

**Dynamics of oscillating piezoelectric micro resonators:
Hydrodynamic loading effect and intrinsic damping**

Dissertation
zur Erlangung des Grades
des Doktors der Ingenieurwissenschaften
der Naturwissenschaftlich- Technischen Fakultät II
- Physik und Mechatronik -
der Universität des Saarlandes

von

Huacheng Qiu

Saarbrücken

2014

Tag des Kolloquiums: 12.03.2015

Dekan: Univ.-Prof. Dr.-Ing. Georg Frey

Mitglieder des Prüfungsausschusses

Vorsitzender: Univ.-Prof. Dr.-Ing. Chihao Xu

1. Gutachter: Univ.-Prof. Dr. rer. nat. Helmut Seidel

2. Gutachter: Univ.-Prof. Dr. José Luis Sánchez-Rojas

Akademischer Mitarbeiter: Dr. Tilman Sauerwald

Abstract

Micro resonators are important components in many micro electro mechanical system (MEMS) applications. The quality factor is a key parameter for MEMS resonators and is determined by the system damping of the devices. Aluminum nitride (AlN) based piezoelectric Si micro resonators with different geometries are fabricated and measured with an all-electrical excitation and detection method, to study the energy dissipation mechanisms. The dynamic behavior of these resonators is analyzed in gases as well as in high vacuum by developing and applying specific experimental, computational and analytical tools.

We investigate the hydrodynamic loading in detail by exploring how factors, such as ambient pressure, the nature of the surrounding gas, the resonator geometry, higher mode operation and the presence of a nearby surface, effect the resonance behaviour of micro resonators. The resonator fluid interaction can be broadly divided into: i) resonators vibrating in an unbounded fluid, and ii) resonators vibrating close to a surface. For the first case, we systematically investigate the performance in different resonant modes. Incompressible flow is expected for the first few resonant modes. However, as the resonant mode number increases, the acoustic wavelength reduces and the energy loss is found to be diluted through mixing of viscous and acoustic effects. For the second case, most prior efforts to investigate this hydrodynamic loading have focused on squeeze film damping with very narrow gaps. In this research we investigate the case that a resonator vibrates close to a surface with a moderate distance.

When a resonator is operated in high vacuum, intrinsic damping inside the solid materials dominates the quality factor. We focus on the three major intrinsic damping effects, which are thermoelastic damping (TED), anchor losses and coating losses. TED and anchor losses are investigated by using a combination of both analytical and numerical methods, while the coating loss mechanism is explored by measuring a series of cantilevers with a piezo-electrode stack coverage varying from 20%-100% of the beam length. Experimental validations are conducted on different structures of piezoelectric micro resonators, showing that the analysis yields qualitative matches with measurements and the contributions of the three mechanisms can be separated to a reasonable extent.

Zusammenfassung

Mikroresonatoren sind wichtige Komponenten in vielen Anwendungen der Mikrosystemtechnik. Der Gütefaktor ist ein Schlüsselparameter für MEMS-Resonatoren und wird durch die Systemdämpfung der Bauelemente bestimmt. Um die Mechanismen des Energieverlusts zu untersuchen, wurden piezoelektrische Si-Mikroresonatoren auf Basis von Aluminiumnitrid (AlN) mit unterschiedlichen Designs hergestellt und mit einem elektrischen Anregungs- und Detektionsverfahren charakterisiert. Experimentelle, theoretische und analytische Werkzeuge wurden entwickelt, um die Dynamik von piezoelektrischen Mikroresonatoren in Gasen sowie im Hochvakuum zu analysieren.

Die hydrodynamischen Energieverluste wurden in Abhängigkeit von verschiedenen Faktoren, wie dem Umgebungsdruck, der Gasart, der Resonatorgeometrie, der Mode und dem Vorhandensein von nahegelegenen Oberflächen untersucht. Die Wechselwirkung zwischen Resonator und Fluid kann in zwei verschiedene Gruppen aufgeteilt werden. Zum einen das Schwingen von Resonatoren in einem unbegrenzten Fluid, zum anderen das Schwingen der Resonatoren in der Nähe einer benachbarten Oberfläche. Für den ersten Fall wurde das Verhalten in verschiedenen Resonanzmoden untersucht, wobei eine inkompressible Strömung für die niedrigeren Moden erwartet wird. Für höhere Moden reduziert sich jedoch die Schallwellenlänge und der Energieverlust kann durch ein Mischen von viskosen und akustischen Effekten beschrieben werden. Bezogen auf den zweiten Fall haben sich fast alle bisherigen Arbeiten auf die Squeeze-Film-Dämpfung in einem sehr engen Spalt fokussiert. Unsere Untersuchung konzentriert sich auf die Dämpfungseigenschaften von Resonatoren in der Nähe einer Oberfläche mit einem moderaten Spaltabstand.

Wenn ein Resonator im Hochvakuum schwingt, dominiert die intrinsische Dämpfung im Festkörpermateriale den Gütefaktor. Die vorliegende Arbeit konzentriert sich auf die drei Hauptbeiträge zur intrinsischen Dämpfung, nämlich auf die thermoelastische Dämpfung (TED), den Ankerverlust und den Beschichtungsverlust. TED und Ankerverluste wurden durch die Verwendung einer Kombination von analytischen und numerischen Methoden untersucht. Der Verlustmechanismus durch Beschichtung mit dem AlN-Piezo-Stack wurde durch eine experimentelle Reihe von Resonatoren mit zwanzig- bis hundertprozentiger Schichtabdeckung bezogen auf die Resonatorlänge charakterisiert. Experimentelle Validierungen zeigen eine qualitative Übereinstimmung mit den simulierten bzw. analytischen Ergebnissen. Ferner können die Dämpfungsbeiträge der drei Mechanismen in nachvollziehbarer Weise qualitativ voneinander getrennt werden.

Table of Contents

Abstract.....	I
Zusammenfassung.....	III
1. Introduction	5
1.1 Piezoelectric micro resonators	5
1.2 Basic concepts.....	6
1.2.1 Excitation and detection principles.....	6
1.2.2 Oscillation modes	7
1.2.3 Fundamental equations of a damped vibrating resonator	8
1.2.4 Fluid dynamics and characteristic numbers.....	9
1.3 Relevant background and literature review.....	10
1.3.1 Full Navier-Stokes equations.....	11
1.3.2 Hydrodynamics of micro resonators vibrating in unbounded fluids	11
1.3.3 Hydrodynamics of micro resonators vibrating close to a surface	12
1.3.4 Thermoelastic damping	13
1.3.5 Anchor loss.....	13
1.3.6 Damping by thin film coating.....	14
1.4 Research goals.....	14
1.5 Outline of this work	15
2. Device fabrication and electrical readout.....	17
2.1 Aluminum nitride based piezoelectric micro resonator fabrication.....	17
2.2 Electrical crosstalk in micro piezoelectric resonators.....	19
2.2.1 Electrical crosstalk introduction	20
2.2.2 Equivalent circuit model.....	21
2.2.3 Performance analysis	22
2.3 Crosstalk compensation solutions	23
2.3.1 On-chip compensation.....	24
2.3.2 Electrical compensation.....	26
2.4 Electrical readout results	27
2.5 Conclusion.....	30
3. Experimental details and results.....	31
3.1 Experimental details.....	31
3.1.1 Measurement setup	31

3.1.2 Device geometry and packaging.....	33
3.1.3 Resonator characterization	37
3.2 Dynamic response of micro resonators vibrating in unbounded fluid	38
3.2.1 Micro resonator performance at the first flexible mode	38
3.2.2 Dependence of micro resonator response on ambient pressure, gas and geometry	41
3.2.3 Micro resonator performance at higher modes.....	46
3.3 Dynamic response of micro resonators vibrating close to a surface.....	51
3.3.1 Dependence of micro resonator responses on gap width	52
3.3.2 Dependence of micro resonator response on ambient gas.....	54
3.3.3 Effect of higher vibrating modes	56
3.4 Conclusion.....	56
4. Analysis of hydrodynamic loading on vibrating micro resonators.....	59
4.1 Full Navier-Stokes equations and numerical simulation	60
4.1.1 Theory.....	60
4.1.2 Physical interpretation	61
4.1.3 Comparison between experimental and simulated results.....	63
4.2 Hydrodynamics of micro resonators vibrating in unbounded fluids.....	66
4.2.1 Analysis for micro resonators in the flexural mode	66
4.2.2 Comparison between experimental and analytical results for the flexural mode	70
4.2.3 Analysis for micro resonators in the torsional mode.....	72
4.2.4 Comparison between experimental and analytical results for the torsional mode	73
4.2.5 Discussion on the influence of the fluid compressibility	74
4.3 Hydrodynamics of micro resonators vibrating close to a surface.....	77
4.3.1 Mathematical models for micro resonators vibrating close to a surface	77
4.3.2 Comparison between experimental, analytical and simulated results	81
4.3.3 Discussion.....	86
5. Analysis of intrinsic damping in piezoelectric micro resonators	89
5.1 Thermoelastic damping (TED)	89
5.1.1 Analytical model for TED	90
5.1.2 Numerical simulation for TED	90
5.1.3 Comparison between analytical and simulated results.....	91
5.1.4 Conclusion.....	95

5.2 Anchor losses	95
5.2.1 Analytical models for anchor losses	95
5.2.2 Numerical simulation for anchor losses	97
5.2.3 Comparison between analytical and simulated results	99
5.2.4 Discussion.....	100
5.3 Damping by thin film coating	100
5.3.1 Experiments	101
5.3.2 Discussion.....	103
5.4 Experimental verification.....	103
5.5 Conclusion.....	105
6. Conclusion and outlook.....	107
6.1 Conclusion.....	107
6.2 Outlook.....	110
References	111
Publications.....	125
Journal publications	125
Conference publications.....	125
List of figures	127
List of tables.....	133
Nomenclature.....	135
Greek symbols.....	135
Roman symbols.....	137
Acknowledgements.....	143
Eidesstattliche Versicherung.....	145

1. Introduction

1.1 Piezoelectric micro resonators

Micromechanical resonators have been developed as sensor platforms for detecting small mass and force due to their tiny structures [1], and widely used in a large variety of applications. This includes acoustic wave resonators [2], ultrasonic transducers [3], gyroscopes [4], accelerometers [5], filters [6], energy harvesters [7], micro balances [8], and fluid sensors [9-11]. Among a large variety of resonator structures, piezoelectric micro resonators have been attracting intensive attention due to their advantages in low-cost fabrication and high sensitivity [12]. For many applications, piezoelectric resonators are more attractive than other types, such as electrostatic [13], electromagnetic [14] or optically-associated [15] resonators, due to their self-exciting and self-sensing capability, low driving voltage and full integration. To be compatible with complementary metal-oxide-semiconductor (CMOS) technology, aluminum nitride (AlN) was selected as the active piezoelectric layer in this research. Furthermore, both high piezoelectric coefficients and low intrinsic stress of the AlN film can be obtained by controlling the deposition parameters [16].

The piezoelectric resonator normally works in two port mode, which means one area of the active piezoelectric layer provides an input bending stress for the resonator, and another area of the layer can be used to detect the resulting vibration. However, the electrical crosstalk between drive and sense ports of the resonator makes the mechanical resonance less pronounced, and the characterization of the resonator more difficult [17, 18]. Besides, a relatively weak output signal from the AlN film requires a high precision pre-amplifier for the detection of the resonance. In this work, an electrical compensation and readout method has been developed [19]. By using this method, the measurements can be completed by all-electrical excitation and detection.

MEMS resonators are normally operated in fluids (such as air or liquid) under varying pressure ranges from vacuum to atmospheric. In most applications, the resonance behavior may change due to external environmental influences to the device and needs to be determined. The variation in resonance response of oscillators can be characterized in terms of resonance frequency f_r and quality factor Q . The Q factor is defined as the ratio of stored energy to the dissipated energy per cycle. This is equivalent to $f_r/\Delta f$, where Δf is the peak width at half power. In general, a high Q factor results in a sharper resonance peak and leads to a better detectable resolution (refer to Fig. 1.1 to see two resonance curves with different

resonance frequencies and Q factors). In this work, we will present the results of experimental, simulated and analytic investigations on hydrodynamic loading and intrinsic damping effects which damp vibrations of micro resonators.

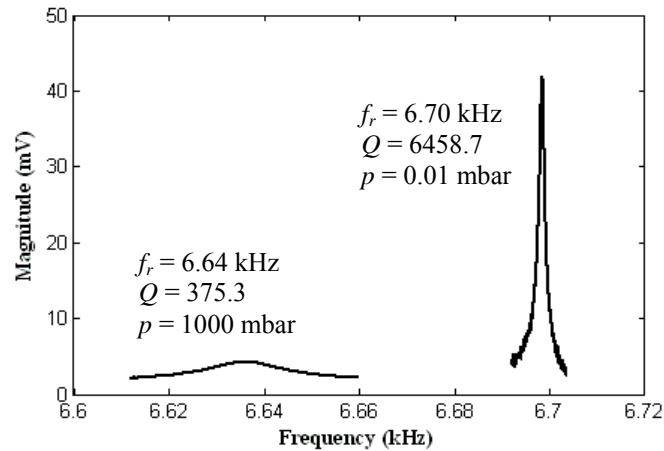


Figure 1.1: Resonance curves for a resonator at pressures of 0.01 mbar (narrow resonance) and 1000 mbar (broad resonance).

1.2 Basic concepts

1.2.1 Excitation and detection principles

The mechanical resonator structure has to be brought into vibration and the vibration has to be detected. There are several types of excitation techniques, each having a corresponding detection method based on the same principle or arrangement for the interrogation of the vibration [20]. Electrostatic excitation and capacitive detection, piezoelectric excitation and detection, magnetic excitation, electrothermal excitation, photothermal excitation, piezoresistive detection, and optical detection are widely used in MEMS resonator applications [21, 22]. For example, the electrothermal excitation and piezoresistive detection were chosen as driving and detector mechanisms in Ref. [23] by integrating two diffused p-type silicon resistors at the clamped edge of the microcantilever.

The most popular and most widely used methods are based on electrostatic excitation and capacitive detection as well as on piezoelectric excitation and detection. The first method requires two electrodes arranged in close proximity, where one of the electrodes is a part of the vibrating structure. Capacitive resonators with very high Q have been demonstrated e.g. by [24, 25] and are produced commercially. In order to achieve a good electromechanical coupling and acceptable impedance levels, large bias voltages and submicron gaps are required. To overcome these challenges, piezoelectrically transduced MEMS resonators have emerged as a valid alternative [26-28]. A major advantage is that no counter electrode is necessary so that the gap size can be designed to any desired value. The main drawback of

piezoelectric transduction is the necessity of the additional piezoelectric material and the integration of the piezoelectric material with the silicon based resonator. Besides, it has been observed experimentally that the presence of the piezoelectric layer may degrade the quality factor considerably.

1.2.2 Oscillation modes

Most MEMS-based resonators are fabricated from silicon wafers or silicon-on-insulator (SOI) wafers by micromachining techniques. The basic elements of MEMS-based resonators are microstructures such as cantilevers, bridges, membranes and plates, which are fully or partially anchored, usually onto a silicon substrate. MEMS resonators are used in different fields of application, depending on their different resonant modes: bulk mode, shear mode, flexural mode and torsional mode etc. [29-33]. Beam-type resonators such as AFM probes [34] and fluidic sensors [35] are widely applied due to their relatively large deformation and simple fabrication compared to other resonators. Each resonator structure has its own displacement pattern, resonance frequency and Q factor. The cantilever, for example, may vibrate in a flexural, torsional or lateral mode, as illustrated in Fig. 1.2. Each mode type may have several higher-order resonance frequencies, as shown in Fig. 1.3 for a cantilever structure vibrates in flexural modes. The figures are plotted by finite element analysis software COMSOL.

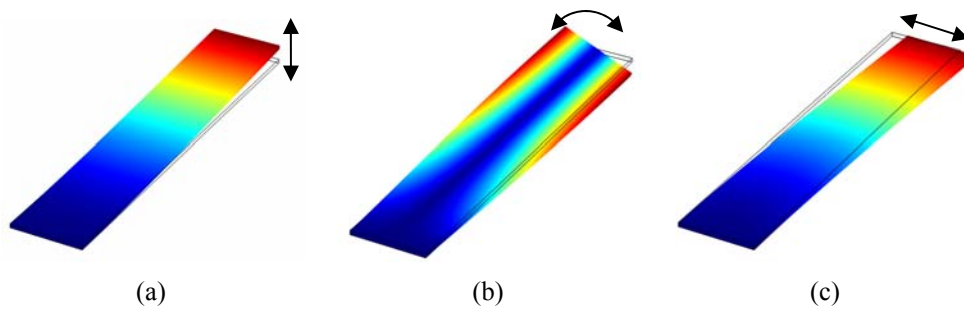


Figure 1.2: Cantilever beam in fundamental (a) flexural, (b) torsional and (c) lateral vibration modes. The color coding represents the deflection in the relevant direction.

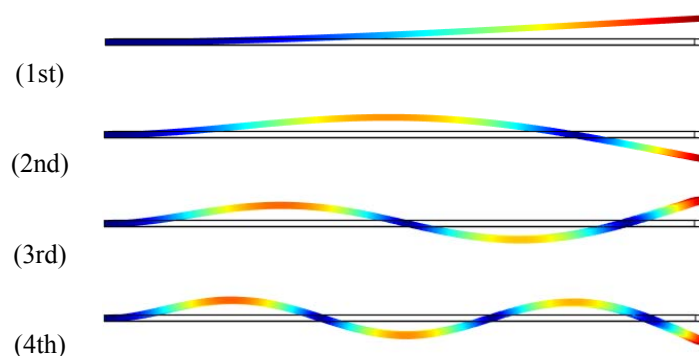


Figure 1.3: First four flexural mode shapes of a cantilever.

1.2.3 Fundamental equations of a damped vibrating resonator

For a linear harmonic vibration, which means the vibration amplitude is much smaller compared to the resonator dimensions, the mechanical performance of the resonator can be described by a second order differential equation:

$$m\ddot{x} + c_0\dot{x} + k_0x = f, \quad (1.1)$$

where m , c_0 and k_0 are the mass, damping coefficient and spring constant of the resonator, respectively, f is the external force acting on the resonator, and x is the position (deflection) of the mass. When operated in a fluid, the resonator will experience a drag force from the fluid, the external force f can be separated into two contributions:

$$f = f_{hydro} + f_{drive}, \quad (1.2)$$

the first component in eq. (1.2) is a hydrodynamic loading component due to the motion of the fluid around the beam, whereas the second term is a driving force that excites the beam. The driving force is usually a known function. The hydrodynamic loading can be obtained by deriving from measurement or solving for the flow field around the resonator.

In many previous studies, e.g. [36], f_{hydro} has been characterized by damping force and spring force terms:

$$f_{hydro} = c_a\dot{x} + k_ax, \quad (1.3)$$

where $c_a = \text{Real}(f_{hydro}/\dot{x})$ is the fluidic damping coefficient and $k_a = -\omega \text{Imag}(f_{hydro}/\dot{x})$ is the fluidic spring constant.

Substituting eqs. (1.2 and 1.3) into eq. (1.1), we obtain an uncoupled equation for the structure:

$$m\ddot{x} + c\dot{x} + kx = f_{drive}, \quad (1.4)$$

$$c = c_0 + c_a, \quad (1.5)$$

$$k = k_0 + k_a, \quad (1.6)$$

where c and k include the contributions from the resonator and the surrounding fluid.

The resonance frequency f_r and the quality factor Q are given as:

$$f_r = \frac{1}{2\pi} \sqrt{\frac{k}{m}}, \quad Q = \frac{\omega}{\Delta\omega}, \quad \Delta\omega = \frac{c}{m}, \quad (1.7)$$

$\Delta\omega$ is the resonance bandwidth at which the response amplitude equals 71% of the peak

value.

Eq. (1.4) gives a relatively simple form for understanding the fluid effects in terms of fluidic damping coefficients and spring constant. Nevertheless, note that the above analysis does not tell us how the damping coefficient and spring constant will vary with resonator dimensions, fluid viscosity or density, or the distance to a nearby wall. These are simply the tools that help us characterize the resonance.

1.2.4 Fluid dynamics and characteristic numbers

The fluid dynamics of MEMS resonators can be formulated by simply treating the resonator as a solid body oscillating in a fluid. Through the solid-fluid boundary, an oscillating flow is set up in the fluid, which dissipates energy and results in mass loading of the resonator. A natural starting point for our discussion is the static flow. For a solid object moving through a fluid at a constant speed, the fluid drag force, caused by the fluid pressure and stress, acts to oppose the motion of the object. The Reynolds number is the fundamental parameter characterizing the flow dynamics, which is given by

$$Re = \rho u_0 L / \eta, \quad (1.8)$$

where ρ and η are the fluid density and the viscosity respectively, and u_0 is the characteristic object velocity and L is the characteristic length parameter of the object.

We now turn to the problem of a solid object oscillating at angular frequency ω in an unbounded (infinite) fluid. Let us consider a simple but typical example: a sphere with radius R , which is illustrated in Fig. 1.4. Surrounding the sphere there is a boundary layer where the flow velocity has dropped by a factor of $1/e$ [37]. Inside the boundary layer the flow is nearly tangential to the body surface, while outside the layer the flow can be assumed as inviscid. For this reason, the boundary layer is also called as viscous layer [38]. The layer thickness δ is dependent on the pressure (equivalent to the fluid density ρ) and is given by

$$\delta = \sqrt{2\eta / \rho\omega}. \quad (1.9)$$

The dimensionless Reynolds number Re in this problem is frequency dependent and some authors prefer to define it as

$$Re = \rho\omega L^2 / \eta. \quad (1.10)$$

Here the characteristic length L is the radius of the sphere R . Notice that Re is also a simple ratio between L and δ since it also equals to $2L^2 / \delta^2$.

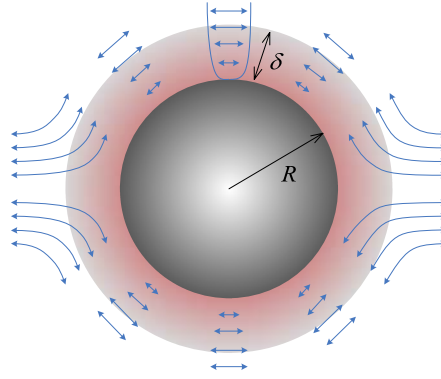


Figure 1.4: Illustration of a sphere oscillating in a Newtonian fluid at angular frequency ω . Inside the boundary layer, the flow is nearly tangential to the solid body surface.

1.3 Relevant background and literature review

Energy can be dissipated in different ways for a resonator, as schematically shown in Fig. 1.5. In general, when the resonator is operated in high vacuum, only intrinsic energy losses Q_{int}^{-1} are relevant. They contain thermoelastic damping Q_{TED}^{-1} in the structure, radiation of elastic energy into the attachment (anchor losses) Q_{anchor}^{-1} and energy losses due to coating films $Q_{coating}^{-1}$. When the resonator vibrates in a gaseous medium, external losses Q_{gas}^{-1} dominate the scene. They consist of viscous losses Q_{vis}^{-1} , acoustic losses Q_{acous}^{-1} and squeeze film losses Q_{squ}^{-1} if there is a nearby surface to the resonator, defining a gap. The energy dissipated per cycle is the sum of the energy dissipated by each of these mechanisms:

$$Q_{tot}^{-1} = \underbrace{Q_{vis}^{-1} + Q_{acous}^{-1} + Q_{squ}^{-1}}_{Q_{gas}^{-1}} + \underbrace{Q_{anchor}^{-1} + Q_{TED}^{-1} + Q_{coating}^{-1}}_{Q_{int}^{-1}} + Q_{other}^{-1}. \quad (1.11)$$

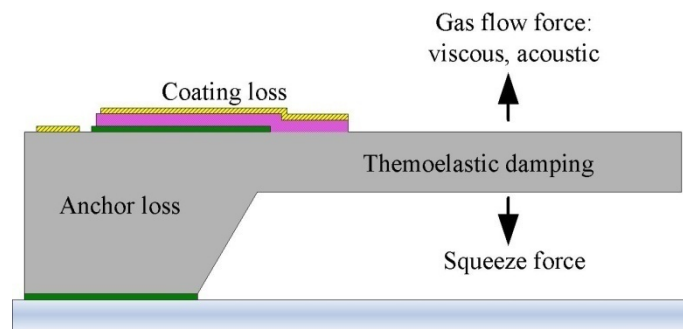


Figure 1.5: Energy dissipation mechanisms of micro resonators.

It is obvious that Q_{tot} cannot exceed the smallest component. All other possible sources (like residual stress loss in silicon and electrical loss in AlN material) of damping are neglected in the analysis and kept minimal in the experiments. The following discussion will review recent researches on each individual contribution.

1.3.1 Full Navier-Stokes equations

Micromechanical resonators can be profoundly influenced by the fluid surrounding them. For a continuous fluid medium, the most extensive type of model clearly must be based on a solution of the full set of Navier-Stokes equations. The derivation of the full set of equations was first given by Bruneau *et al.* [39]. The governing equations are rewritten into a set of linearized equations suited for implementation in Boundary Element Method (BEM) environment. Beltman [40, 41], Karra *et al.* [42] and Qiu *et al.* [43] developed their own numerical codes to solve the equations based on the BEM method. On the other hand, fully coupled three-dimensional simulations from Lee *et al.* [44] and Basak *et al.* [45] were performed leading to highly accurate results. Furthermore, commercial package COMSOL Multiphysics also offers the possibility to solve and simulate the full model equations [46].

However, due to the mathematical complexity, the full Navier-Stokes model is computationally costly and nonintuitive for gaining physical insight. Several authors have attempted to simplify the fluid-structure interaction problem based on certain assumptions, and predicted analytically the quality factors and frequency shifts of microcantilevers in viscous fluids. The cases on micro resonator vibrating in fluid can be broadly divided into i) those that deal with a micro resonator vibrating in an unbounded fluid, ii) those that deal with a micro resonator vibrating close to a surface, defining a gap.

1.3.2 Hydrodynamics of micro resonators vibrating in unbounded fluids

For the first case, lots of previous researches have been focused on the viscous loss effect on micro resonators vibrating in the first few harmonic modes. The gas flow is expected as incompressible, since the dominant length scale of the beam is much smaller than the wavelength of sound in the gas, and viscous drag is typically the dominant gas damping mechanism. Viscous damping models require solutions of the Navier-Stokes equations for unsteady incompressible flow, for some simple geometry taken as an approximation of the actual geometry. In Refs. [47-50] a microcantilever was modeled as a combination of spheres, based on the fluidic drag force calculation on an oscillatory motion sphere from Landau and Lifshitz [51]. On the other hand, in Refs. [52, 53] a semianalytical theory was developed to predict the quality factor of microcantilevers vibrating in an unbounded viscous fluid based on the earlier work of Tuck [54], by simplifying the cantilever as a cylinder. It is worth to note that the analytical model predictions are considered sufficiently accurate from beam aspect ratios length/width higher than 3.5 [55].

Besides, Blom *et al.* [56] as well as Naeli and Brand [57] investigated the dependence of the

Q factor on the cantilever geometry, while Xia and Li [58], Lu *et al.* [59] and Dohn *et al.* [60] discussed different resonant-mode effects on the cantilever performance. Blom *et al.* [56] pointed out that the Q factor of a resonator in a higher order flexural mode is larger than that of a lower one. However, will the quality factor always increase as the mode number increases? Recent papers from Van Eysden and Sader [61, 62] detailed a model for a cantilever beam oscillating in a compressible fluid. They found that an increase of the quality factor is not always valid. This is further confirmed by Weiss *et al.* [63] who compared the compressible fluid and incompressible fluid simulation results using a numerical method. Jensen and Hegner [64] carried out measurements and found qualitative agreement between experimental results and calculations based on the compressible fluid model of Van Eysden and Sader.

1.3.3 Hydrodynamics of micro resonators vibrating close to a surface

In a lot of practical applications, resonators are vibrating near a surface. Nearly five decades ago, Newell [65] observed that the ever-present damping effect of the surrounding air would be increased when a plate was oscillating near a second surface due to the squeeze film action of air between the surfaces. The traditional squeeze film model, which is derived using Reynolds equation from hydrodynamic lubrication theory, is sufficient to deal with resonators vibrating very close to a surface or the plate dimensions are much larger than the film thickness. Much theoretical work and many measurements have been carried out to explore the squeeze film effect with a very narrow air gap [66-73]. In these literatures only the fluid layer between the microcantilever and the surface is considered, the fluid on the opposite side of the gap is not modeled. Moreover, an effective fluid viscosity is used in rarefied fluids to account for the non-continuum fluid behavior at very low pressures.

However, the squeeze film assumption does not always hold. At moderate distances, the motion of the fluid all around the microcantilever affects its motion and the squeeze film effect alone does not capture the fluid loading. To determine the hydrodynamic loading effect analytically, it would be necessary to solve a set of coupled nonlinear equations governing the structure and fluid motions. Therefore experimental and computational studies are needed to associate the analytical solution. The literatures dealing with this problem can be mainly divided into (a) those dealing with experimental determination of hydrodynamic quantities, and (b) those dealing with analytical/semi-analytical models. As to the first approach, in [74-76] the effect of a nearby surface to a microcantilever vibration in air and in different liquids is investigated experimentally. The Q factors are tabulated and fitted to a polynomial as a

function of gap length. While for the second approach, Veijola *et al.* [77, 78] have proposed a model for micromechanical squeeze film dampers with gap sizes comparable to the surface dimensions by considering the effect of open boundaries. The fluid loading on the opposite side of the gap is still not included in this model. Other authors [79-81] proposed a semi-analytical solution from the numerical solution of the unsteady Stokes equations for microbeams oscillating near rigid walls. Besides, Schwarz and Seidel [82] have proposed a new thermo-mechanical resonance model to account for the gas damping effect (called “dynamic” damping in their work) in the transition regime. The resonance behavior over a wide pressure range is then modeled quantitatively by the superposition of different damping mechanisms, e.g. intrinsic damping, free molecular damping, viscous damping and dynamic damping.

1.3.4 Thermoelastic damping

When a resonator is operated in high vacuum, the energy dissipation inside the materials of the resonator dominates the damping behavior. One of the energy dissipation mechanisms discussed here is thermoelastic damping (TED). When the resonator structure is deformed, a strain gradient is produced, and this leads to a temperature gradient. This induced temperature gradient yields heat flow, and energy is therefore dissipated due to an increase in entropy. If the vibration frequency is of the order of the heat relaxation rate, the energy loss due to TED becomes appreciable, resulting in a low quality factor.

TED theory has been systematically developed since the 1930s. To our knowledge, Zener is the first one who studied and modelled TED in flexural vibrating cantilevers in 1937 [83, 84]. Recently, extensive research on TED has been performed by many research groups in order to extend Zener’s model to more complex geometries [85-89]. The analytical models are subject to very restrictive assumptions. Thus they are not sufficiently accurate to predict the behaviour of complex 3D structures. There is a great need to use numerical simulations for TED analysis; Antkowiak [90], Gorman [91] and Duwel [92] pioneered the TED numerical analysis in MEMS. Their methods are also implemented in the COMSOL Multiphysics software [46].

1.3.5 Anchor loss

Anchor loss (also called support loss or clamping loss) concerns the mechanical energy that is dissipated via the coupling to the support structure. During its vibrating motion, a resonator exerts the supporting structure to small deformations, thereby leading to the generation and propagation of elastic waves from the resonator to the surrounding material. Therefore, the

support structure absorbs some of the vibration energy of the resonator.

To analytically predict anchor losses, simplifications of the support geometry are often made. For example, the anchor loss of a cantilever beam of infinite width attached to a semi-infinite medium is studied in Refs. [93-96], while Refs. [97, 98] investigated the anchor loss by assuming the support structure as semi-infinite elastic media with finite or infinite thickness. The calculations were derived either in the 2D [93-96] or 3D [97, 98] methods. However, all these approaches contain simplifying assumptions which are generally difficult to quantify, and the calculated results also differ substantially from each other. Hence, for more realistic geometries of micromachined cantilevers, numerical techniques are required for the prediction of anchor losses.

From the numerical standpoint different options are available for the simulation of wave dissipation, among which the Perfectly Matched Layer (PML) techniques are the most commonly employed [99, 100]. The approach taken in commercial package CoventorWare's MemMech solver is similar to PML techniques [101]. The solver includes a "QuietBoundary" boundary condition, which assumes the boundary extending to infinity. This can be applied to predict elastic energy that is transmitted via the anchor to the substrate.

1.3.6 Damping by thin film coating

For many applications, the resonators are coated with thin films to supply driving and/or sensing electrical functions (as in this work), or else to supply optical reflectivity [102] or to alter surface chemistry [12]. Experience with several devices suggests that these coatings can increase damping; in some cases, relatively thin metallic films have been found to degrade the quality factor of ceramic beams by an order of magnitude. The reason might be internal friction between/in each layer. Great effort has been put into describing the effect of cantilever coating on their resonant behavior. For example, Sandberg *et al.* [103] and Sekaric *et al.* [104] investigated the effect of metal coating on the quality factor of a micro/nano resonator and showed that in vacuum Q is severely reduced by the deposition of even a thin metal film with a thickness of 100 nm, while the absence of these metal coatings results in a three to four times higher Q factor. Moreover, the thin coating film damping is found proportionally dependent on the coating thickness.

1.4 Research goals

The interest is growing to analyze the energy dissipation mechanisms and improve the design of high precision micro structures. The major goal of this research is, by using the

combination of experiments, numerical simulations and analytical calculations, to develop a closed loop platform for understanding and predicting the resonator behavior in gases over a wide pressure range as well as intrinsic damping in vacuum. Experiments provide measured data for modeling the resonator behavior. Numerical simulations are advantageous as they are less demanding in terms of both time and costs than experiments. While compact analytical calculations allow a better understanding of the interactions between different physical fields.

The objectives of this research can be divided into four main tasks:

- Fabricate piezoelectric micro resonators with different geometries, and develop all-electrical excitation and detection method for the resonators.
- Experimentally evaluate and compare the effect of ambient pressure, surrounding gases, resonator geometry, higher mode operation and the presence of a nearby surface on the resonance behavior of micro resonators.
- Propose analytical models as well as Finite Element Method (FEM) simulations to explain the gas drag damping effect. The cases on micro resonator vibrating in fluid can be broadly divided into vibrating in unbounded fluid and vibrating close to a surface. Relatively compact analytical solutions need to be proposed and compare with measurements.
- For MEMS resonators operated in vacuum, we will focus on the intrinsic energy dissipation mechanisms to understand the Q factor upper limit. Each dissipation mechanism needs to be investigated experimentally or numerically, theoretically we develop/improve an approximation for each loss mechanism. Useful relation is developed to aid MEMS designers in achieving Q factor prediction and control in the design phase.

1.5 Outline of this work

In order to present the work carried out, the dissertation is divided into the following Chapters:

- Chapter 1 **Introduction**; briefly introduces the context of the research and describes the work objectives and strategy. A comprehensive literature review is also presented on different energy loss mechanisms that occur in MEMS resonators.
- Chapter 2 **Device fabrication and electrical readout**; describes the piezoelectric AlN based resonator fabrication procedure and all-electrical excitation and detection methods. A specifically designed compensation-readout circuit is presented.
- Chapter 3 **Experimental details and results**; presents detailed measurements of the

frequency response of a series of micro resonators. This part aims at evaluating and comparing systematically the effects of ambient pressure, the nature of the surrounding gas, resonator geometry, higher mode operation and the presence of a nearby surface on the resonance behavior.

- Chapter 4 **Analysis of hydrodynamic loading on vibrating micro resonators**; focuses on beam-type resonators operating in gas mediums. Firstly, the full set of Navier-Stokes equations is semi-analytically solved and simulated using commercial package COMSOL Multiphysics. Secondly, hydrodynamic loading for slender structures vibrating in unbounded fluid is analyzed, as well as discussion on the influence of the fluid's compressibility. Thirdly, hydrodynamic loading of slender structures vibrating at very near to moderate distances from a surface is studied.
- Chapter 5 **Analysis of intrinsic damping in vibrating piezoelectric micro resonators**; focuses on three major intrinsic damping effects on piezoelectric micro resonators, which are thermoelastic damping, anchor losses and coating losses. Each damping mechanism is studied individually, by the combination of experimental, analytical and numerical methods. At the end, a series of experimental validations are conducted on different structures of piezoelectric cantilevers.
- Chapter 6 **Conclusion and outlook**; finally summarizes and concludes this research work and presents an outlook for future projects.

2. Device fabrication and electrical readout

In this Chapter we describe the experimental procedure, including the device fabrication and measurement. Piezoelectric aluminum nitride (AlN) based resonators were fabricated and tested. The effect of the input-output electrical crosstalk was found to be significant. The overall output of two-port piezoelectric resonators is a superposition of the mechanical resonance behavior and of the electrical crosstalk, the latter coming mainly from the coupling feedthrough capacitance. Two crosstalk compensation schemes have been developed for an AlN based doubly clamped beam resonator. The first solution demonstrates an on-chip self-cancellation technique of the feedthrough capacitance by using a compensation electrode and applying a complementary voltage to it, while the second solution applies an adjustable compensation voltage to the common bottom electrode. A specifically designed compensation-readout circuit is presented. Experimental investigations of the output signal proved the efficiency of both crosstalk compensation solutions.

2.1 Aluminum nitride based piezoelectric micro resonator fabrication

AlN is a preferred functional layer for MEMS applications, such as microactuators or microsensors, due to its high CMOS compatibility and good piezoelectric coefficients [105]. Alternative piezoelectric thin film materials are zinc oxide (ZnO) and lead zirconate titanate compounds (PZT). PZT has much higher piezoelectric coefficients than AlN or ZnO. However, the preparation of suitable thin films of this three-component system is very complex and difficult [106]. AlN and ZnO thin films can be deposited at relatively low temperatures [107, 108], which is important to decrease the intrinsic stress in the films. A low intrinsic stress value is essential for the integration of films onto mechanically soft structures, like beams or membranes. Zn affects the lifetime of minority carriers in silicon and therefore is not compatible with standard CMOS processes. This problem does not occur with AlN, which can be deposited at room temperature and is fully compatible with standard CMOS processes. In this work, the AlN thin films were sputtered reactively from an aluminum (Al) target in a pure nitrogen atmosphere, using a DC magnetron sputtering machine from "Von Ardenne". The sputtering parameters were controlled precisely to achieve good c-axis orientation of the thin film [16] with an effective piezoelectric constant $d_{33} = 3$ pm/V and $d_{31} = -1.0$ pm/V [105]. Fig. 2.1 shows a photograph of the sputtering machine and a schematic description of the AlN reactive sputtering process.

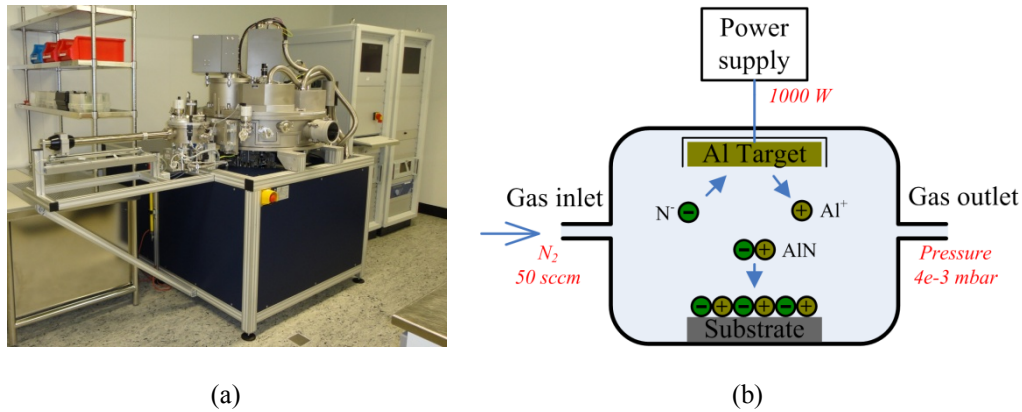


Figure 2.1: (a) Photograph of the sputtering machine (von Ardenne) and (b) a schematic description of the AlN reactive sputtering process.

The AlN based resonators were fabricated using a low-resistivity (less than $0.1 \Omega \text{ cm}$) p-type (100) single crystal silicon (SCS) wafer. The SCS forms the resonator and simultaneously serves as bottom electrode for the piezoelectric layer. Fig. 2.2 shows the flowchart of the fabrication process. First, the SCS wafer was oxidized on both sides in a dry atmosphere at 1000°C to form 120 nm thick SiO_2 layers for passivation purposes. Then a 500 nm thick PECVD Si_xN_y layer was deposited on the bottom side of the wafer (Fig. 2.2 a). The top SiO_2 layer acted as an insulator between the top and bottom electrodes, while the bottom SiO_2 and Si_xN_y layers were used as a hard mask for anisotropically etching the SCS substrate to a residual thickness of about $20 \mu\text{m}$ at the areas where the suspended beam is located. In a next step a $1 \mu\text{m}$ thick AlN film and a 300 nm thick gold (Au) film were sputter deposited and etched to form a sandwiched piezo-electrode stack together with the SCS bottom electrode (Fig. 2.2 b). Then the AlN film was patterned in 80°C phosphoric acid (H_3PO_4) [109]. The Au layer was patterned in aqua regia, nitric acid (HNO_3) and hydrochloric acid (HCl) in a mixing ratio of 1:3, to form the top electrode as well as to provide the contact pads to the SCS bottom electrode. Finally, the resonant beam was formed by back side wet etching in 38% potassium hydroxide (KOH) at 80°C and was then released by a dry etching process at cryogenic temperatures using a $\text{SF}_6\text{-O}_2$ gas composition (Fig. 2.2 c).

In this work, the methods for feedthrough capacitance analysis and cancellation have been demonstrated using a doubly-clamped beam resonator as an example. The resonator consists of several active piezoelectric areas of the same size, in order to demonstrate different crosstalk compensation solutions. Fig. 2.3 shows the optical micrograph of the drive port of the fabricated resonator. The sense port is identical to the drive port. The active piezoelectric area was divided into three parts: the areas on the left and right hand sides were used as the drive electrodes to excite the resonator. The compensation electrode is located in the center.

Its use and the overall crosstalk compensation scheme are described in Section 2.3. The nominal dimensions of the bridge are 200 μm in width and 3400 μm in length.

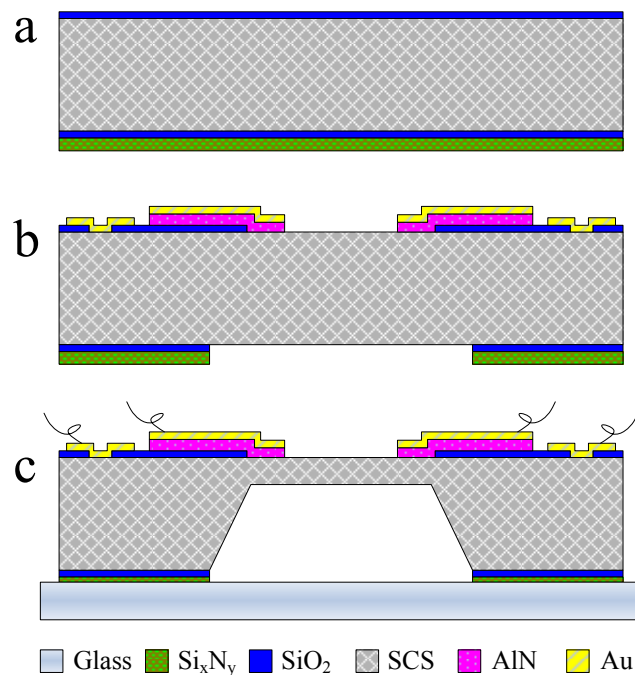


Figure 2.2: Flow chart of the resonator fabrication process.

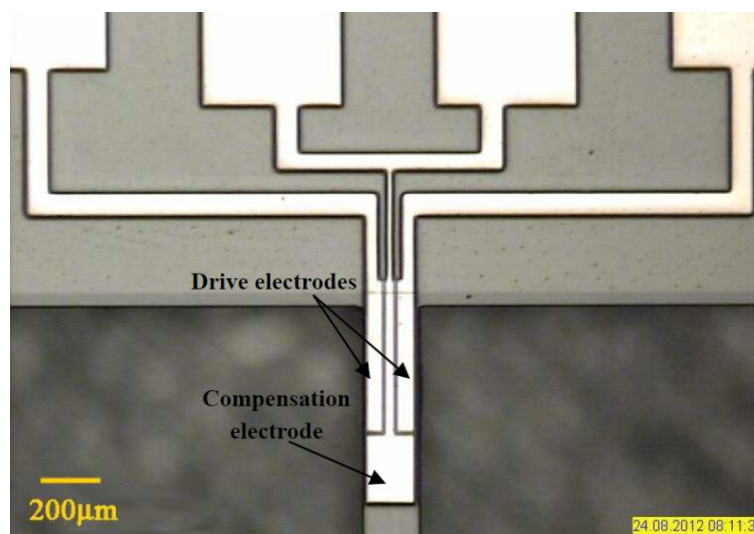


Figure 2.3: Micrograph of the drive port of the piezoelectric resonator, including the compensation electrode discussed in Section 2.3.

2.2 Electrical crosstalk in micro piezoelectric resonators

As the first testing stage, the fabricated resonator was tested by supplying a sinusoidal voltage on the drive electrode, and detecting the output change of the sense electrode. The resonator output was found to be a superposition of the mechanical resonance behavior and electrical crosstalk effects, the latter coming mainly from the coupling feedthrough capacitance. The crosstalk affects the electrical behavior significantly, even to the point of swamping the

resonance behavior of the resonator. This Section reports on the electrical performance analysis and modeling of AlN piezoelectric resonators.

2.2.1 Electrical crosstalk introduction

The overall output function $U_o(s)$ of a two-port piezoelectric resonator can be written as the sum of two contributions: $U_M(s)$, representing the mechanical resonance behavior, and $U_E(s)$, representing electrical crosstalk. This is shown schematically in Fig. 2.4. The crosstalk $U_E(s)$ is assumed to be constant in a narrow frequency range around the resonance, while $U_M(s)$ gets a maximal amplitude $|U_M(i\omega_r)|$ at the resonance frequency $\omega = \omega_r$. A figure of merit (which has to be minimized for best compensation) may be defined by using the ratio of the crosstalk to the mechanical resonance signal:

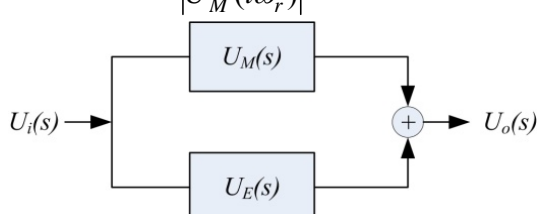
$$\lambda = \frac{|U_E|}{|U_M(i\omega_r)|} \quad (2.1)$$


Figure 2.4: The overall transfer function diagram of a two-port piezoelectric resonator.

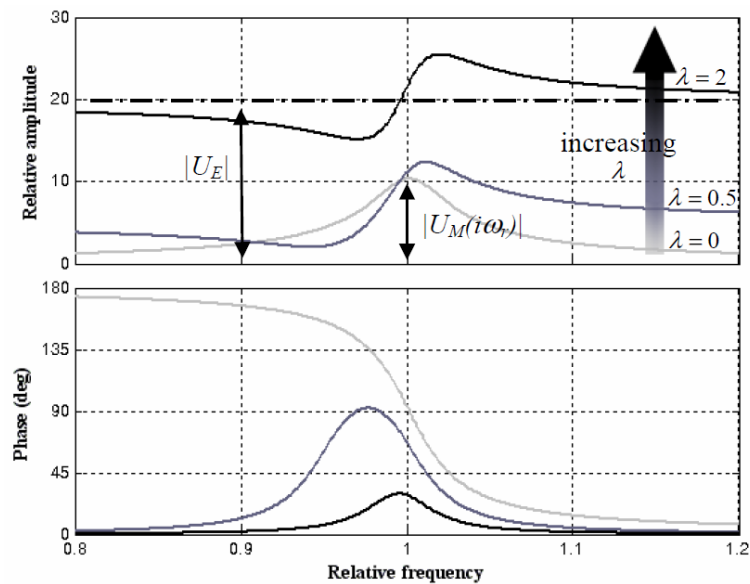


Figure 2.5: Illustration of the effect of increasing the figure of merit λ on the electrical output of a two port piezoelectric resonator, the lightest color lines show the output without any crosstalk ($\lambda = 0$).

Fig. 2.5 illustrates the effect of increasing the figure of merit λ on the electrical output of a two port piezoelectric resonator. The figure shows that crosstalk may introduce “anti-resonance” peaks and a shift of frequency at the maximum output, which makes the electrical detection of resonance frequency and quality factor more difficult. In the worst situation, i.e.

low quality factor due to high air damping, the crosstalk will completely obscure the mechanical resonance, making detection of the resonance peak impossible.

2.2.2 Equivalent circuit model

The electrical capacitances in the resonator are shown in Fig. 2.6. C_{d1} and C_{s1} are represented as the capacitances between the top electrode, AlN layer and SCS bottom electrode layer on the suspended bridge; C_{d2} and C_{s2} differ from C_{d1} and C_{s1} as there is an isolating SiO_2 layer under the AlN layer. As drive port and sense port have a common ground connected through the SCS substrate, an input AC voltage at the drive electrode will produce an output at the sense electrode. The feedthrough capacitance C_{ft} is used to account for the mutual coupling capacitances between drive and sense electrodes.

The resonator's electrical behavior for a narrow frequency range around resonance can be modeled by an equivalent circuit shown in Fig. 2.7. The transformer couples energy from the electrical domain to the mechanical domain and vice versa. The motional branch (L_m , C_m and R_m) describes the mechanical-modal behavior of the structure (i.e. resonant frequency and quality factor). The outer capacitor branch (C_d , C_{ft} and C_s) describes the electrical behavior without mechanical vibration. These capacitances were measured using an LCR meter and are listed in Tab. 2.1. C_d and C_s here include the capacitances $C_{d1,2}$ and $C_{s1,2}$ respectively. The other parameters of the equivalent circuit model can be determined according to [17].

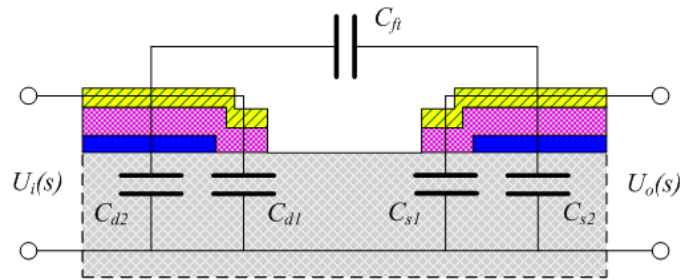


Figure 2.6: Simplified capacitance model of the piezoelectric resonator.

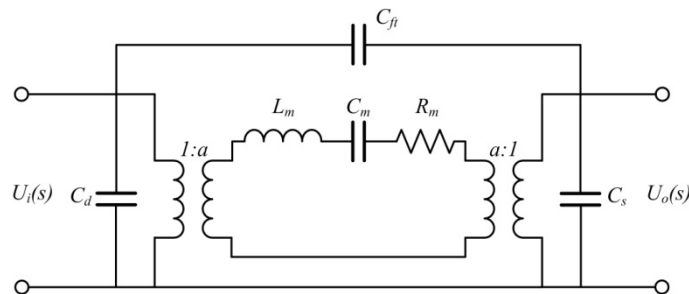


Figure 2.7: Equivalent circuit model for the two port piezoelectric resonator.

	Symbol	Calculated Value
Drive port shunt capacitance	C_d	255 pF
Sense port shunt capacitance	C_s	232 pF
Feedthrough capacitance	C_{ft}	26.3 fF

Table 2.1: Capacitances of the fabricated resonator.

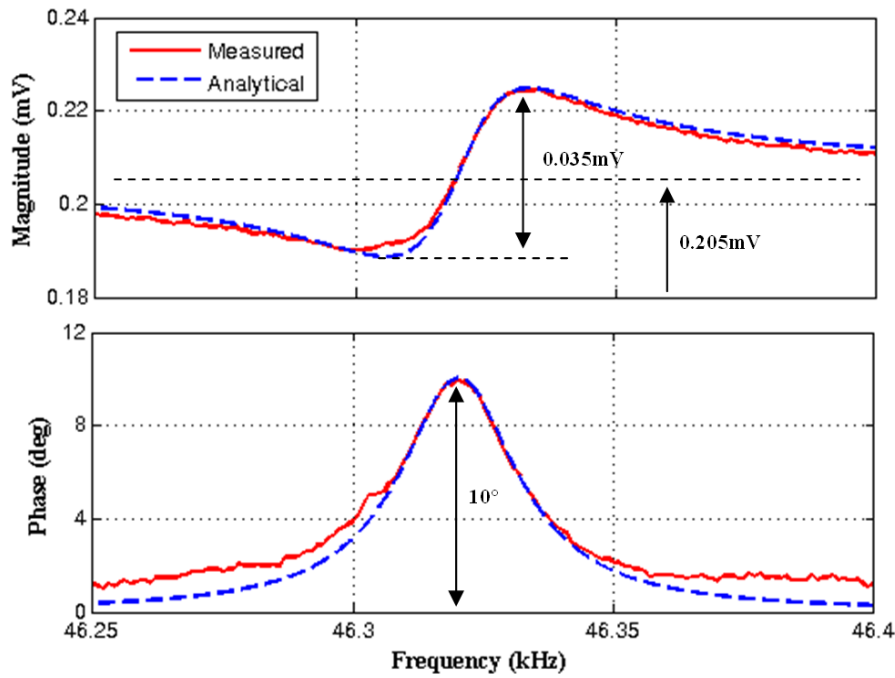


Figure 2.8: Measured and analytically derived response of the AlN based piezoelectric resonator at normal atmosphere.

Fig. 2.8 compares the response of this bridge resonator to a $2 V_{pp}$ drive voltage at normal atmosphere with analytical calculations using the equivalent circuit model. It indicates that the resonant peak has been heavily buried in the crosstalk. The “anti-resonance” peaks magnitude difference is about 0.035 mV, much smaller than the crosstalk 0.205 mV, and a maximum phase shift of 10° was observed around resonance. The quality factor for this resonator was found to be 1490, which is not a low value, but the crosstalk still obscures the resonator’s electromechanical signal.

2.2.3 Performance analysis

The output voltage U_o can be written as the sum of the mechanical resonance behavior U_M and the electrical crosstalk U_E , where

$$U_M(s) = -\frac{a^2}{\left(R_m s + L_m s^2 + \frac{1}{C_m}\right) C_s} U_i(s), \quad (2.2)$$

$$U_E(s) = \frac{C_{ft}}{C_{ft} + C_s} U_i(s). \quad (2.3)$$

The electrical behavior of the two port resonator can be illustrated by a polar diagram in the complex plane, as shown in Fig. 2.9. The mechanical resonance U_M is represented by an approximate circle; the electrical crosstalk U_E introduces an offset of the resonance circle toward the first quadrant. For this reason the magnitude of the resonator reaches a minimum first and then a maximum with increasing frequency. Furthermore, the expected phase shift of 180° in the frequency interval around resonance is smaller.

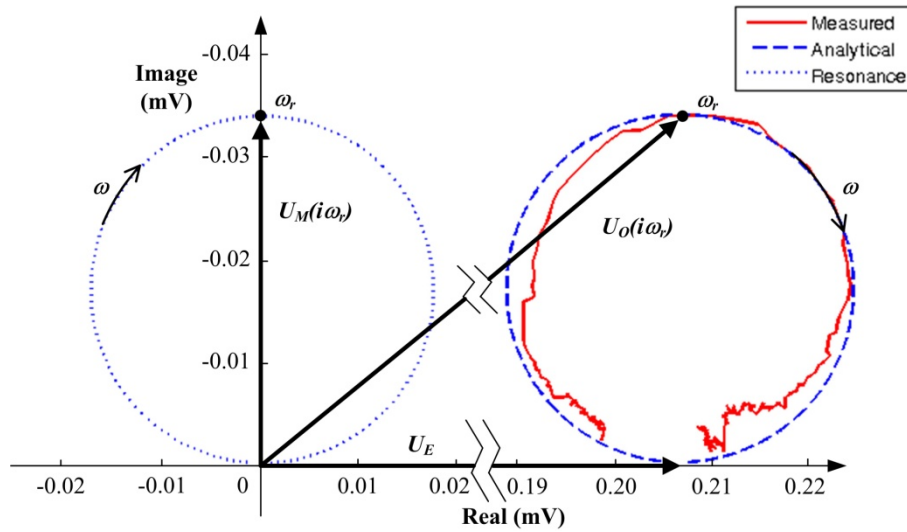


Figure 2.9: Measured and analytically calculated polar diagram of the resonator's response, the left circle shows the ideal resonance polar diagram without any crosstalk.

2.3 Crosstalk compensation solutions

The crosstalk makes the mechanical resonance less pronounced and the characterization of the resonator more difficult, thus calling for its compensation. Based on the above analysis, one can derive the physical sources of crosstalk: a) the electrical crosstalk comes mainly from the feedthrough capacitance C_{ft} , and b) C_{ft} is caused by the short circuit connection between drive and sense port grounds. Two approaches can be used to reduce/compensate the electrical crosstalk.

Firstly, the resonator structure and/or the geometry can be optimized to reduce the feedthrough capacitance by the following means: The shape of the piezoelectric layer can be optimized as to minimize crosstalk effects [110]; the bottom SCS electrode could be separated electrically by means of two anti serial p-n junctions [111]; two separated metal ground electrodes could be used [112]. Secondly, compensation techniques can be chosen. The basic idea is that the resonant signal can be picked up by the resonator output minus a dummy

signal which is equal to the electrical crosstalk. In this Section these two compensation methods will be described further, where the first method produces the dummy crosstalk signal on the same chip as the resonator under test, while the second one is realized by applying an external compensation voltage on the SCS bottom electrode.

2.3.1 On-chip compensation

In order to reduce the effect of the feedthrough capacitance C_{ft} , a capacitive compensation method could be employed, as shown in Fig. 2.10. The input drive voltage U_i is applied directly to the drive electrodes of the resonator, whereas a complementary voltage which is generated out of the drive is fed into the compensation capacitor C_{comp} , producing an output current i_{comp} . The resulting output currents from the resonator output and C_{comp} finally all add up at the sense node:

$$i_o = i_r + i_{ft} - i_{comp}, \quad (2.4)$$

$$\text{where } i_r = -\frac{a^2}{\left(R_m + L_m s + \frac{1}{C_m s}\right)} U_i(s), \quad i_{ft} = \frac{C_{ft} C_s s}{C_{ft} + C_s} U_i(s), \quad i_{comp} = \frac{C_{comp} C_s s}{C_{comp} + C_s} U_i(s).$$

The output voltage on the sense port shunt capacitor C_s is thus now given by:

$$U_o(s) = \left[-\frac{a^2}{\left(R_m s + L_m s^2 + \frac{1}{C_m}\right) C_s} + \frac{C_{ft}}{C_{ft} + C_s} - \frac{C_{comp}}{C_{comp} + C_s} \right] U_i(s). \quad (2.5)$$

Eq. (2.5) suggests that if C_{comp} closely matches the value of the feedthrough capacitance C_{ft} , the crosstalk can be reduced to:

$$U_o(s) = -\frac{a^2}{\left(R_m s + L_m s^2 + \frac{1}{C_m}\right) C_s} U_i(s). \quad (2.6)$$

The compensation capacitor C_{comp} can be realized on the same chip, as depicted in Fig. 2.11. The resonator in this design consists of several functional piezoelectric electrodes: drive electrodes, sense electrodes, and two compensation electrodes in the drive port and sense port separately. Here only the compensation electrode in the drive port is used. In order to insure $C_{d1} \approx C_{c1}$ and $C_{d2} \approx C_{c2}$, the area of the compensation electrode was designed to be equal to the area of the two drive electrodes. For this matching, the region on top of the suspended bridge has to be treated separately from the outside region, because the latter one has an

isolating SiO₂ layer in the piezo-electrode stack, whereas the former has none (refer also to Figs. 2.3 and 2.6). Since both the compensation electrode and drive electrodes are nominally identical in surface area, the feedthrough capacitance between the drive-sense and compensation-sense terminals can be expected to be closely matched ($C_{ft} \approx C_{comp}$).

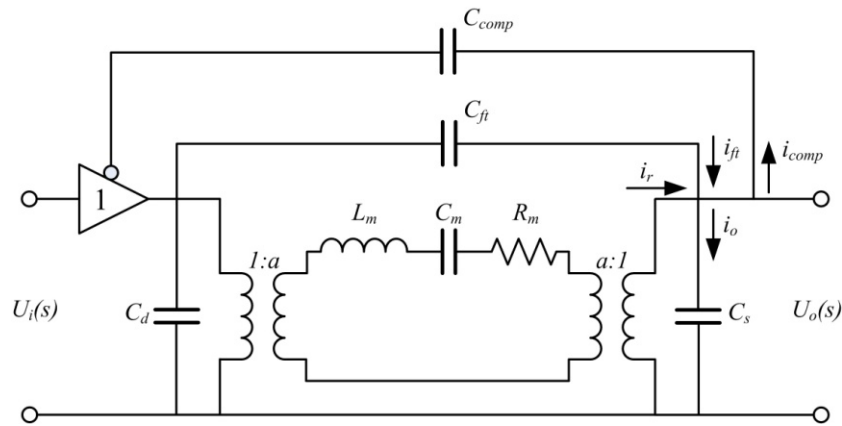


Figure 2.10: Schematic diagram of the feedthrough capacitance cancellation technique, using a compensation capacitor.

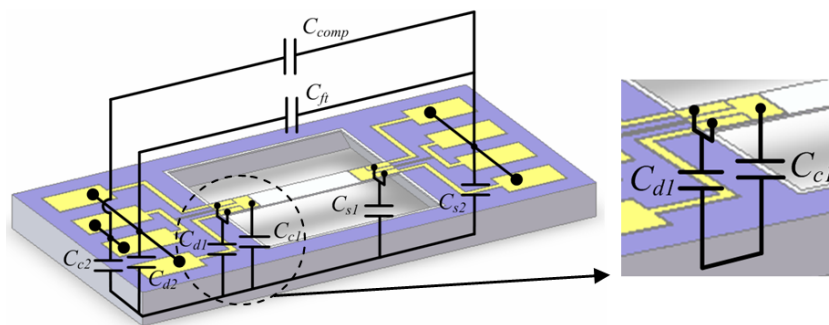


Figure 2.11: Simplified capacitance model for the piezoelectric resonator with an on-chip compensation electrode. There are two compensation electrodes in the drive port and sense port separately, only the one in the drive port is used.

The electric wiring diagram for on-chip capacitive compensation is shown in Fig. 2.12. Two complimentary drive voltages are applied to the drive and compensation electrodes, respectively.

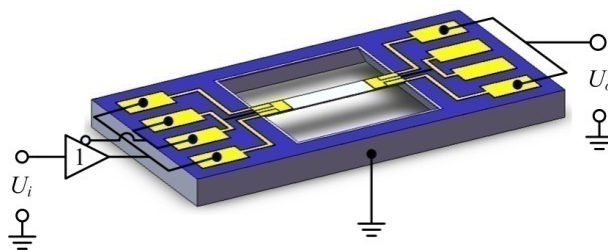


Figure 2.12: Electric wiring diagram for cancelling the feedthrough capacitance, using the on-chip compensation electrode in the drive port.

2.3.2 Electrical compensation

From eq. (2.3) one can find that the crosstalk has no phase shift with respect to the input voltage, the resonance signal can be picked up by the resonator output minus one portion of the input voltage, which is equal to the crosstalk. An electrical solution was developed to actively compensate the crosstalk; the corresponding schematic is shown in Fig. 2.13. Fig. 2.14 shows the electrical wiring for the electrical compensation solution. A drive voltage U_i is applied to the drive electrodes as normal, but the bottom electrode is connected with a voltage $-kU_i$ from an inverted voltage amplifier, where k is the adjustable gain of the amplifier.

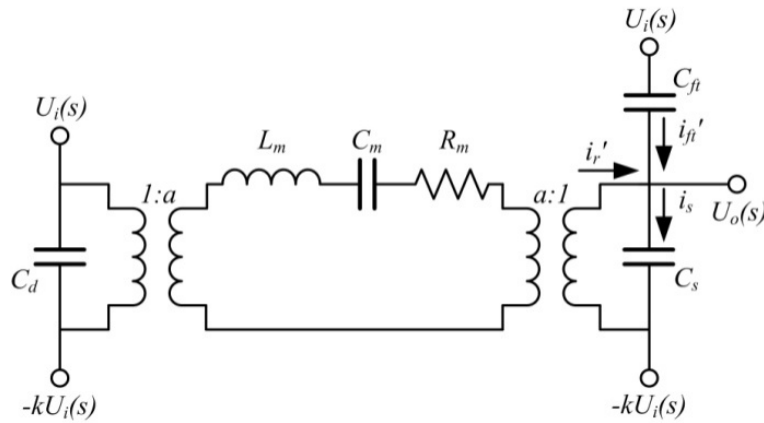


Figure 2.13: Schematic diagram of the feedthrough capacitance cancellation technique by applying an inverted voltage $-kU_i$ to the bottom electrode.

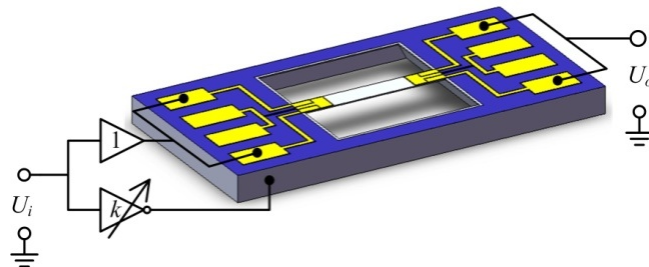


Figure 2.14: Electric wiring diagram for cancelling the feedthrough capacitance by applying an inverted voltage with adjustable gain k to the SCS bottom electrode.

After applying U_i and $-kU_i$ to the resonator's drive electrode and bottom electrode, the current on the sense port shunt capacitor C_s is:

$$i_s = i_r' + i_{ft}' , \quad (2.7)$$

$$\text{where } i_r' = -\frac{a^2}{\left(R_m + L_m s + \frac{1}{C_m s}\right)} U_i(s), \quad i_{ft}' = (1+k) \frac{C_{ft} C_s s}{C_{ft} + C_s} U_i(s) .$$

The differential voltage on the shunt capacitor C_s is:

$$\Delta U_s(s) = (1+k) \left[-\frac{a^2}{\left(R_m s + L_m s^2 + \frac{1}{C_m} \right) C_s} + \frac{C_{ft}}{C_{ft} + C_s} \right] U_i(s). \quad (2.8)$$

Since there is an inverted voltage $-kU_i$ at one end of the shunt capacitor C_s , the output voltage U_o at the other end of C_s can be obtained as:

$$U_o(s) = \left[-\frac{(1+k)a^2}{\left(R_m s + L_m s^2 + \frac{1}{C_m} \right) C_s} + \frac{(1+k)C_{ft}}{C_{ft} + C_s} - k \right] U_i(s). \quad (2.9)$$

By adjusting the gain k of the inverted voltage amplifier until $k = C_{ft}/C_s$,

$$U_o(s) = -\frac{(1+k)a^2}{\left(R_m s + L_m s^2 + \frac{1}{C_m} \right) C_s} U_i(s), \quad (2.10)$$

the influence of the feedthrough capacitance can be suppressed completely.

2.4 Electrical readout results

After the compensation of electrical crosstalk, a charge amplifier is used to amplify the resonator output signal. Fig. 2.15 shows the whole compensation-readout circuit, including the compensation parts described in Section 2.3, the charge amplifier, an additional variable gain voltage amplifier (in order to adjust the circuit output gain), a low pass filter and the chip socket.



Figure 2.15: Photograph of the compensation-readout circuit.

The results of the two compensation methods are presented in Fig. 2.16. The original uncompensated signal output is shown for comparison. Both compensation methods experimentally proved their efficiency for crosstalk reduction, since no significant anti-resonance could be observed.

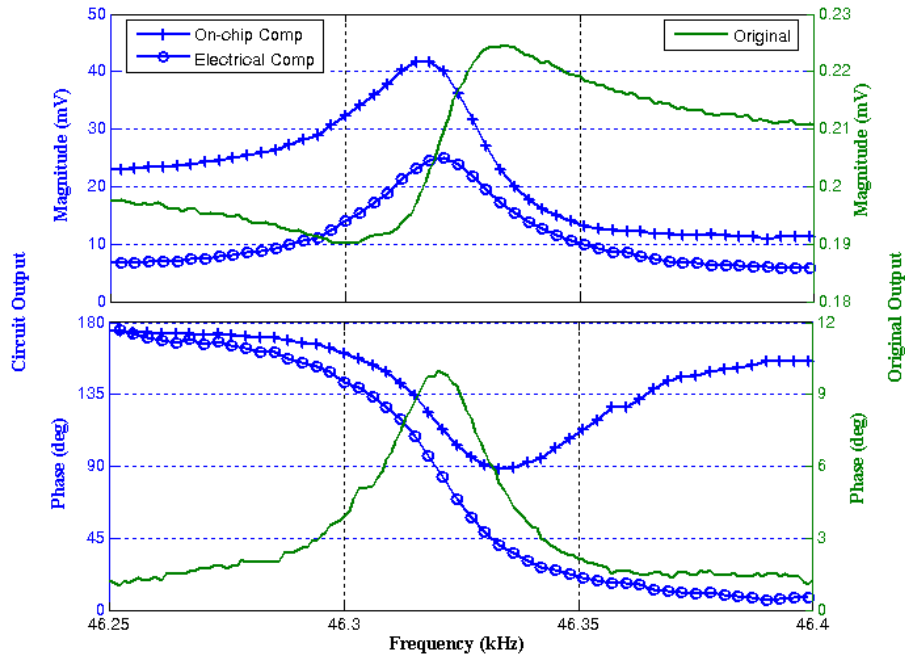


Figure 2.16: Results of on-chip compensation and electrical compensation of the piezoelectric resonator. The original uncompensated signal is shown for comparison.

For the on-chip compensation scheme there is an asymmetry in the magnitude of the frequency response around the resonance peak. This effect and also the behavior of the phase shift are an indication that the feedthrough capacitance has been over-compensated. We assume that this is because the compensation electrode is closer to the sense electrodes, as compared to the drive electrodes. Therefore, the feedthrough capacitance between compensation and sense ports C_{comp} is larger than the capacitance between drive and sense ports C_{ft} .

The output amplitude after electrical compensation is precisely symmetric around the resonance peak, and a phase shift of 90° occurs at resonance, indicating that the feedthrough capacitance has been adequately cancelled out, as the gain k of the inverted voltage amplifier has been tuned to closely match the requirement: $k = C_{ft}/C_s$.

The results from the on-chip compensation technique are not as good as from the electrical compensation, as there are some mismatches between the compensation and feedthrough capacitances. The compensation current i_{comp} can be tuned electrically to compensate the feedthrough current i_{ft} by either means of adjusting the level of the complimentary voltage or

compensation electrode size and/or position. Once the compensation electrode has been designed carefully to match well with the feedthrough capacitance, this technique would be promising for mass production as there is no adjusting element in the readout circuit. The second technique can achieve very good resonance output when the inverted voltage amplifier is sufficiently fine-tuned to cancel out the feedthrough effect. This adjustment can be done very easily and accurately with a variable resistor. For this reason this technique is widely used in the following work.

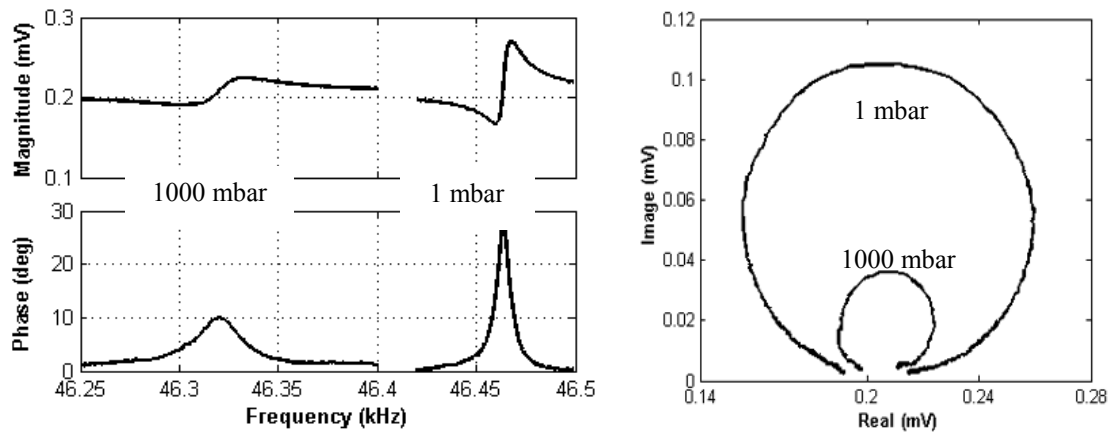


Figure 2.17: Measured amplitude and phase curves as well as polar plots of original resonator output at normal atmosphere and 1 mbar.

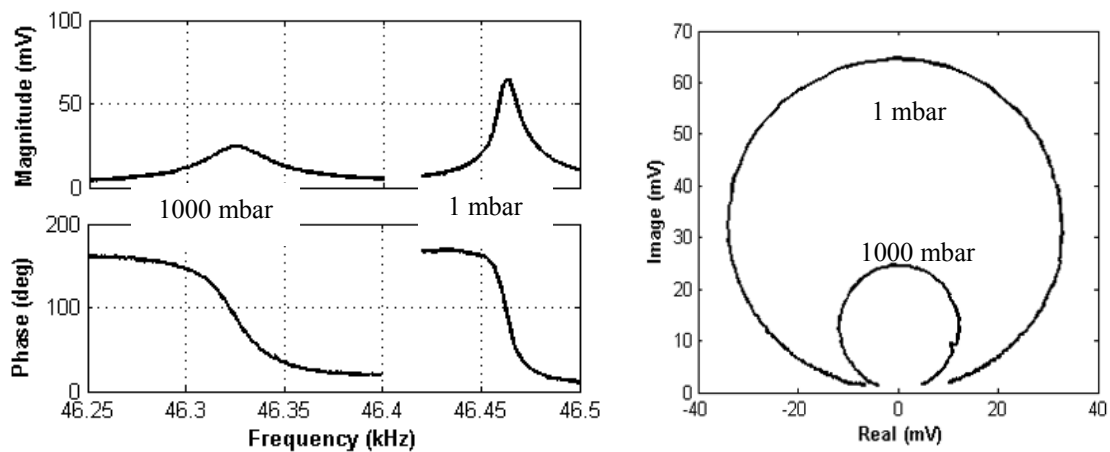


Figure 2.18: Measured amplitude and phase curves as well as polar plots of the output after signal conditioning at normal atmosphere and 1 mbar.

To characterize the performance of the resonators under different pressures and gas atmospheres, they were measured in a vacuum chamber under back pressures ranging from atmospheric conditions (≈ 1000 mbar) down to low vacuum obtained with a turbomolecular pump (measurement setup and results are shown in Chapter 3). Fig. 2.17 illustrates the measured resonator response without any circuit treatment (original output) under 1 mbar and under 1000 mbar pressures. For comparison, Fig. 2.18 shows the resonance signal after the

circuit treatment using electrical compensation. From these two figures it can be seen that, the electrical crosstalk in the resonator has been adequately cancelled out and the resonator output signal is much improved.

2.5 Conclusion

Piezoelectric beam resonators employing AlN as active film have been fabricated and tested. The effect of the input-output electrical crosstalk is found to be significant. Its origin is found to be mainly due to the feedthrough capacitance C_{ft} . It was analyzed and modeled, using an equivalent circuit model. In a polar diagram, the crosstalk introduces an offset of the resonance circle toward the first quadrant, making the mechanical resonance less pronounced and the characterization of the resonance behavior more difficult.

Two solutions were investigated in order to compensate the electrical crosstalk, by using a doubly-clamped beam resonator as example. The first solution is based on an additional on-chip compensation electrode, applying an inverted complementary voltage to it as compared to the drive electrodes. The second compensation method uses an adjustable inverted voltage amplifier, applying a compensation voltage to the SCS bottom electrode. After the compensation treatments the resonator output signal can be enlarged by a charge amplifier in both cases. The experimental results indicate that both compensation solutions are applicable and in excellent agreement with the theoretical predictions. In our experiments the matching of the on-chip compensation electrode was not as precise as expected, but it can be improved by design adjustments. Once this improvement has been achieved, the on-chip compensation is easier and more cost efficient for mass production, whereas the electrical compensation solution is more flexible with respect to individual precise adjustment. At the laboratory stage we are presently in, the latter method is commonly used with individual calibration for each resonator.

3. Experimental details and results

It is well known that oscillating structures can be profoundly influenced by the gas that surrounds them. In general, the dissipated energy for a resonator consists of internal energy losses (e.g. mechanical structure friction, radiation of elastic energy into the attachments: so called anchor-losses, etc.), and external losses (e.g. viscous, acoustic, and squeeze-film losses) into the surrounding fluid [21, 113]. The energy dissipated per cycle is the sum of the energy dissipated by each of these mechanisms. The total quality factor is dominated by the lowest component. The internal loss can be measured by operating the resonator in high vacuum. However, when operating in normal atmosphere, energy losses into the surrounding fluid are the main energy loss source. The surrounding fluid also affects the natural frequencies of the resonator. The cases on oscillators vibrating in fluid can be broadly divided into i) those that deal with vibration in unbounded fluids, ii) those that deal with vibration in a fluid bounded by a nearby surface.

Detailed measurements of the frequency responses of a series of micro beam resonators are presented in this Chapter. This work aims at evaluating and comparing systematically the effects of ambient pressure, the nature of the surrounding gas, resonator geometry, higher mode operation and the presence of a nearby surface on the resonance behavior. For this purpose, rectangular silicon beams with different geometries have been fabricated and tested in a number of gases under pressures varying from 10^{-4} – 10^3 mbar. To investigate the energy losses in a practically unbounded fluid, up to seven higher vibration modes are recorded in addition to the fundamental flexural resonance mode. For the case of vibrations in a bounded volume of fluid, a cover with cavity heights of 20, 50, 100, 150, 200, 250 and 300 μm , is clamped on the top surface of the resonator. Thus the mechanisms by which the closeness to the surface affects the quality factors and frequency shifts of the resonator can be explored.

The work in this Chapter demonstrates how the possible sources of damping affect the resonance behavior of micro resonators. It provides experimental data for modeling the resonator behavior in gaseous environment as well as in vacuum.

3.1 Experimental details

3.1.1 Measurement setup

The resonator is mounted on the setup with the electronic circuit (which was depicted in Chapter 2) and then placed in a custom-built vacuum chamber. The vacuum chamber is equipped with a turbo molecular pump and a rotary vane pump. The combination of a low

vacuum gauge (measurement range: 1000 to 0.1 mbar) and a high vacuum gauge (1 to 10^{-4} mbar) allows us to measure the pressure from atmosphere down to high vacuum (HV). Meanwhile, five noble gases (He, Ne, Ar, Kr, Xe) as well as N_2 , CO_2 and SF_6 are used to observe the resonator performance variation. During the measurement the maximum pressure is set to be 950 mbar, which is a little lower than normal atmospheric pressure (around 1000 mbar), in order to avoid the environment air leak into the chamber. The expression “atmospheric” pressure is referred to 950 mbar in this work. The gases are chosen for their significantly different properties. The noble gases are particularly interesting in this investigation since they have similar properties. They are all monatomic gases, with gradually increasing density (molecular mass) and decreasing heat capacity, thermal conductivity and speed of sound under standard conditions as their orders increase in the periodic table. Surprisingly, Ne has the highest dynamic viscosity η of all gases. Besides, He has the lightest density and highest heat capacity and a relatively low viscosity (H_2 was not used here for safety reasons), SF_6 is the densest gas that is stable and not toxic in normal atmosphere. CO_2 has similar density with Ar but different viscosity. A list of these gases with their properties is given in Tab. 3.1. Fig. 3.1 shows (a) the camera picture (the gas bottles are behind the chamber, not shown in the picture) and (b) the schematic diagram of the measurement setup used to characterize the resonator behavior.

Gas	Density ρ kg/m ³	Dynamic viscosity η Pa s 10 ⁻⁶	Heat capacity C_p J/(kg K) 10 ³	Thermal conductivity κ W/(m K)	Sound speed c_0 m/s	Specific heat ratio γ -	Molecular diameter d_0 m 10 ⁻¹⁰	Molar mass M kg/mol 10 ⁻³
He	0.178	19.68	5.2335	0.1513	1007	1.667	1.8578	4.00
Ne	0.9004	29.7	1.0216	0.0491	461	1.667	2.2660	20.18
Ar	1.784	22.8	0.5234	0.0177	319	1.667	3.0678	39.95
Kr	3.708	25.38	0.247	0.00949	221	1.667	3.4992	83.80
Xe	5.897	23.0	0.1583	0.00565	178	1.667	4.113	131.29
N₂	1.2506	17.9	1.0216	0.0258	343	1.4	3.1684	28.01
CO₂	1.977	14.83	0.8457	0.0168	267	1.333	3.8971	44.01
SF₆	6.18	15.66	0.658	0.135	134	1.1	5.1188	146.07

Table 3.1: Properties of different gases (at 20 °C and 1000 mbar).

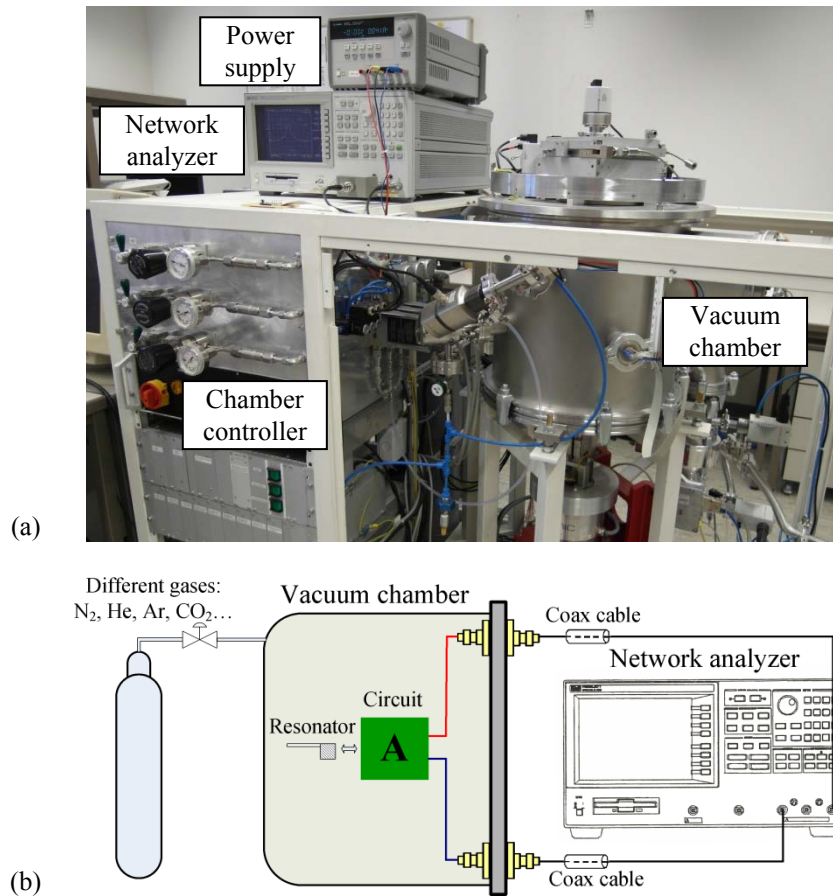


Figure 3.1: (a) The camera picture and (b) the schematic diagram of the measurement setup used to characterize the micro resonators in the vacuum chamber.

3.1.2 Device geometry and packaging

Three sets of resonators are fabricated and used in this study, a schematic depiction of which is given in Fig. 3.2. The first set of resonators is suspended from one side only, henceforth referred to as cantilevers. Their length-width ratio l/w varies from 3 to 11. The second set of resonators is doubly clamped, and is therefore referred to as bridge. The third set is referred to as plate with single side suspension. The plate resonator differs from normal cantilevers since l/w is around 1. Besides, in order to compare the cantilever and plate resonator behaviors at a similar frequency range, there is an etched hole near the clamped end in some plate resonators. The width w of cantilevers and bridges was set at 100, 200, 400 and 800 μm , and the length l of cantilevers was varied at 1200, 1540 and 2200 μm , while l of bridges was set at 3400 μm . The plate resonators have two $l-w$ combinations: 2000-1600 μm and 2900-2400 μm . The thickness t of the resonators was designed to be 20, 40 and 60 μm , and determined by the wafer thickness and wet etching process. In our fabrication process, the thickness variation was controlled to below $\pm 3 \mu\text{m}$. The exact thickness of individual resonators can be calculated by comparing the simulated resonance frequency with the measured resonance

frequency in HV. The detailed resonator geometries are listed in Tab. 3.2.

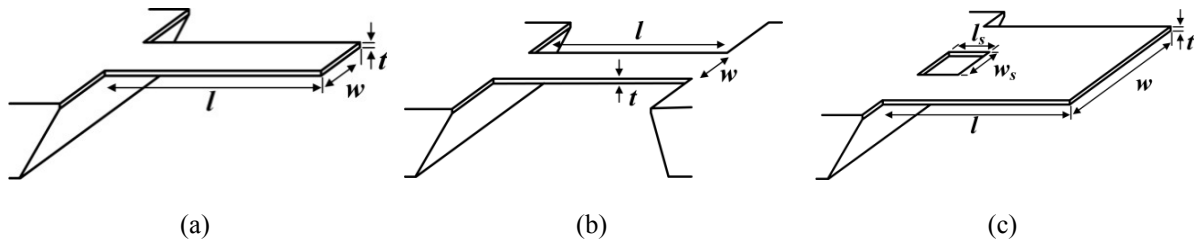


Figure 3.2: The basis resonator structures: (a) cantilever, (b) bridge and (c) plate.

Structure	Nr.	w (μm)	l (μm)	t (μm)	w_s (μm)	l_s (μm)
Cantilever	<i>C1</i>	200	1200	18.4	-	-
	<i>C2-I</i>	200	1540	18.8	-	-
	<i>C2-II</i>	200	1540	37	-	-
	<i>C2-III</i>	200	1540	58	-	-
	<i>C3</i>	200	2200	17.7	-	-
	<i>C4</i>	400	1200	20	-	-
	<i>C5</i>	400	1540	22.5	-	-
	<i>C6-I</i>	400	2200	22	-	-
	<i>C6-II</i>	400	2200	37	-	-
<i>C6-III</i>	400	2200	57.2	-	-	
<i>C7</i>	800	1200	23	-	-	
<i>C8</i>	800	1540	17.2	-	-	
<i>C9</i>	800	2200	18	-	-	
Bridge	<i>B1</i>	200	3400	21.2	-	-
	<i>B2</i>	400	3400	21	-	-
	<i>B3</i>	800	3400	20.5	-	-
Plate	<i>P1</i>	1600	2000	18	440	450
	<i>P2</i>	2400	2900	19.5	1800	500

Table 3.2: Resonator geometries.

Two resonator packaging methods were used in this work, to investigate the gas flow force and squeeze force effects individually. For the first case, the resonator chip was die-mounted on a printed circuit board (PCB) package, with a hole pre-drilled on the board, as shown in

Fig. 3.3. In this package, the resonator is suspended several millimeters away from any bottom surface, much bigger compared to the resonator width, the influence of the bottom surface on the resonance spectrum is minimum. So this packaged set can be used to investigate the resonator vibration in unbounded fluid, especially under reduced pressure.

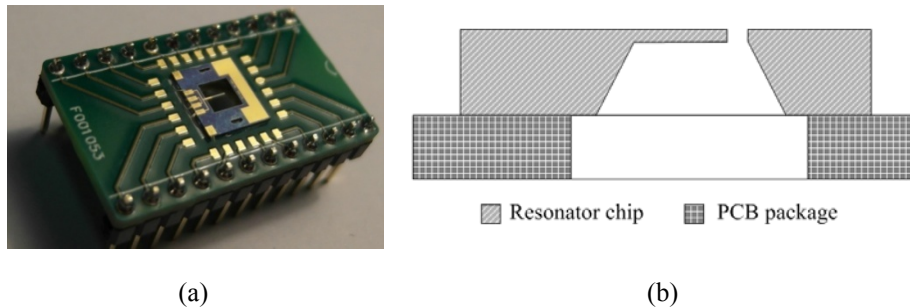


Figure 3.3: (a) The photo of a packaged chip for gas flow evaluation and (b) the schematic cross section view of the setup.

To understand how fluid viscous dissipation is modified when the microcantilever is brought close to a surface and simultaneously allowing maximum flexibility for combining different cantilever structures with varying squeeze film gaps, a special mounting technology was used. Fig. 3.4 schematically shows the resonator packaging setup for “squeeze film” evaluation. In order to allow maximum flexibility for combining different resonators with varying squeeze film gaps, a top cover was clamped on the structure surface using a clip. For small cavities (20, 50, 100 and 150 μm), silicon wafers were wet etched to create the certain depth cavity, and for large cavities (200, 250 and 300 μm), aluminum blocks were used as the top cover, which were manufactured by conventional mechanical milling processes.

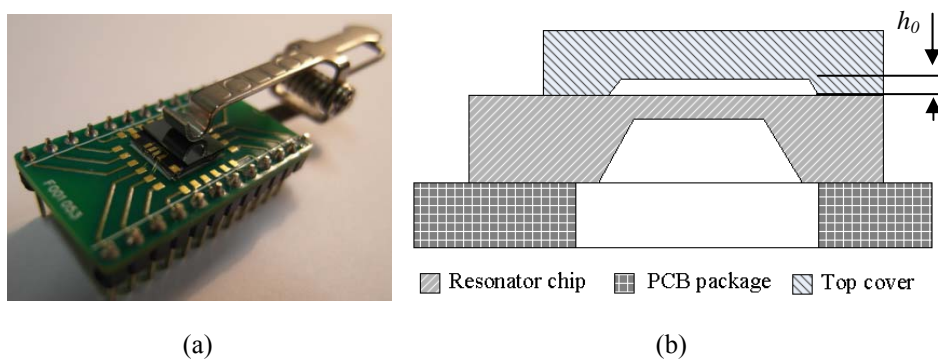


Figure 3.4: (a) The photo of a packaged chip for squeeze film evaluation and (b) the schematic cross section view of the setup.

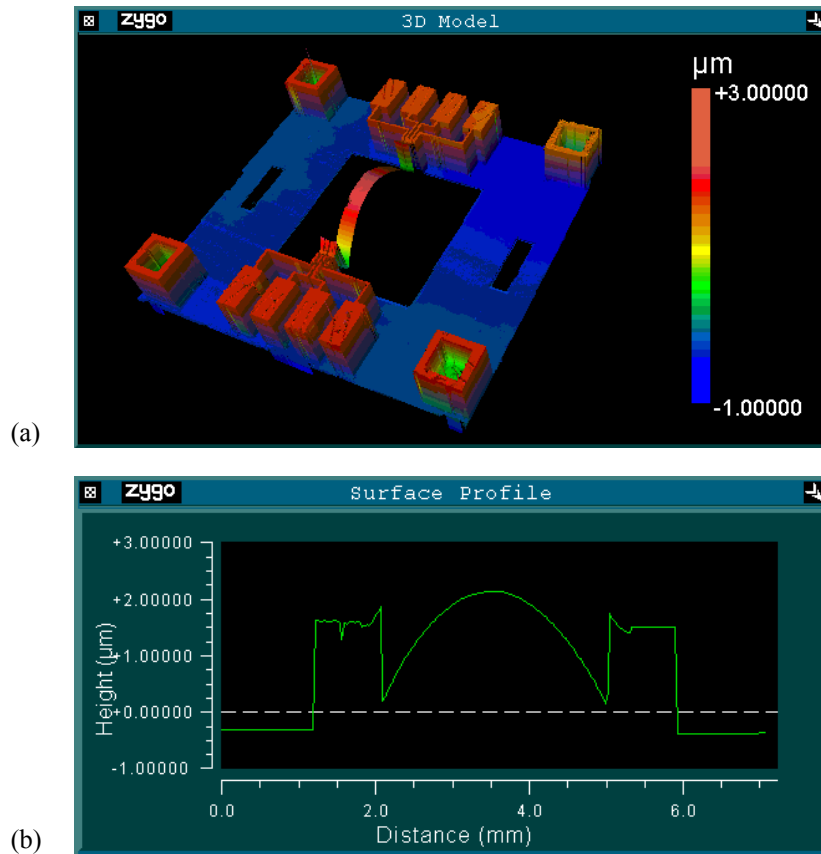


Figure 3.5: (a) 3D illustration of the surface and (b) the surface profile of a bridge resonator.

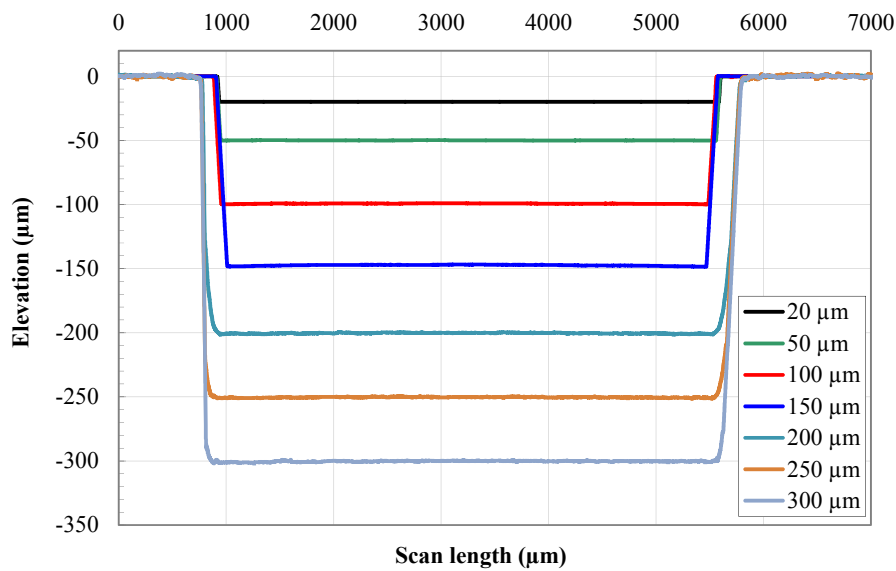


Figure 3.6: Surface profiles of the top covers.

The gap height h_0 is an important parameter in this study. Accurate characterization of the gap height h_0 depends on the resonator bending due to internal stresses and silicon wet etching timing or mechanical fabrication tolerance. White-light interferometer measurements were carried out to determine the resonator self-bending. The deflections of cantilevers at the tip point are normally in the range from 10 ~ 20 μm, whereas, due to the doubly clamped

configuration, the deformations of bridge resonators are much smaller ($< 3 \mu\text{m}$). So the bridge resonators were selected for squeeze film measurements. Fig. 3.5 shows a typical surface profile of bridge resonator. The surfaces of the top covers were measured using a profilometer and are shown in Fig. 3.6.

3.1.3 Resonator characterization

By sweeping the actuation frequency across the resonance frequency, one can get the harmonic frequency response of the device, from which the damping characteristic of the device can be extracted. The response curve was fitted by using a second order equivalent circuit model. In real measurements, due to the nonlinearity of the real circuit, an offset voltage U_{off} was added to the fit function. Finally the output voltage can be written as

$$U_o(s) = U_{off} + \frac{1}{R_m s + L_m s + 1/C_m} U_i(s). \quad (3.1)$$

The resonance frequency and Q factor can be calculated from this model by

$$f_r = \frac{1}{2\pi} \sqrt{\frac{1}{C_m L_m}}, \quad Q = \frac{1}{R_m} \sqrt{\frac{L_m}{C_m}}. \quad (3.2)$$

Fig. 3.7 displays the frequency response from a micro bridge resonator at 1000 mbar, together with a fit result, which yields the resonance frequency $f_r = 46.325 \text{ kHz}$ and quality factor $Q = 1691.8$.

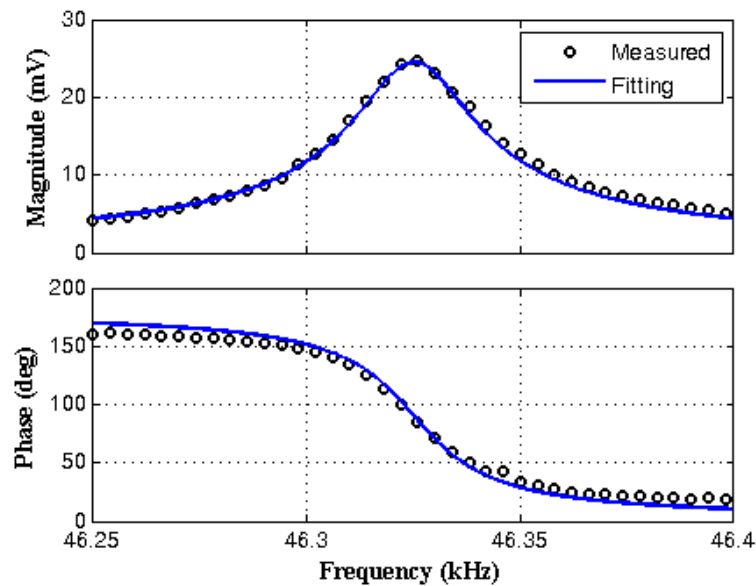


Figure 3.7: Measured resonance (circles) with fitting curves (solid line) according to eq. (3.2) yielding the fit parameters $f_r = 46.325 \text{ kHz}$ and $Q = 1691.8$.

3.2 Dynamic response of micro resonators vibrating in unbounded fluid

Broadly speaking, the dissipation of the mechanical vibration energy of a micro resonator can occur due to acoustic radiation and viscous losses in the surrounding fluid, internal friction and support loss in the structure, etc. However, at the micrometer scale, energy losses in the surrounding fluid are typically much greater than other losses combined. The surrounding fluid also affects the natural frequencies of the microbeam. The cases on microbeam vibrating in fluid can be broadly divided into i) those that deal with a microbeam vibrating in unbounded fluid, ii) those that deal with a microbeam vibrating close to a surface. The first case is investigated in this Section.

3.2.1 Micro resonator performance at the first flexible mode

The resonators were tested under controlled pressure from HV pressure to normal atmosphere. The resonance frequencies and Q factors were characterized as a function of the ambient pressure. Apparently, when vibrating in a vacuum, the gas damping on the resonator is minimized and a high Q value can be achieved. Increasing the pressure by starting from HV conditions results in a slight shift in the resonance frequency but a dramatic reduction in the Q factor, as demonstrated by the example resonance curves shown in Fig. 3.8, which is the measurement of a microcantilever in N_2 atmosphere for the first flexural mode. The cantilever is numbered as *C6-I*, and its nominal dimensions can be found in Tab. 3.2.

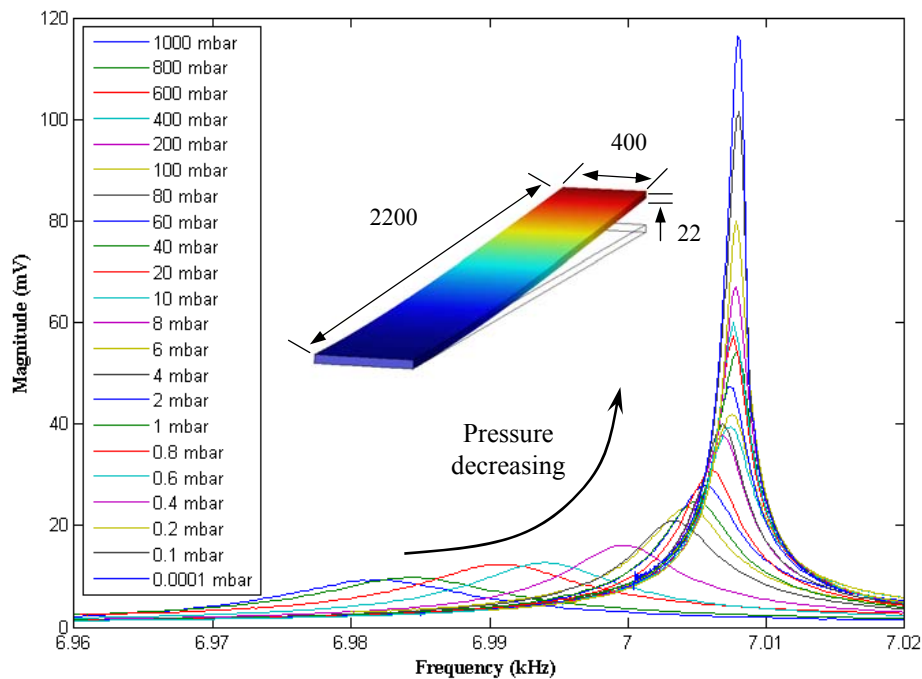


Figure 3.8: Resonant measurements of the cantilever under the pressures from HV to 1000 mbar in N_2 environment for the first flexural mode. The insert shows the resonance mode and cantilever dimensions (in μm).

The resonance frequency shift is illustrated in Fig. 3.9. The corresponding resonance frequency was changed from 6.981 kHz at atmosphere pressure to 7.008 kHz at 1 mbar. When the pressure is decreased further, the resonance frequency stays constant within the measurement accuracy. Fig. 3.10 shows the measured Q factors of the cantilever as a function of the chamber pressure. The Q factor is 530 at atmosphere pressure and increases as the pressure decreases, but this tendency in lower pressure is limited by intrinsic damping effects occurring in the mechanical structure [114], the Q factor finally reaches its maximum value, as high as 6900 at 0.001 mbar. As observed from both Q factors and resonance frequency shifts, at higher pressure levels the interaction between cantilever and the residual gas atmosphere is in both cases the dominating losses mechanism. Gas damping becomes less effective if the back pressure reduced.

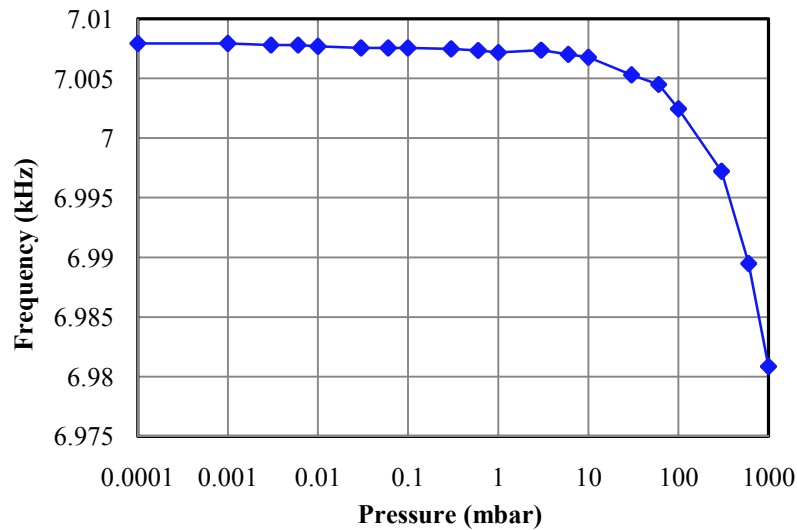


Figure 3.9: Resonance frequency shift for the first flexural mode as a function of ambient pressure in N_2 atmosphere.

The measured Q factor is a composition of the intrinsic Q factor Q_{int} and Q_{gas} due to gas damping, following the relationship:

$$Q^{-1} = Q_{int}^{-1} + Q_{gas}^{-1}. \quad (3.3)$$

When the ambient pressure was below 10^{-3} mbar, no differences in the resonator output could be observed; so the Q factor below this pressure is assumed to be the resonator's intrinsic Q factor Q_{int} and this pressure regime is called:

- *Intrinsic regime*: the pressure is at sufficiently low vacuum level so that gas damping is negligible. The intrinsic losses within the resonator materials dominate the performance. The damping effect comes exclusively from energy dissipation mechanisms inside the solid structure.

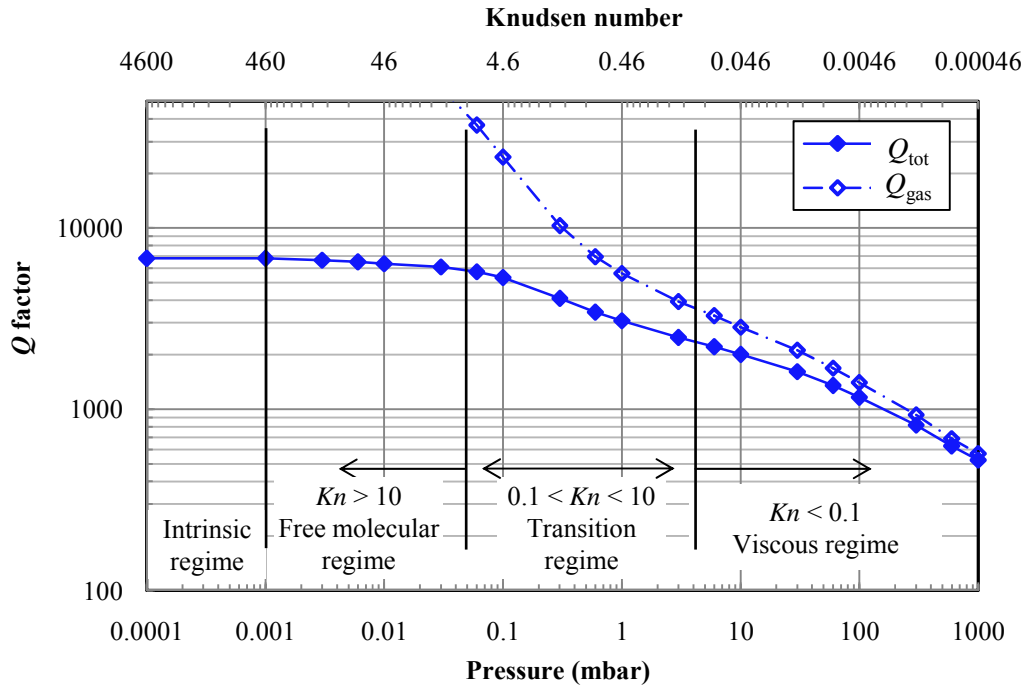


Figure 3.10: Variation of Q factor with ambient pressure in N_2 environment for the first flexural mode. The solid diamond points are the measured Q factors, while the hollow points are the calculated Q factors purely due to gas damping, by separating mathematically the intrinsic damping.

Gas damping starts to increase energy losses in the microcantilever when the ambient pressure exceeds the levels of the intrinsic regime. Different damping regions can be identified by using the Knudsen number Kn . The Knudsen number is given as the ratio between the mean free path of the gas λ and the characteristic length scale of the flow. For the cantilever without a gap to a nearby surface the characteristic length is considered to be the width of the cantilever w [115]

$$Kn = \lambda/w. \quad (3.4)$$

The mean free path is inversely proportional to density and may be calculated using

$$\lambda = \frac{K_b T}{\sqrt{2\pi p d_0^2}}, \quad (3.5)$$

where $K_b = 1.38 \cdot 10^{-23}$, is the Boltzmann constant, T is the ambient temperature, p is the ambient gas pressure.

Depending on the pressure level, three different gas damping regions can be identified [115]:

- *Molecular regime* ($Kn > 10$): damping is caused by independent collisions of non interacting gas molecules with the vibrating surface of the resonator; the energy loss is proportional to the gas pressure p [116, 117]. However, since the intrinsic damping is much higher than the gas damping in the example shown above, we cannot observe

directly a significant pressure dependence.

- *Transition regime* ($0.1 < Kn < 10$): the gas is neither non-interacting nor continuous. The analysis using particle simulation like direct simulation Monte Carlo (DSMC) approaches [118] must be employed [119-121]. Although recently an analytical solution in the transition regime has been proposed by Yakhot *et al.* [122-126], it does require several fitting parameters which are different with respect to different resonators and gases. They need to be determined experimentally [127, 128]. Detailed investigation in this regime is out of this research scope.
- *Viscous regime* ($Kn < 0.1$): the gas acts as a continuous viscous fluid and the viscous drag is typically the dominant loss mechanism, with a \sqrt{p} pressure dependence [37, 129]. In the case shown in Fig. 3.10, above 10 mbar the quality factor is influenced markedly by the ambient gas and Q_{gas} exhibits an inverse square root dependence on pressure, implying that viscous damping is dominant. For the case that the micro resonator vibrates in unbounded gas, we will focus on the gas damping in the viscous regime.

3.2.2 Dependence of micro resonator response on ambient pressure, gas and geometry

In order to determine the resonator performance dependence on gas species, the resonator was tested in the chamber filled with different specific gases under controlled pressure. Fig. 3.11 shows the resonance frequency shifts as a function of pressure for different gases. The results indicate clearly that the resonance frequency decreases as the density (molecular mass) of the gas increases. Furthermore, in Fig. 3.12, the normalized frequency shift $\Delta f / f_{r,HV}$, which equals to $(f_{r,HV} - f_r) / f_{r,HV}$ is plotted as a function of gas density, where $f_{r,HV}$ corresponds to the resonance frequency f_r in HV. In the inset to Fig. 3.12, the relative resonance frequency shift is plotted as a function of the density ρ of the gas at atmospheric pressure. The resonance frequency shift changes from 0.09% (He) to 1.69% (SF₆) as the density increases from 0.178 to 6.18 kg/m³, respectively. The results in Fig. 3.12 indicate a clear linear dependence of the resonance frequency shift on the density of the gas. Although the dynamic viscosities of the eight gases vary between 14.83 and 29.7×10⁻⁶ Pa s, no direct dependence of the resonance frequency shift on the dynamic viscosity is observed.

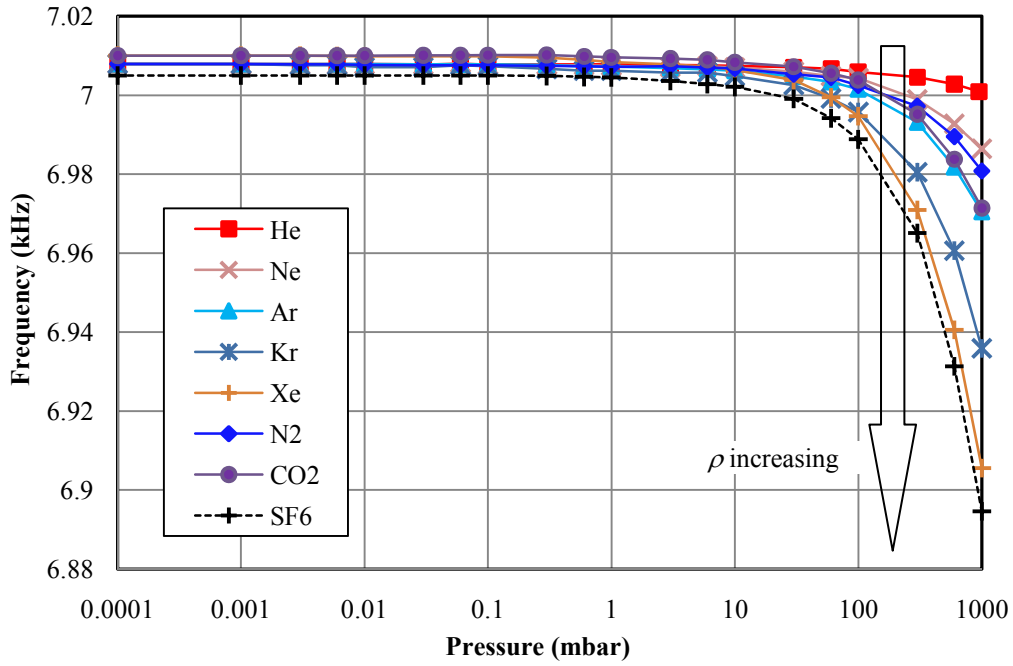


Figure 3.11: Resonance frequency shifts with ambient pressure and different gases for the resonator in its first mode.

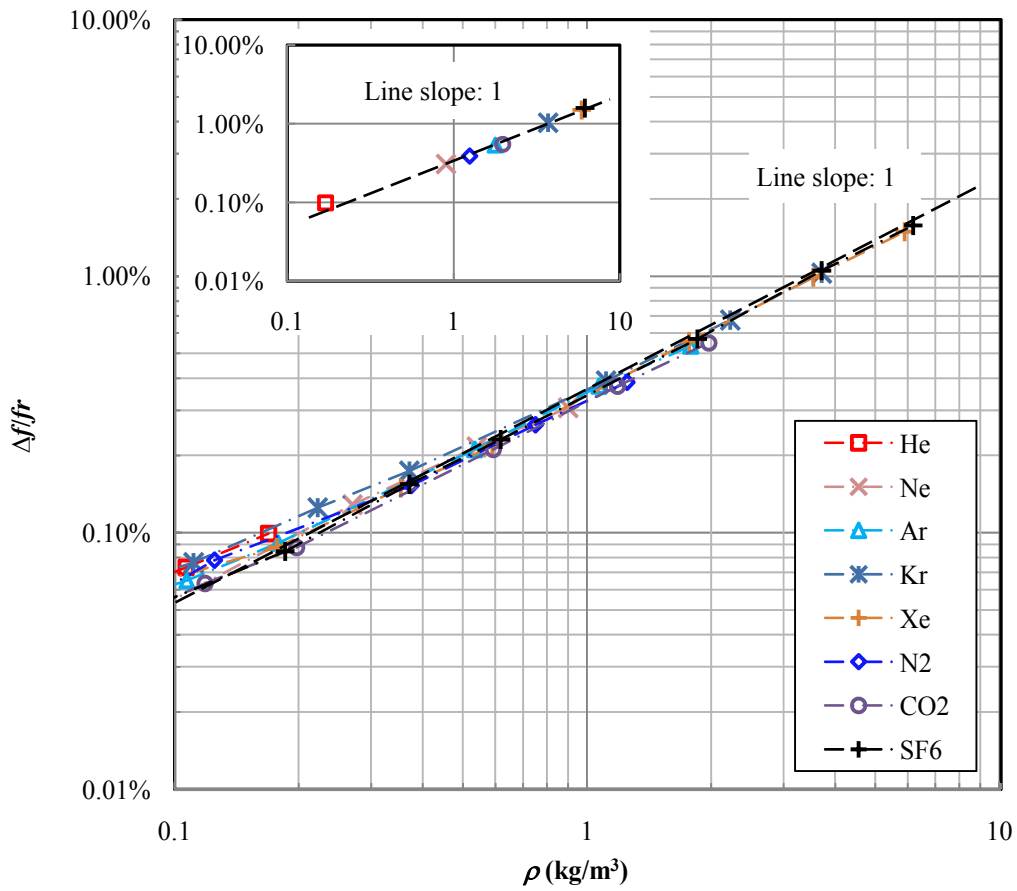


Figure 3.12: Normalized frequency shifts as a function of the density ρ of the gases under different pressures. The insert figure shows the results for atmospheric pressure only.

Fig. 3.13 presents the Q factor dependence on pressure of this resonator for different gases. It has been shown that Q factors are very sensitive to density and viscosity of the surrounding fluid. Q factors Q_{gas} due to gas damping in the viscous regime are derived and shown in Fig. 3.14, and replotted in Fig. 3.15 as a function of the product of the density ρ and the dynamic viscosity η of the surrounding gases at reduced pressure. The inset shows the relationship at atmospheric pressure, only. It indicates a clear dependence of Q_{gas} on $\sqrt{\rho\eta}$. This further confirms that for slender structures viscous loss is proportional to the square root of the gas pressure \sqrt{p} .

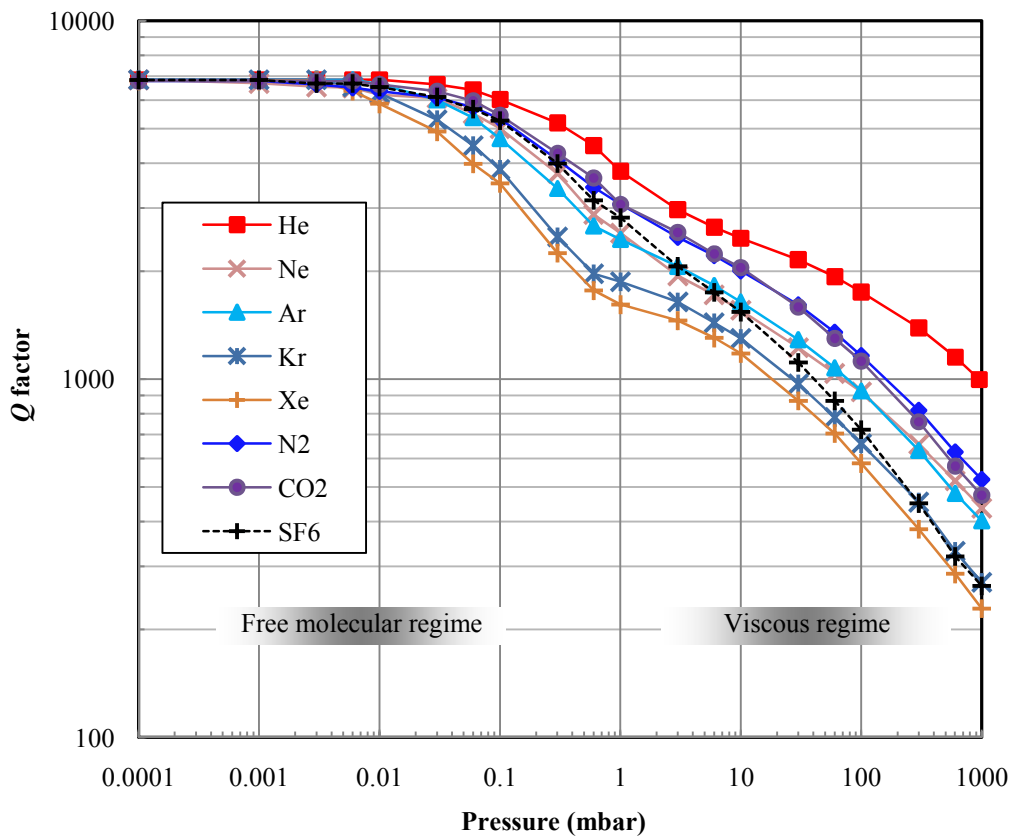


Figure 3.13: Variation of Q factors with ambient pressure for different gases with the resonator in its first flexural mode.

These results further confirm that, by analyzing the frequency response of a cantilever in a fluid, the viscosity and density of the fluid can be determined. Only gases with identical density and viscosity will give the same resonance frequency and Q factor. Gases that have similar viscosities or densities can be easily distinguished with this technique. As an example, consider CO_2 and Ar at 20°C and 1000 mbar, which have similar densities (1.977 and 1.784 kg/m^3) but significantly different viscosities (14.83 and $22.8 \text{ Pa s } 10^{-6}$), we find that the measured spectra in these two gases have nearly identical resonance frequencies (6.971 and

6.970 kHz), yet their quality factors are different (474 and 402).

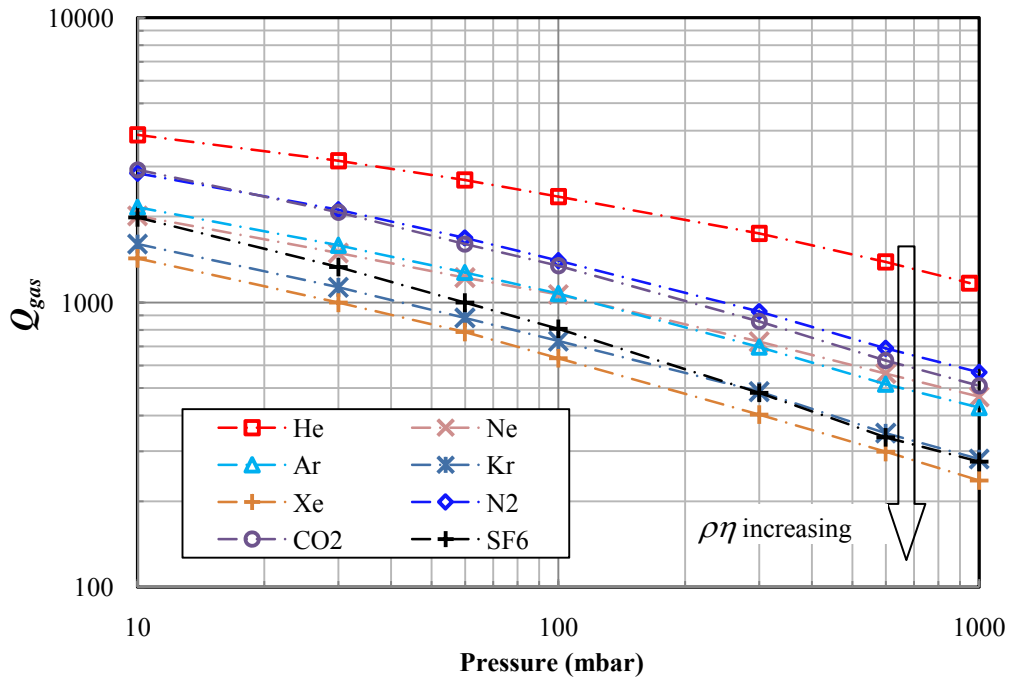


Figure 3.14: Variation of the Q factor due to gas damping in the high pressure regime (approx. viscous regime) for different gases with the resonator in its first flexural mode.

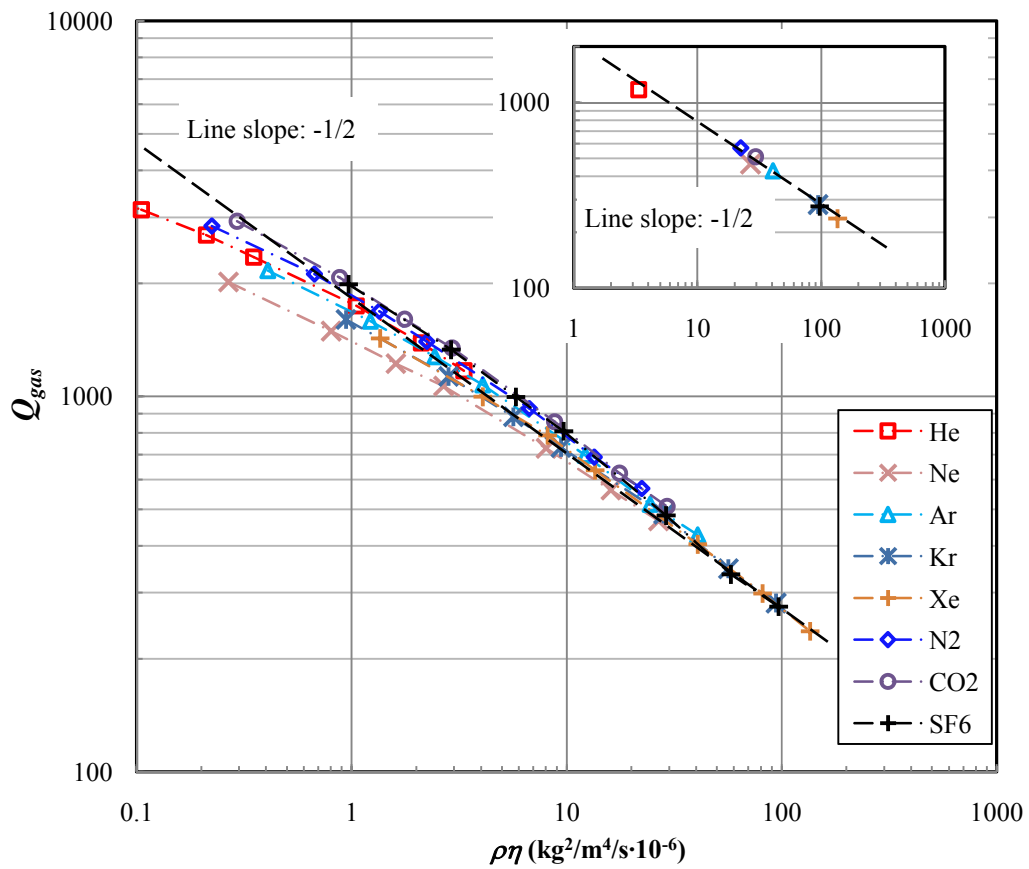


Figure 3.15: Evolution of the Q factors as a function of the product of the density ρ and the dynamic viscosity η of the gases under different pressures. The insert figure shows the results at atmospheric pressure only.

We now discuss the Q factor dependence on the geometry of microcantilevers operating in vacuum condition. Fig. 3.16 shows the measured Q factors of the cantilever with different lengths l and widths w in HV, which is in the intrinsic regime, and under atmospheric pressure in N_2 , and Fig. 3.17 shows the measured Q factors for cantilevers with different thicknesses t . It can be seen that the Q factor in HV increases with increasing l and decreasing t , while at atmosphere it shows the opposite trend. At 1 bar the results are almost independent on the width w . In the intrinsic regime the results show a nonintuitive dependence on the width. Moreover, the quality factors in HV of a cantilever fully covered with a piezo-electrode stack are included in Fig. 3.16. All other resonators are covered by the piezo stack with a fill factor of 20-60% over the cantilever length. It can clearly be seen that the cantilever with a reduced cover layer pattern results in a markedly improved quality factor.

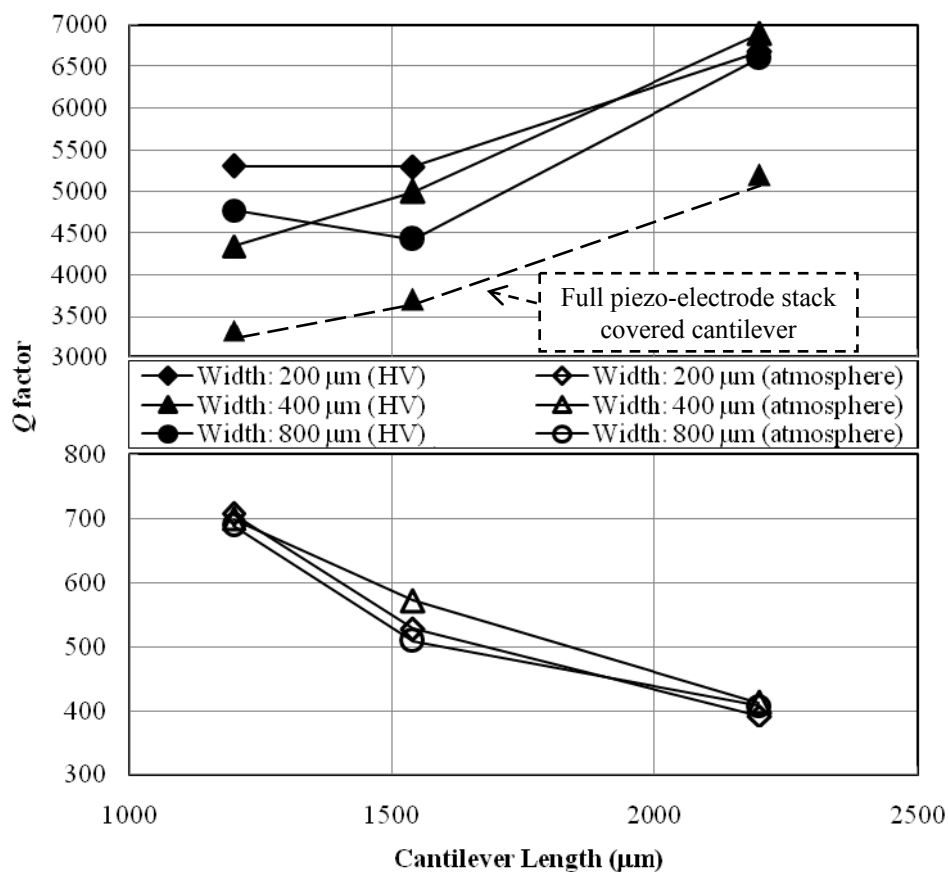


Figure 3.16: The Q factors of cantilevers with different widths and lengths. The Q factors of fully piezo-electrode stack covered cantilevers in HV were included for comparison.

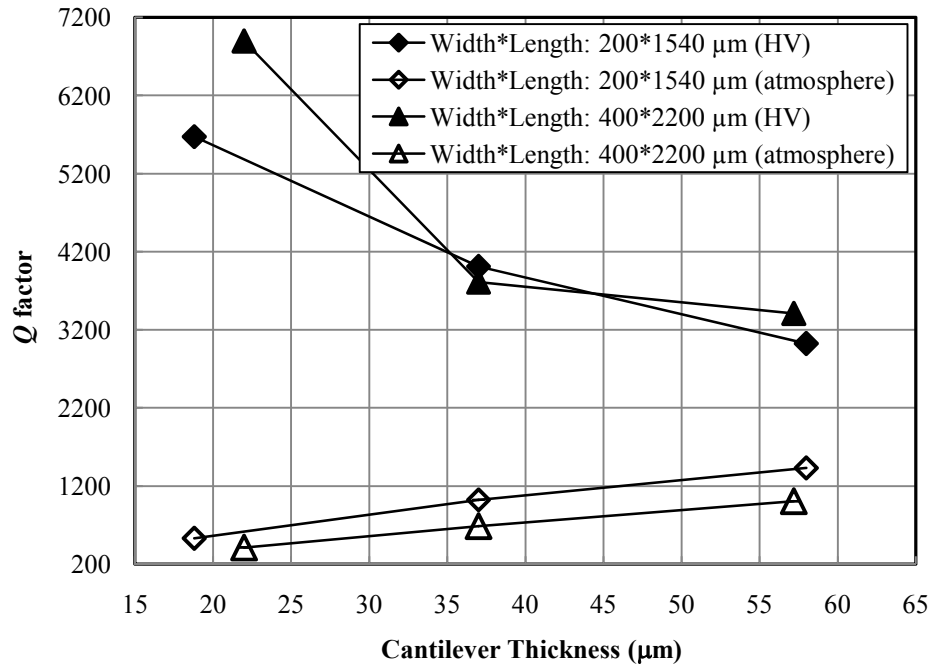


Figure 3.17: The Q factors of cantilevers with different thicknesses.

3.2.3 Micro resonator performance at higher modes

Up to now, most of the published research work was focused on the gas flow damping effect of resonators operating in their fundamental first flexural mode. More recently, however, attention begins to be paid to resonators operating at higher flexural or torsional modes [58-60, 130, 131]. So far, in individual studies, individual resonance modes of resonant cantilevers are developed and used. With the results obtained from different cantilever designs and different experimental conditions, it is difficult to compare them and to judge which mode is superior. In this work the performance of microcantilevers in different orders of flexural, lateral and torsional modes are systematically evaluated and compared.

The cantilever resonator *C6-I* was tested first. To excite the resonator in higher modes, the applied driving voltage frequency was scanned from 5 kHz to 500 kHz. Seven resonant modes of the cantilever have been detected and characterized, which are the first to fourth flexural modes, the first lateral mode, and the first and second torsional modes, respectively. Finite element analysis software COMSOL was used to assign the resonant modes to the observed peaks. A comparison between simulated and experimentally observed frequencies is shown in Tab. 3.3. Fig. 3.18 shows the resonance frequencies and amplitudes of the cantilever in normal atmospheric N_2 . The resonant mode shapes inserted in the figure were obtained by COMSOL software, depicting the displacement of the cantilever for each mode.

Mode	1st flex.	2nd flex.	1st tors.	1st later.	3rd flex.	2nd tors.	4th flex.
f_e	7.0	41.1	73.6	95.5	112.6	212.7	225.5
f_s	6.6	41.5	74.1	110.3	116.3	219.6	228.3
Error	5.71%	0.97%	0.68%	15.50%	3.29%	3.24%	1.24%

Table 3.3: Comparison of experimentally observed resonance frequencies f_e (kHz) and COMSOL simulated frequencies f_s (kHz).

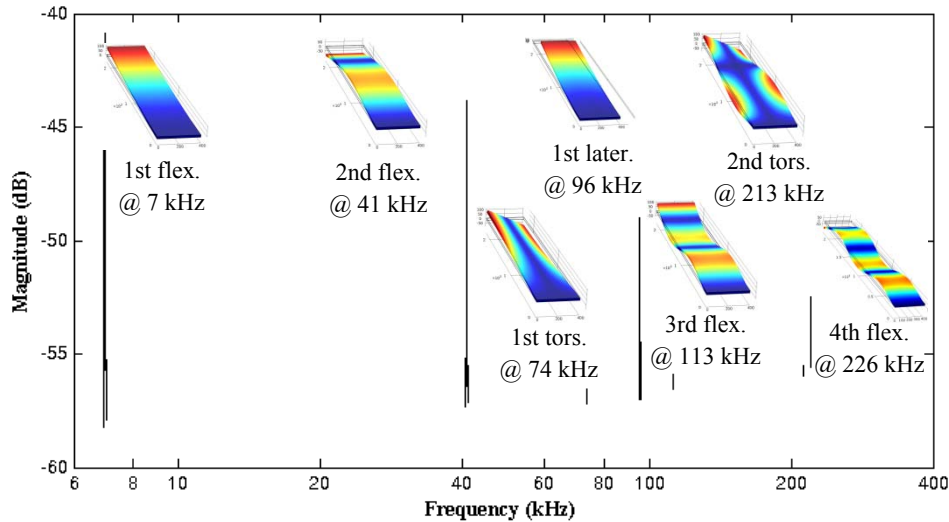


Figure 3.18: Amplitude spectrum and mode shapes of the cantilever at normal atmospheric N_2 .

The Q factors of different modes were characterized under different pressures varying from 10^{-4} mbar (HV) to 950 mbar (atmosphere). When the ambient pressure was even lower no differences in the resonator output could be observed. So the results at 10^{-4} mbar pressure are assumed as the intrinsic output of the resonator. The Q factors from the measurements are summarized in Fig 3.19, from which one can find that, the mode shape has a big effect on the performance of the resonator.

The torsional modes exhibit higher Q factors than all other types of modes over the whole observed pressure range. This phenomenon is consistent with measurements found in the literature [56, 132 and 133]. Unlike the bending strain under flexural or lateral motion in the silicon membrane and the top piezo-electrode stack strips, the generated shear strain under torsional motion is unaffected by volume tension or compression. This can effectively suppress volume-change-induced energy dissipation [134]. Moreover, the tuning-fork-like antiphase movement between the double sides of the torsional cantilever is expected to feature a high quality factor in gaseous environment.

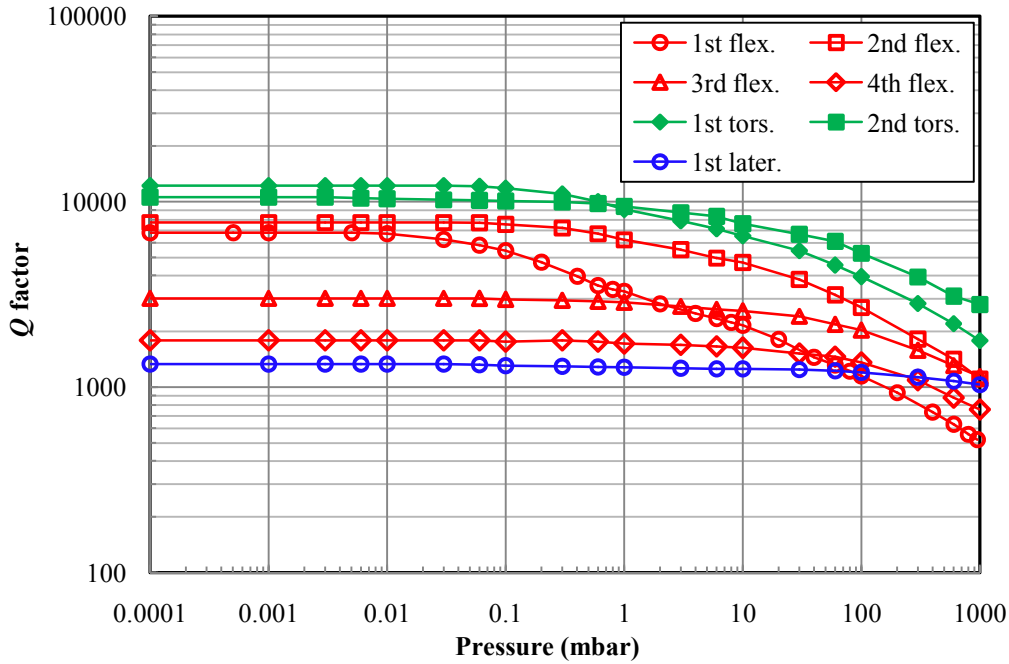


Figure 3.19: The Q factors of different modes as a function of ambient pressure.

The Q factor of the lateral mode stays almost constant in low pressure and starts to decrease until the pressure is close to 1 bar. The gas damping energy loss in the lateral mode is expected to be lower, since the beam is shearing with its width and only compressing the gas with its much smaller thickness. However, the intrinsic energy loss was found to be the highest for all observed modes, so that the effect of gas damping is only observed at pressures close to 1 bar. The high intrinsic loss is expected to be mainly due to the larger support loss as compared to other modes [94].

While the quality factor changes for the flexural modes are found to be complex. The Q factors for the flexural modes at different pressures are extracted in Fig. 3.20. The intrinsic energy loss is found to increase when the mode number is higher than 2. For the 3rd and 4th flexural modes, the thermoelastic damping (TED) loss was found to play an important role in the internal losses. According to Ref. [83, 84], Q_{TED} has a minimum when vibrating at thermal relaxation frequency F_0 , where the heat energy generated from the material internal friction dissipates completely. For the cantilever in this case, F_0 is calculated to be around 235 kHz, the resonance frequency of the 3rd (112.6 kHz) and 4th (225.5 kHz) flexural modes are closer than those of other flexural modes, and the TED energy loss is much higher than the others.

The Q factors in gas environment is increasing and then decreasing as the order of the flexural mode gets higher. This is partially due to the higher intrinsic damping for the 3rd and 4th modes. Besides, the gas damping is found to play an important role, the measured values of

the quality factors Q_{gas} due to gas damping at atmospheric pressure are 543, 1318, and 1890 for the first, second, and third flexural modes, respectively. These results show a general trend that Q_{gas} is increasing as the order of the flexural mode gets higher. However, Q_{gas} slightly reduces to 1645 at the fourth flexural mode. It indicates that Q_{gas} will not unlimited increase as the increasing frequency. The reason for this is waiting for further investigation.

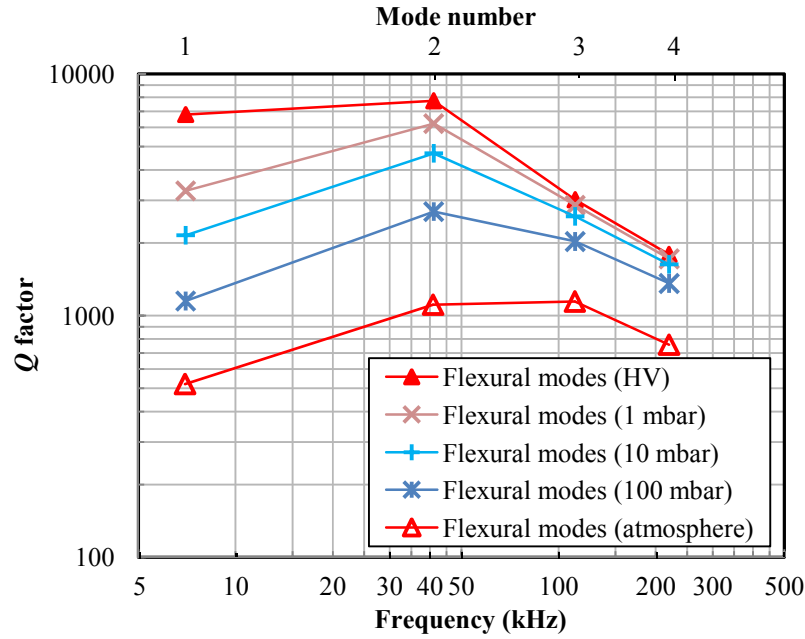


Figure 3.20: The Q factors of the flexural modes at different pressures in N_2 environment.

More cantilevers, numbered as $C1$, $C2-I$, $C3$ and $C6-I$, were tested and characterized. Since the Q factor dependence on surrounding pressure is expected to be similar to that shown in Fig. 3.19, only the results in vacuum and at normal atmosphere N_2 are shown here.

From Fig. 3.21 (a) one can find that, firstly, for the flexural modes, almost constant quality factors are found when the resonance frequency is lower than 50 kHz or higher than 300 kHz, whereas a minimum occurs around 200 kHz, as indicated by the dashed curve in the figure. Secondly, the torsional modes have the highest quality factors in vacuum. Thirdly, the intrinsic quality factors for the lateral modes are around 2000, which limit the quality factors in gaseous environment. In future research, we will focus on decreasing the intrinsic damping for the lateral mode.

The vibration features in atmospheric pressure are shown in Fig. 3.21 (b). For the flexural modes, the quality factor first increases as the mode number and frequency increases, but the growth of quality factor slows down and finally decreases. This is induced by both higher intrinsic and gas damping. While the torsional modes, again, show the highest quality factors at atmospheric pressure.

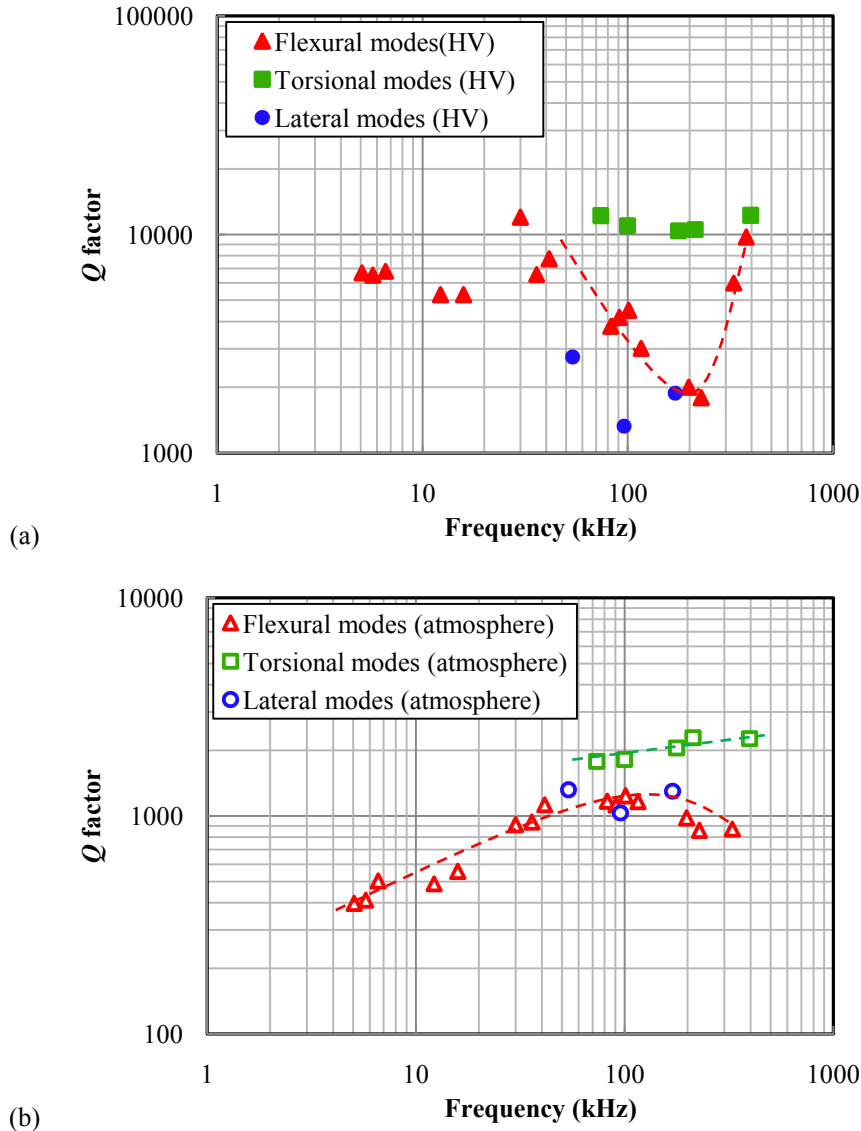


Figure 3.21: The Q factors as a function of resonance frequency of different cantilevers at different modes, (a) in HV and (b) at atmospheric pressure in N_2 environment. The dashed lines are guides to the eye only.

To further evaluate the gas damping effects on the higher flexural vibration modes, the cantilever was tested in different gases. The quality factor associated with the gas damping Q_{gas} in atmospheric pressure is characterized and shown in Fig. 3.22. Resonator vibrating in He shows the highest Q factor for all modes in atmospheric pressure. However, the intrinsic damping is even heavier than gas damping in the third and fourth flexural modes, the Q_{gas} for He is not shown here since they cannot be precisely evaluated. Only the first two modes for Kr, SF_6 and Xe and first three modes for CO_2 could be detected in atmospheric pressure, because the signal of the fourth mode was too weak. The left three gases, Ne, N_2 , and Ar, are successfully characterized in atmospheric pressure up to the fourth flexural mode. Like N_2 , the Q_{gas} of Ar finally decreases for the fourth mode. It can be seen that, for the first two modes, the Q_{gas} inverse linearly scales to $\sqrt{\rho\mu}$ as described before (c.f. Fig. 3.15), while for the

fourth mode, the Q_{gas} shows a larger dependence on the density ρ of the gas.

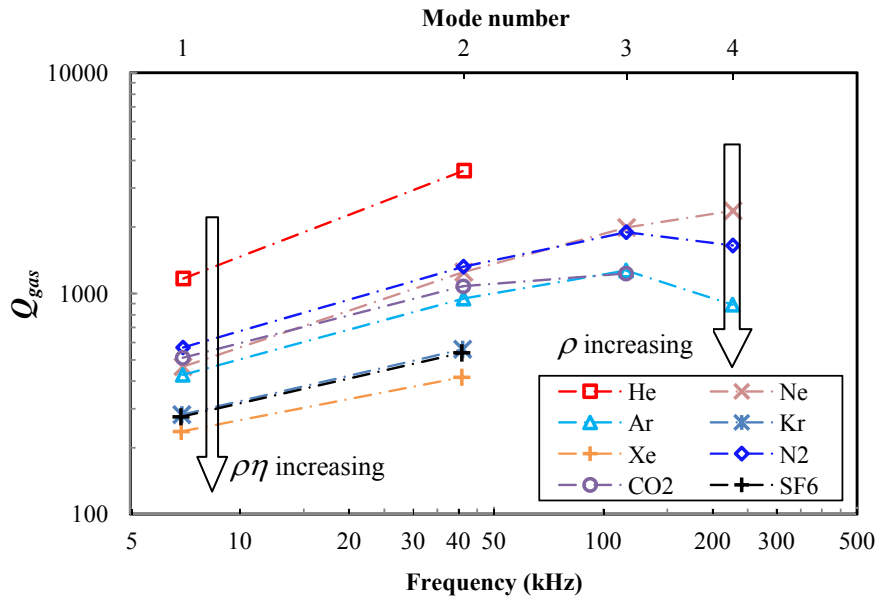


Figure 3.22: The Q factors of the cantilever of different flexural modes in different gases at atmospheric pressure.

When the resonator is vibrating in the first mode (or at low frequency), the gas which the resonator immersed is assumed to be incompressible, thus viscous damping is the dominant energy loss. However, as the mode number increases, the incompressible gas assumption is not valid. Compression of the gas leads to additional acoustic damping and reduces Q_{gas} [135, 136]. So compressible fluid model should be considered when planning experiments which involving the use of higher resonant modes in normal atmosphere.

3.3 Dynamic response of micro resonators vibrating close to a surface

This Section focuses on microbeams vibrating close to a surface, i.e. resonators with a well defined air gap. In many practical applications, resonators are vibrating near a planar surface or sample with a certain gap between the resonator and the wall [137-143]. It is well known that the presence of a wall can strongly affect the hydrodynamic loading on a body immersed in a viscous fluid. For the case when the gap is much narrower than the lateral dimensions of the resonator plate, the theory of squeeze film damping applies and the fluid can be modeled using hydrodynamic lubrication theory. Many publications [66-71] can be found in this field, including the work in our group [72, 73]. Moreover, an effective viscosity η_{eff} is used instead of the gas dynamic viscosity η , to account for the non-continuum fluid behavior in the gap between resonator and surface. This concept is reasonable when the surrounding pressure range is in the viscous regime, which means the pressure is not very low so that the gas can still be considered as a continuum, i.e. when the Knudsen number Kn (here defined as the

ratio of the mean free path of the gas molecules to the gap height), is smaller than 0.1. Burgdoufer [144] obtained a simple form for the effective viscosity coefficient

$$\eta_{eff} = \frac{\eta}{1 + 6Kn}. \quad (3.6)$$

The traditional squeeze film model is sufficient to deal with resonators vibrating very close to a surface or when the plate dimensions are much larger than the film thickness. However, in practical devices the squeeze film assumption does not always hold. In this Section, we experimentally explore the mechanisms by which the closeness to the surface affects the resonator resonance behavior. The experiments are carried out on the *B2* bridge resonator. We will present the results of the first mode of vibration in different gases under pressures varying from HV to normal atmosphere, as well as the results for higher modes of vibration.

3.3.1 Dependence of micro resonator responses on gap width

To understand how fluidic dissipation is modified when the resonator is brought close to a surface, we first measured the fundamental mode of the bridge resonator placed near a surface with the following gap widths h_0 : 20, 50, 100, 150, 200, 250 and 300 μm . The case without gap was also measured for comparison (“without gap” here or “no gap” in the figure means there is no cover on top of the resonator beam. Due to the package configuration, the next neighboring surface under the resonator beam is approximately 2.5 mm away, which is much bigger compared to the beam width, so the influence of this surface is assumed to be negligible). We begin by presenting results of the resonance responses of the resonator immersed in atmospheric N_2 , which is shown in Fig. 3.23.

It is obvious that the resonator beam/surface separation has a strong effect on the resonance behavior. The general trend for the resonance peaks is to broaden and shift to lower peak frequencies as the resonator beam/surface separation decreases. As the bridge is brought closer, this squeeze film damping continues to increase. The measurement results fit with the expectation that the fluid loading force increases significantly upon approach toward a surface. We observe that the resonance frequency shift is relatively insensitive to the presence of a surface when the separation h_0 is greater than 150 μm , which corresponds to a gap to plate-width ratio of more than 0.5. However, for $h_0 = 150 \mu\text{m}$, the Q factor is approximately 20% less than vibration without gap, and for $h_0 = 250 \mu\text{m}$, the Q factors differs by only less than 2%.

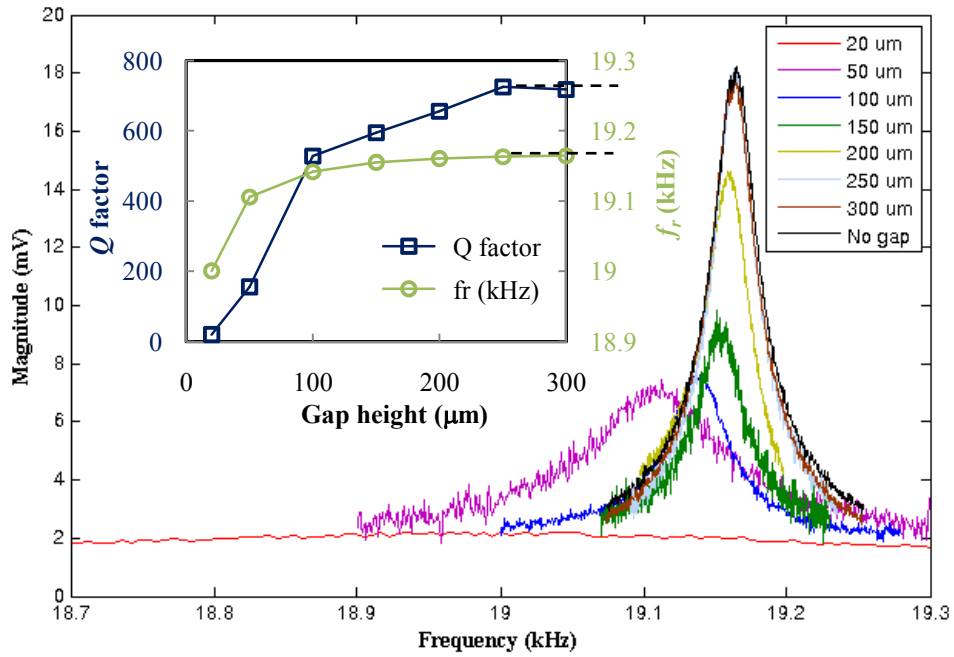


Figure 3.23: Amplitude spectra of bridge resonator in fundamental mode in N₂ at atmospheric pressure. The curves for 250 and 300 μm and no gap are overlapped in this figure. Insert shows the quality factor and resonance frequency, the dashed lines represent the limit as without gap.

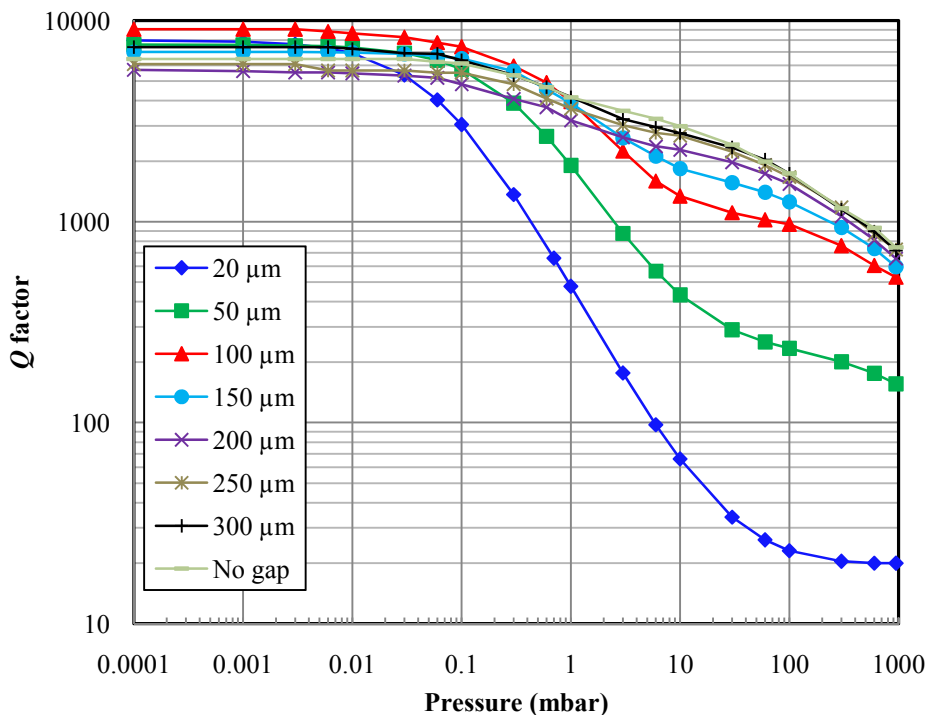


Figure 3.24: Variation of Q factors with ambient pressure for N₂ with different gap heights.

To quantify the pressure effect on the dissipation in the fluid as the resonator is vibrating near a surface, it was further measured under reduced pressures. Fig. 3.24 shows the quality factors with different gap heights for different pressures in N₂ atmosphere. From these results it is

clear that the dissipated energy increases dramatically as h_0 decreases, particularly at low h_0 . These results demonstrate that the proximity of a solid surface leads to a vast increase in viscous dissipative effects in the fluid, as expected from lubrication theory. Furthermore, we observe that for $h_0 > 200 \mu\text{m}$, the quality factor tends to be very similar to that of a resonator immersed in an infinite fluid. For instance, for $h_0 = 250 \mu\text{m}$ at 1000 mbar pressure, the quality factor differs from its value for $h_0 \rightarrow \infty$ by approximately 2%. However, at lower pressure, e.g. 10 mbar, the quality factors differs by more than 10%. In other words, at reduced pressure the presence of a wall can affect the behavior of the dissipative loading, even for large gap heights.

3.3.2 Dependence of micro resonator response on ambient gas

The cases with 20 and 50 μm gap were tested with different gases, and Figs. 3.25 and 3.26 illustrate the results, plotted on a logarithmic pressure scale.

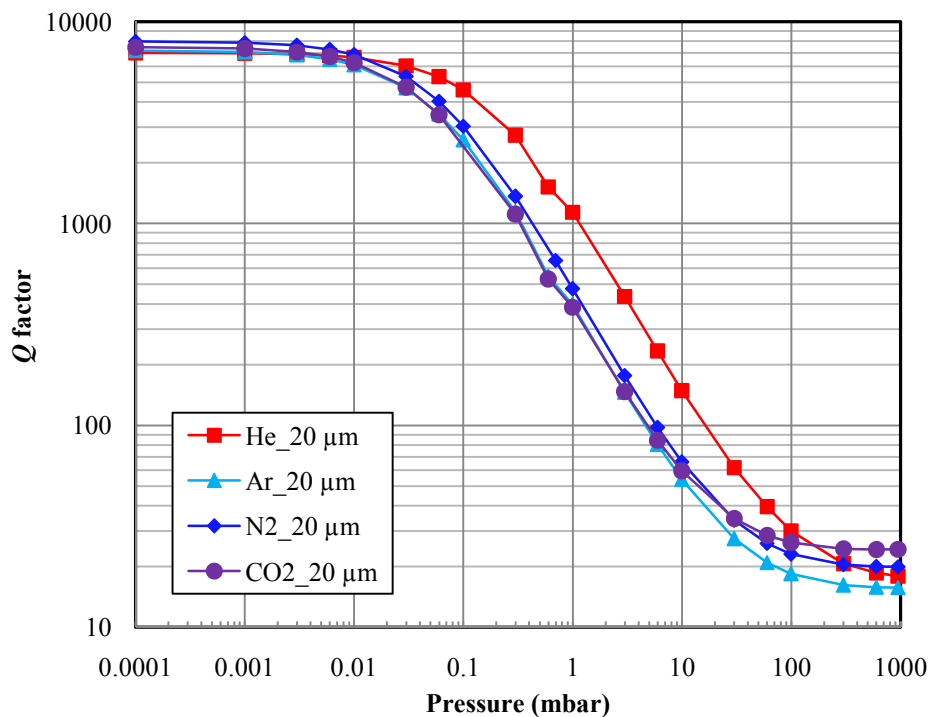


Figure 3.25: Variation of Q factors with ambient pressure for different gases with a 20 μm gap.

From traditional squeeze film theory, the energy loss is proportional to the effective viscosity of the surrounding gas. The assumption is that the gap height should be much smaller than the beam width. To examine the case that does not fit this “narrow gap” assumption, it is necessary to scale all pressure data in terms of effective viscosities. After replotting the quality factors as a function of effective viscosity η_{eff} , linear relationships appeared (c.f. to Fig. 3.27), especially for the 20 μm gap size. For the 50 μm gap a nearly linear relationship

can be observed at lower effective viscosities (equivalent to lower pressure), whereas for higher η_{eff} the Q factors of different gases start to differ from each other, calling for improvement of the traditional theory.

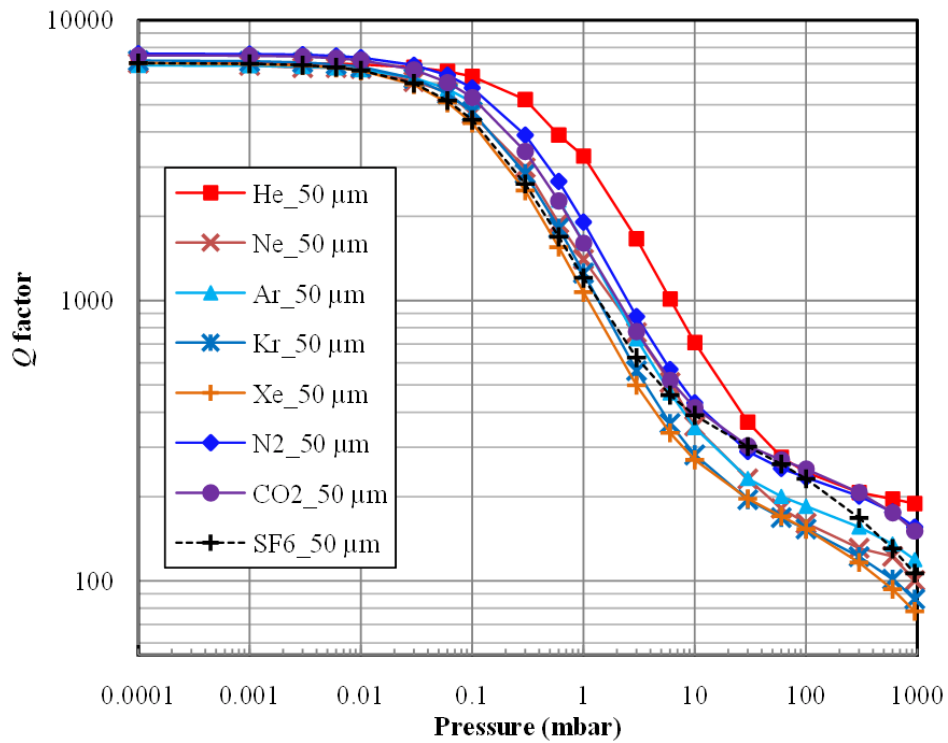


Figure 3.26: Variation of Q factors with ambient pressure for different gases with a 50 μm gap.

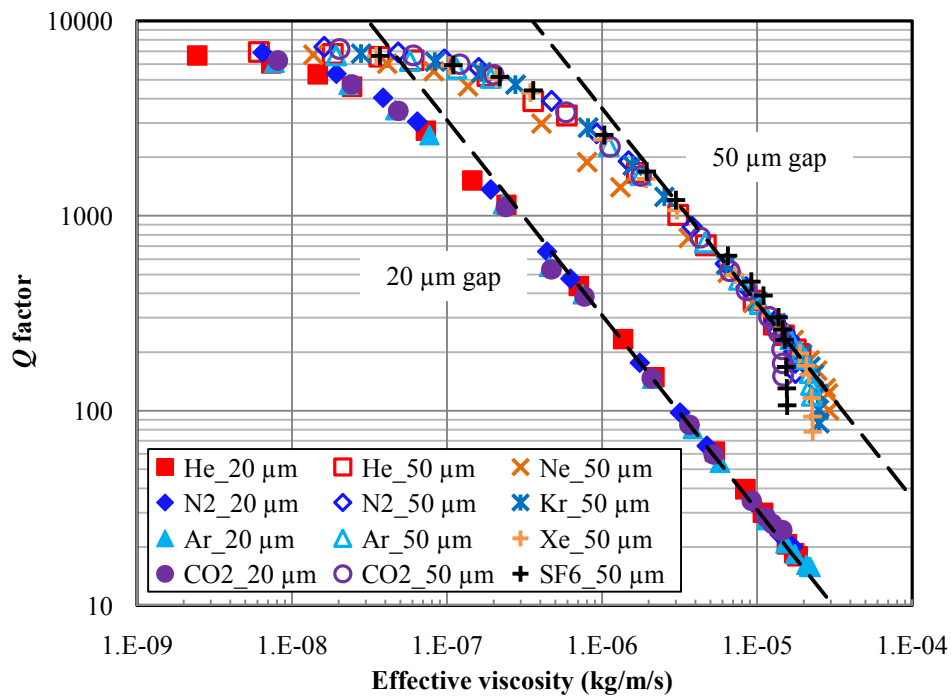


Figure 3.27: Replot of the Q factors shown in Figs. 3.25 and 3.26 as a function of effective viscosity.

3.3.3 Effect of higher vibrating modes

Moreover, the squeeze film effect is expected to be mode shape dependent. To quantify this effect, the Q factors for the higher modes were measured and plotted in Fig. 3.28. The second mode cannot be detected, only the first and third flexural modes are shown here. The quality factors generally increase with increasing gap height and resonant mode. Although the intrinsic quality factor in the 3rd mode (2000) is lower than the 1st mode (8000), the quality factors at atmospheric pressure increased from 20 to 146 at 20 μm gap and from 156 to 477 at 50 μm gap.

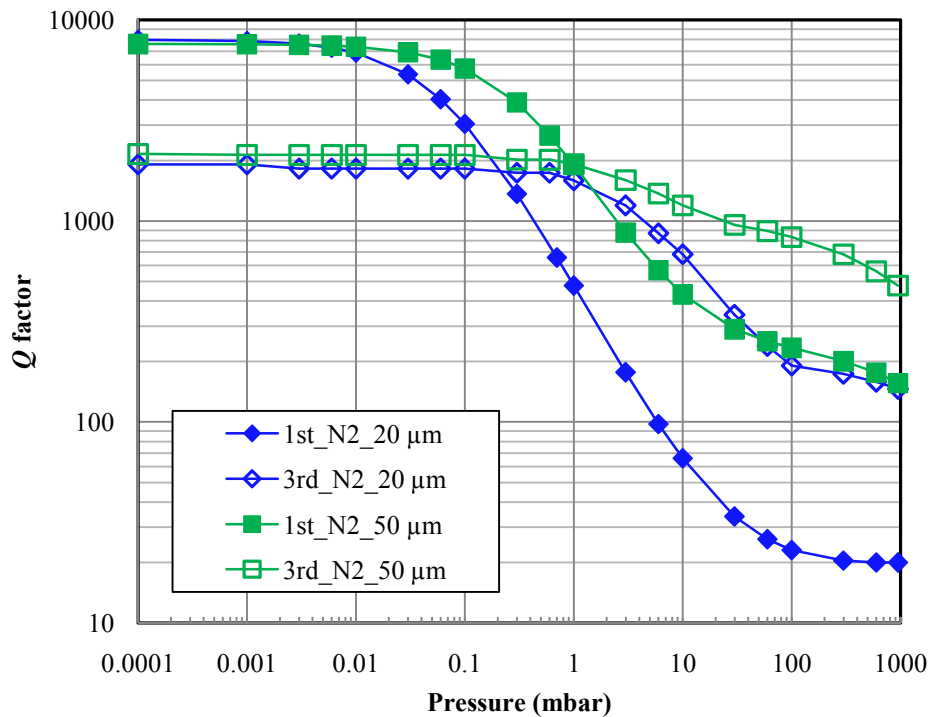


Figure 3.28: Variation of Q factors over pressure for the 1st and 3rd flexural modes and for two different gap heights in N_2 atmosphere.

3.4 Conclusion

Detailed experimental measurements of the resonance responses of different microbeam resonators immersed in eight different gases under pressures ranging from 10^{-4} to 1000 mbar have been presented. The measurements are used to assess the validity and applicability of different energy-loss models for resonators, which will be presented in the next Chapters. The main observations and findings of this Chapter are the following:

For resonators vibrating in unbounded gases:

- (1) The resonance frequency shift of microbeams immersed in gases is mainly affected by the gas density (equivalent to molecular mass). Although there are big dynamic viscosity

variations of the eight different gases, no direct dependence of the resonance frequency shift on the dynamic viscosity is observed.

- (2) In contrast, the Q factor is dominated by viscous damping in the higher pressure range, and is influenced by both gas density and viscosity. For resonators vibrating in gases in the viscous regime, especially at or near atmospheric pressure, a linear dependence on $\sqrt{\rho\mu}$ is observed.
- (3) The performance of microcantilevers in higher order resonance modes is systematically investigated. The torsional modes exhibit better quality factors than those of the flexural and lateral ones over the whole pressure range. The cantilever vibrating in lateral mode experiences the lowest gas damping, but the highest intrinsic damping.
- (4) For the flexural modes, the quality factors in vacuum are found to be almost constant when the resonance frequency is lower than 50 kHz or higher than 300 kHz, whereas a minimum occurs around 200 kHz, this is mainly because of TED damping. While at atmosphere, the quality factor first increases as the mode number and frequency increases, but the growth of quality factor slows down and finally decreases. This is induced by both higher intrinsic and gas damping. Further measurements with different gases show that the compressibility of gases leads to additional damping when the resonator is vibrating in higher mode, whereas in most cases, the gases are assumed incompressible.

For resonators vibrating in bounded gases:

In traditional theories, viscous damping models assume that the resonator is vibrating in unbounded fluid, while squeeze film damping models are based on the assumption that resonators vibrating very close to a surface or the plate dimensions are much larger than the film thickness. In practical devices these assumptions do not always hold. Experiments with a big range of beam/surface separation are performed, and can be used to verify the improved theoretical models which will be presented in next Chapter.

4. Analysis of hydrodynamic loading on vibrating micro resonators

In this Chapter, the research interest is focused on beam-shaped resonators operating in gas media. Firstly, the full set of Navier-Stokes equation is semi-analytically solved using the Boundary Element Method (BEM) [39-43]. The solution of the model can be interpreted by a “three wave theory” with coupled viscous, thermal and acoustic waves. The viscous and thermal wavelengths are in the same order of magnitude but much shorter than the acoustic wavelength. For low frequency vibration, the energy is mainly dissipated by the viscous and thermal waves. However, as the resonance frequency increases, the acoustic wavelength in the fluid reduces and ultimately becomes comparable to and even smaller than the structural wavelength. In such cases, acoustic radiation can be the dominant energy loss into the surrounding fluid.

In this work, the FEM package COMSOL Multiphysics [46] has been used to solve and simulate the full model equations. The comparison of the measured quality factors from a plate resonator and COMSOL simulation confirms the accuracy of the full model and COMSOL prediction. Later, COMSOL simulations are also used to verify with experiment results and simplified analytical models.

Secondly, for slender structures at moderate reduced pressures viscous drag is typically the dominant loss mechanism. Viscous damping models require solution of the Navier-Stokes equations for unsteady, incompressible flow. Some simple geometry like a sphere [47-50, 56] or a cylinder [52, 55] is taken as an approximation of the actual geometry. Incompressible flow is expected for the first few flexural or torsional harmonic modes where the dominant length scale of the beam is much smaller than the wavelength of sound in the fluid. However, as the resonant mode number increases, the acoustic wavelength reduces and the energy loss is diluted through mixing of viscous and acoustic effects. Discussion on the influence of the fluid’s compressibility on the resistance of the beam is carried out.

Thirdly, in many MEMS applications, micro resonators are either fabricated or intentionally moved close to a second surface, separated by a well defined gap. The vicinity of the micro resonator to such a surface can affect significantly the quality factors. Traditional squeeze film models are sufficient to deal with resonators vibrating with a gap size to a nearby surface which is much smaller than the plate dimensions. However, in practical devices this “squeeze film” assumption does not always hold. We will focus on gap sizes that are comparable to the lateral dimensions. An extended squeeze film theory [77, 78] and a semi-analytical solution

[79-81] derived from unsteady Navier-Stokes equations are examined with experiments and COMSOL simulations. Besides, Schwarz and Seidel [82] have proposed a new thermo-mechanical resonance model to account for the gas damping effect in the transition regime. In this work the resonance behavior over a wide pressure range (from HV to atmospheric pressure) is also modeled quantitatively by the superposition of different damping mechanisms in the different flow regimes, including the thermo-mechanical damping in the transition regime.

4.1 Full Navier-Stokes equations and numerical simulation

For a gas continuum, the most extensive type of model clearly must be based on a solution of the full set of Navier-Stokes equations. This means that it takes into account the effect of gas viscosity, thermal conductivity and compressibility. The variables are pressure, density, velocity and temperature that all vary around the vibrating structure. This leads to a very straightforward and widely applicable model.

4.1.1 Theory

The basic equations governing the gas motion due to the resonator vibration are the compressible Navier-Stokes equation, the equation of continuity, the equation of state for an ideal gas and the energy equation. The equations can be written as:

$$\partial \mathbf{u} / \partial t + (\mathbf{u} \cdot \nabla) \mathbf{u} = -\frac{1}{\rho} \nabla p + \frac{4}{3} \frac{\eta}{\rho} \nabla (\nabla \cdot \mathbf{u}) - \frac{\eta}{\rho} \nabla \times (\nabla \times \mathbf{u}), \quad (4.1)$$

$$\rho (\nabla \cdot \mathbf{u}) + \partial \rho / \partial t = 0, \quad (4.2)$$

$$p = (C_p - C_v) \rho T, \quad (4.3)$$

$$\rho C_p \partial T / \partial t = \kappa \Delta T + \partial p / \partial t, \quad (4.4)$$

where \mathbf{u} , C_v and t denote respectively the velocity vector, heat capacity at constant volume and time. The operators ∇ and Δ are the gradient and Laplace operator.

This set of equations has been implemented in the commercial package COMSOL Multiphysics [46]. In order to understand the equations more deeply, an alternative solution of the full model called Boundary Element Method (BEM) [39-43] is discussed here. The velocity is written as the sum of a viscous velocity \mathbf{u}_v , due to viscous effects, and a laminar velocity \mathbf{u}_l :

$$\mathbf{u} = \mathbf{u}_v + \mathbf{u}_l, \quad (4.5)$$

which satisfy the conditions that the divergence of the viscous velocity is zero: $\nabla \cdot \mathbf{u}_v = 0$, and the rotation of the laminar velocity is zero: $\nabla \times \mathbf{u}_l = 0$.

The pressure is also split up into two components:

$$p = p_a + p_h, \quad (4.6)$$

where p_a is the acoustic pressure and p_h is the thermal pressure. Splitting the acoustic variables facilitates rewriting the governing equations into scalar wave equations for the acoustic and thermal pressures and a vector wave equation for the viscous velocity:

$$(\Delta + k_a^2) p_a = 0, \quad (4.7)$$

$$(\Delta + k_h^2) p_h = 0, \quad (4.8)$$

$$(\Delta + k_v^2) \mathbf{u}_v = 0. \quad (4.9)$$

The temperature fluctuation ΔT is the sum of acoustic and thermal temperature variations related to the acoustic and thermal pressures by:

$$\Delta T = \alpha_a p_a + \alpha_h p_h, \quad (4.10)$$

and the laminar velocity \mathbf{u}_l is written as:

$$\mathbf{u}_l = \phi_a \nabla p_a + \phi_h \nabla p_h. \quad (4.11)$$

The exact expressions for the coefficients k_a , k_h , k_v , α_a , α_h , ϕ_a , and ϕ_h can be found in the literature [39-42].

4.1.2 Physical interpretation

The solution of the full set of equations can be physically interpreted as follows: The structural vibration results in acoustic wave propagation in the surrounding fluid. The acoustic domain can be divided into a boundary layer and the bulk region, as shown in Fig. 4.1. In micro scaled geometries where the boundary layer (also refer to Fig. 1.4) occupies a substantial part of the acoustic domain, the acoustic model needs to account for the viscothermal effects to accurately describe the wave propagation.

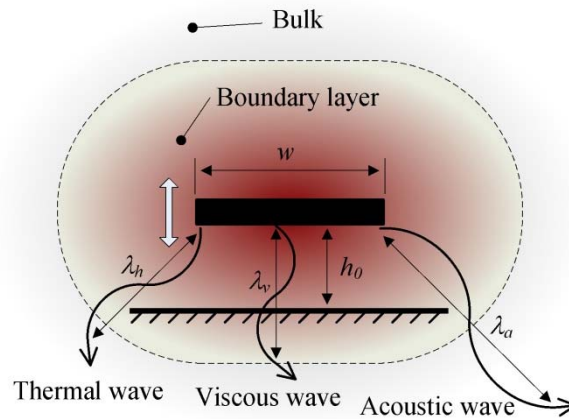


Figure 4.1: Two regions in the acoustic domain: the bulk and the boundary layer, and three waves due to vibration.

Amongst other authors, Mechel [145] describes the viscothermal acoustic equations as a “three wave theory”: interaction of an acoustic wave, a viscous wave and a thermal wave. The expressions for the acoustic k_a , viscous k_v and thermal k_h wave numbers are derived from the solution of the full model. They are defined as: $k_a = \omega/c_0$, $k_v^2 = -i\omega\rho/\eta$ and $k_h^2 = -i\omega\rho C_p/\kappa$, with i the imaginary unit. The wavelengths λ_v , λ_h of the more heavily damped viscous and thermal waves are related to the boundary layer thickness, while the slightly damped acoustic wave propagates with wavelength λ_a mainly in the bulk regime. The formed viscous and thermal wavelengths have comparable length scales with the boundary layer thickness, but they are much smaller than the acoustic wavelength. Fig. 4.2 compares these frequency dependent length scales in air at frequencies from 1 kHz to 1 MHz.

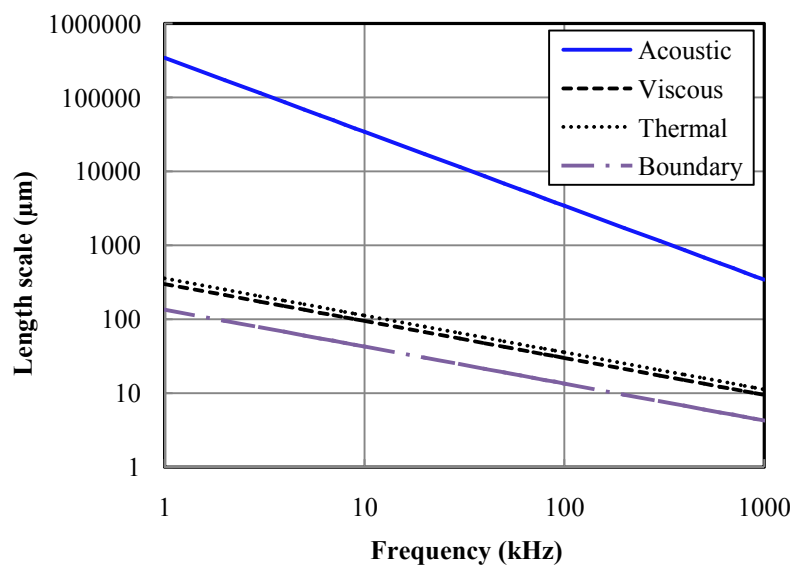


Figure 4.2: Characteristic length scales for vibrations in air: acoustic wavelength (solid), viscous wavelength (dashed), thermal wavelength (dotted) and boundary layer thickness (dash-dotted).

For microscale resonators vibrating in the fundamental mode and in the next few harmonics, the dominant length scale of the beam (e.g. width of the cantilever) is much smaller than the acoustic wavelength in the fluid. In this case the acoustic wave develops only very weakly so that the bulk region can be ignored and the fluid is expected to be practically incompressible and the energy loss is mainly due to the viscothermal dissipative effects. Consequently, the fluid motion can be described quite accurately by using incompressible Navier-Stokes equations. However, as the mode number or resonance frequency increase, the acoustic wavelength in the fluid reduces and ultimately becomes comparable to or even smaller than the dominant length scale of the beam. In this case, the bulk regime can become significant and the acoustic wave starts to radiate vibration energy. Therefore, compressibility can become critically important for operation at higher order modes, which would otherwise be greatly underestimated. In the extreme case, the fluid motion and the related energy losses can be modeled using a normal acoustic wave equation and the viscothermal effect can be neglected.

4.1.3 Comparison between experimental and simulated results

Estimating the gas damping characteristic of micro devices is one of the most important steps in the design process. Most existing models are accurate only for resonators with slim beams or narrow air gaps. For relatively large scaled devices like microphones, or resonators with moderate air gap, neither of the assumptions is fulfilled. One of the example resonators (numbered as *PI*) is shown in Fig. 4.3, the insert shows the chip mounted on a PCB board. The resonator was tested under controlled pressure from HV to normal atmosphere.

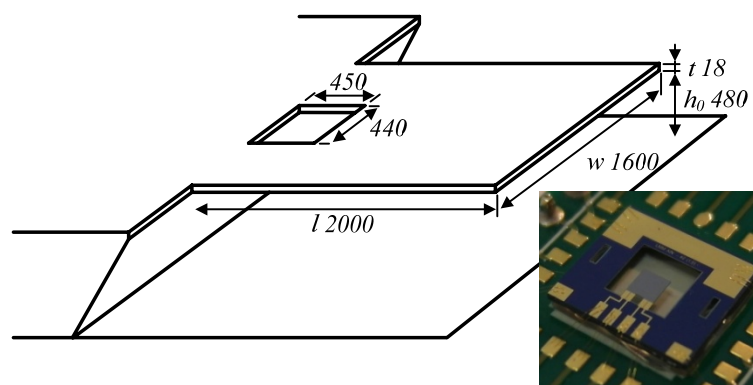


Figure 4.3: The geometry of the *PI* resonator (in μm). The insert shows the photo of the resonator mounted on a PCB board with attached bonding wires.

The case of a resonator vibrating in gaseous environment is a typical fluid structure interaction (FSI) problem, which can be simulated by using an FEM software package. We used COMSOL in our simulations. The geometry of the model, being symmetrical with

shown for comparison. Comparing the pressure distributions in Fig. 4.5, it is clear that significant pressure changes can occur in the gap between resonator and substrate. As the microcantilever is brought closer, this squeeze film damping is expected to become more and more significant.

The simulation results for both cases and the measurement data are shown in Fig. 4.6. The simulated Q factor for the resonator vibrating in unbounded N_2 atmosphere is higher than the measured value, since this simulation neglects the squeeze film effect. However, when the substrate is included, good agreement between simulation and measurement results is observed for the pressure range above 10 mbar. The real resonator was covered by a thin piezo-electrode stack to excite and detect the resonance. To simplify the computation, in the simulation (as well as analytical solutions in following Sections), the resonator structure is assumed as a pure silicon block, the piezo-electrode stack is eliminated by simply increasing the silicon membrane thickness, to get a similar spring constant. The discretization error due to model mesh was kept at a minimum by a mesh convergence study. The fluid mesh independence is checked for convergence by increasing the number of elements in the fluid domain and thereby achieving finer mesh density. To ensure convergence, we do several simulations until the numerical simulation results are within 5% of the converged value.

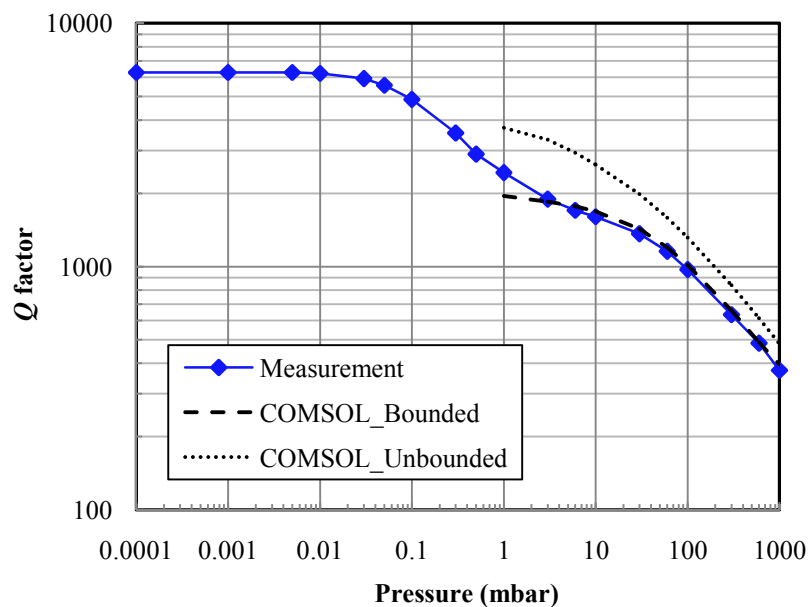


Figure 4.6: Measured and simulated Q factor of the resonator as a function of ambient pressure.

4.2 Hydrodynamics of micro resonators vibrating in unbounded fluids

The full Navier-Stokes model is widely applicable, practically any geometry can be described with it. However, due to the mathematical complexity, such models are computationally extensive, relying on sophisticated numerical techniques and software packages. They are often non-intuitive and do not easily lead to a physical understand of the results, which limits their accessibility and utility in practical applications. In many cases the resonator structures are beam-shaped, and the problem can be further simplified. This Section will focus on the description of beam-shaped resonators vibrating in unbounded fluids. In addition to developing such a model, we systematically investigate the effect of increasing mode numbers on the general characteristics of the resonance response, which is relevant to the design and operation of micro resonator applications.

4.2.1 Analysis for micro resonators in the flexural mode

The dissipation of vibration energy of a micro resonator can occur due to acoustic radiation and viscous loss in the surrounding fluid, as well as due to internal structural damping and support loss. However, for most micro devices vibrating at relatively low frequency (e.g. lower than 100 kHz), viscous drag is typically the dominant loss mechanism at higher pressures. Viscous damping models require solution of the Navier-Stokes equation and continuity equation for unsteady, incompressible flow [51]:

$$\frac{\partial \mathbf{u}}{\partial t} + (\mathbf{u} \cdot \nabla) \mathbf{u} = -\frac{1}{\rho} \nabla p + \frac{\eta}{\rho} \Delta \mathbf{u}, \quad (4.12)$$

$$\nabla \cdot \mathbf{u} = 0. \quad (4.13)$$

The equations cannot be solved in a closed form for the beam-shaped cantilever, but some simple geometry could be taken as an approximation of the actual geometry. One popular method, first developed by Blom *et al.* [56], then extended by Kokubun *et al.* [47, 48] and by Hosaka *et al.* [49, 50], is to represent the beam as a string of spheres, for which the drag force can be analytically determined (see Fig. 4.7 (a) sphere string model). Another approach is to apply the vibrating solution of a resonating cylinder instead of a string of spheres, which can alleviate the issue of incomplete coverage of spheres over the beam structure. This more accurate model is proposed by Kirstein *et al.* [52], and Sader *et al.* [53] based on the earlier work of Tuck [54] (Fig. 4.7 (b) cylinder model).

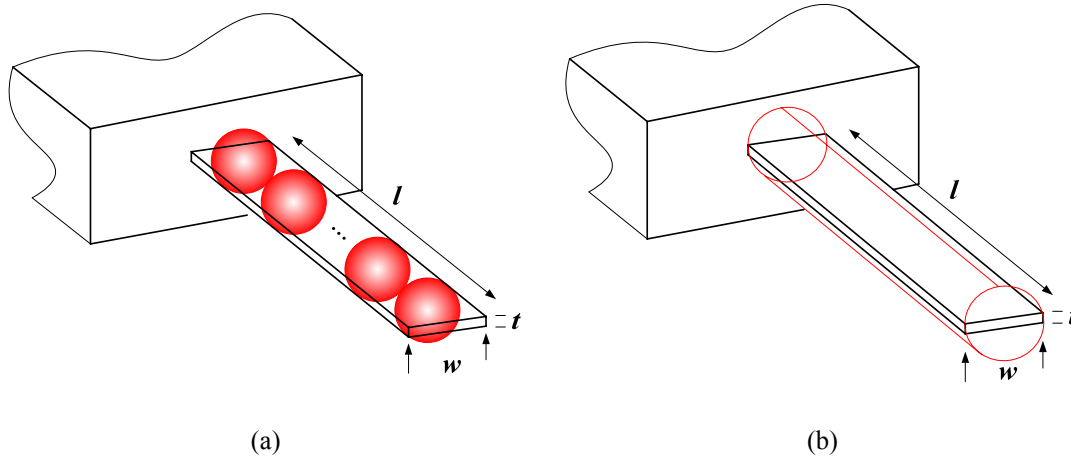


Figure 4.7: Simplified model for the beam resonator: (a) sphere string model and (b) cylinder model.

In most of the models derived based on these approaches, a general assumption is to have a flow with a small Reynolds number, Re , which is defined as (compare with Section 1.2.4 in the Introduction Chapter):

$$Re = \frac{\rho\omega w^2}{4\eta}. \quad (4.14)$$

The physical meaning of the Reynolds number is the ratio of inertial forces to viscous forces. Thus it quantifies the relative importance of these two types of forces for given flow conditions. The requirement for a small Reynolds number in the models implies that they are more accurate for lower resonance frequencies or for smaller resonators. Correspondingly, viscous effects in the fluid become increasingly important.

Sphere string model

Oscillatory motion of a sphere in an infinite viscous fluid is treated by Landau and Lifshitz [51]. The fluid drag force \mathbf{F}_d for an oscillatory motion sphere with radius R can be calculated straightforwardly from eqs. (4.12 and 4.13), and the fluid drag force is expressed as:

$$\mathbf{F}_d = 6\pi\eta R \left(1 + \frac{R}{\delta}\right) \mathbf{u} + 3\pi R^2 \sqrt{\frac{2\eta\rho}{\omega}} \left(1 + \frac{2R}{9\delta}\right) \frac{d\mathbf{u}}{dt}, \quad (4.15)$$

where δ is the boundary layer thickness, defined as $\delta = \sqrt{2\eta/(\rho\omega)}$ (refer to eq. (1.9)). The boundary layer corresponds to the penetration depth of the shear waves emanating from the oscillating particle. In case δ is much larger than the radius of the sphere, one is in the low-frequency limit, where the flow is quasi-stationary. Note that, for $\omega = 0$ this becomes Stokes' formula $\mathbf{F}_d = 6\pi\eta R\mathbf{u}$.

The gas load effect can be characterized from the drag force \mathbf{F}_d , with a damping coefficient:

$$c_{spher} = 6\pi\eta R \left(1 + \frac{R}{\delta}\right), \quad (4.16)$$

derived from the real part of \mathbf{F}_d , and the spring constant:

$$k_{spher} = -3\pi R^2 \omega \sqrt{2\eta\rho\omega} \left(1 + \frac{2R}{9\delta}\right), \quad (4.17)$$

from the imaginary part of \mathbf{F}_d .

For a slender resonator, the vibrating beam can be modeled as a string of spheres, where the diameter of each sphere is approximated to the width of the beam, whereas if the resonator is smaller (e.g. in sub-micrometer range) or under reduced pressure, R is a fitting parameter [128]. If these spheres vibrate independently of each other, the resulting drag force is the sum of the drag forces of the individual spheres. Therefore the result from eq. (4.15) is used as an approximation of the fluid drag force for the beam. According to this model, the quality factor associated with the gas damping $Q_{flex,spher}$ is calculated as:

$$Q_{flex,spher} = \frac{\rho_b t w \omega}{3\pi\eta + \frac{3}{4}\pi w \sqrt{2\rho\eta\omega}}, \quad (4.18)$$

here ρ_b is the density of the beam material.

Cylinder model

Another analytical solution of the Navier-Stokes equation for the oscillation of a cylinder in a viscous medium is well known. Sader *et al.* [53] approximated the damping of a resonating cantilever with that of a long cylinder. In Sader's model, the assumptions are that the length of the beam l greatly exceeds the width w , and also the width greatly exceeds the beam thickness t . The fluid drag force has the following form:

$$\mathbf{F}_d = \frac{\pi}{4} \rho \omega^2 w^2 l \Gamma_{flex}(\omega) \hat{W}(x|\omega), \quad (4.19)$$

where \hat{W} is the Fourier transformation of the cantilever deformation, $\Gamma_{flex}(\omega)$, the so called "hydrodynamic function", is a complex term, and is given by

$$\Gamma_{flex} = 1 + \frac{4iK_1(-i\sqrt{iRe})}{\sqrt{iRe}K_0(-i\sqrt{iRe})}, \quad (4.20)$$

where K_0 and K_1 are modified Bessel functions of the third kind. The real part $\Gamma_{flex,real}$

represents the inertial forces of the fluid, or added mass components; whereas the imaginary part $\Gamma_{flex,imag}$ is proportional to the viscous forces of the fluid, or damping components. Maali *et al.* [146] gave an approximation of the hydrodynamic function for cantilevers with rectangular cross-section, using curve fitting:

$$\Gamma_{flex,real} = a_1 + a_2 \frac{\delta}{w} = a_1 + \frac{a_2}{\sqrt{2Re}}, \quad (4.21)$$

$$\Gamma_{flex,imag} = b_1 \frac{\delta}{w} + b_2 \left(\frac{\delta}{w} \right)^2 = \frac{b_1}{\sqrt{2Re}} + \frac{b_2}{2Re}. \quad (4.22)$$

The parameters for an infinitely thin rectangular beam are $a_1 = 1.0553$, $a_2 = 3.7997$, $b_1 = 3.8018$, $b_2 = 2.7364$.

The expression of the resulting damping coefficient is

$$c_{flex,cyli} = \frac{\pi}{4} \rho w^2 l \omega \Gamma_{flex,imag}, \quad (4.23)$$

and the quality factor can be rewritten as:

$$Q_{flex,cyli} = \frac{\rho_b t w \omega}{\frac{1}{2} b_2 \pi \eta + \frac{1}{4} b_1 \pi w \sqrt{2 \rho \eta \omega}}. \quad (4.24)$$

When we look at the inverse quality factor, we can see from eqs. (4.18 and 4.24) that it can be separated into two components, with a first part being independent of pressure p (equivalent to ρ) and a second part showing a $1/\sqrt{p}$ dependence for Q . This means that when the first part is much bigger than the second, or for small Reynolds numbers ($Re < 1$, equivalent to low pressure, but not molecular regime), the Q factor is only weakly depending on p . When pressure rises, the $1/\sqrt{p}$ dependence dominates, then both models lead to a similar trend and can be further simplified as:

$$Q_{vis} \propto t \sqrt{\frac{\omega}{\rho \eta}} \propto \sqrt{\frac{t^3}{l^2} \frac{1}{\rho \eta}}. \quad (4.25)$$

Despite the mathematical elegance of sphere string model and cylinder mode, the much simplified eq. (4.25) shows a general guideline for viscous dissipation dependence. For slender structures, viscous drag is typically the dominant loss mechanisms, with a $1/\sqrt{\rho \eta}$ dependence, which simplifies to $1/\sqrt{p}$ for a single gas with a given viscosity. There is also a dependence on the square root of the resonant frequency, which can be translated into a

dependence on the resonator length l and thickness t according to $t^{3/2}/l$.

By comparing the results obtained from the methods mentioned above, we find that the gas damping characteristic is proportional to $\sqrt{\omega}$. This gives an indication that a higher-order resonant mode is usually superior in Q compared to a lower-order mode. However, as discussed in [53], the theoretical model is valid provided the mode number is not large, and Ref. [146] experimentally demonstrated that the accuracy of eq. (4.24) decreases as the mode number increases. The best accuracy is expected for the fundamental mode. Consequently, in this Section we restrict our attention to the fundamental mode of vibration. In Section 4.2.5 the vibration behavior in higher modes will be discussed.

4.2.2 Comparison between experimental and analytical results for the flexural mode

To validate the accuracy of analytical formulas described in Section 4.2.1, their predicted Q factors for different gases under varying pressures are compared to the measurement results, which have been presented in Section 3.2.1. The comparison is shown in Fig. 4.8. It can be seen that the predictions of the cylinder model show very good agreement with the measurement within the range from 10^1 to 10^3 mbar, since it rigorously accounts for the true geometry of the cantilever without any fitting parameters. The sphere string model does not agree so well. The deviations between the models predictions and measurement become larger for higher Knudsen numbers (e.g. smaller structures or lower pressures).

As deduced from eq. (4.25), when Re is bigger than 1, the fluidic damping coefficient is expected to obey a linear dependence in $\sqrt{\rho\eta}$. This is experimentally demonstrated in Fig. 3.15. Besides, the damping is dependent on the resonator geometry, mainly related to $t^{3/2}/l$, this simple prediction is also verified experimentally, as shown in Fig. 4.9, by comparing Q factor of a series of cantilevers and bridges which are numbered as *C1-C9* and *B1-B3* (refer to Tab. 3.2 for detailed geometries), with different geometries vibrating in atmospheric N_2 environment.

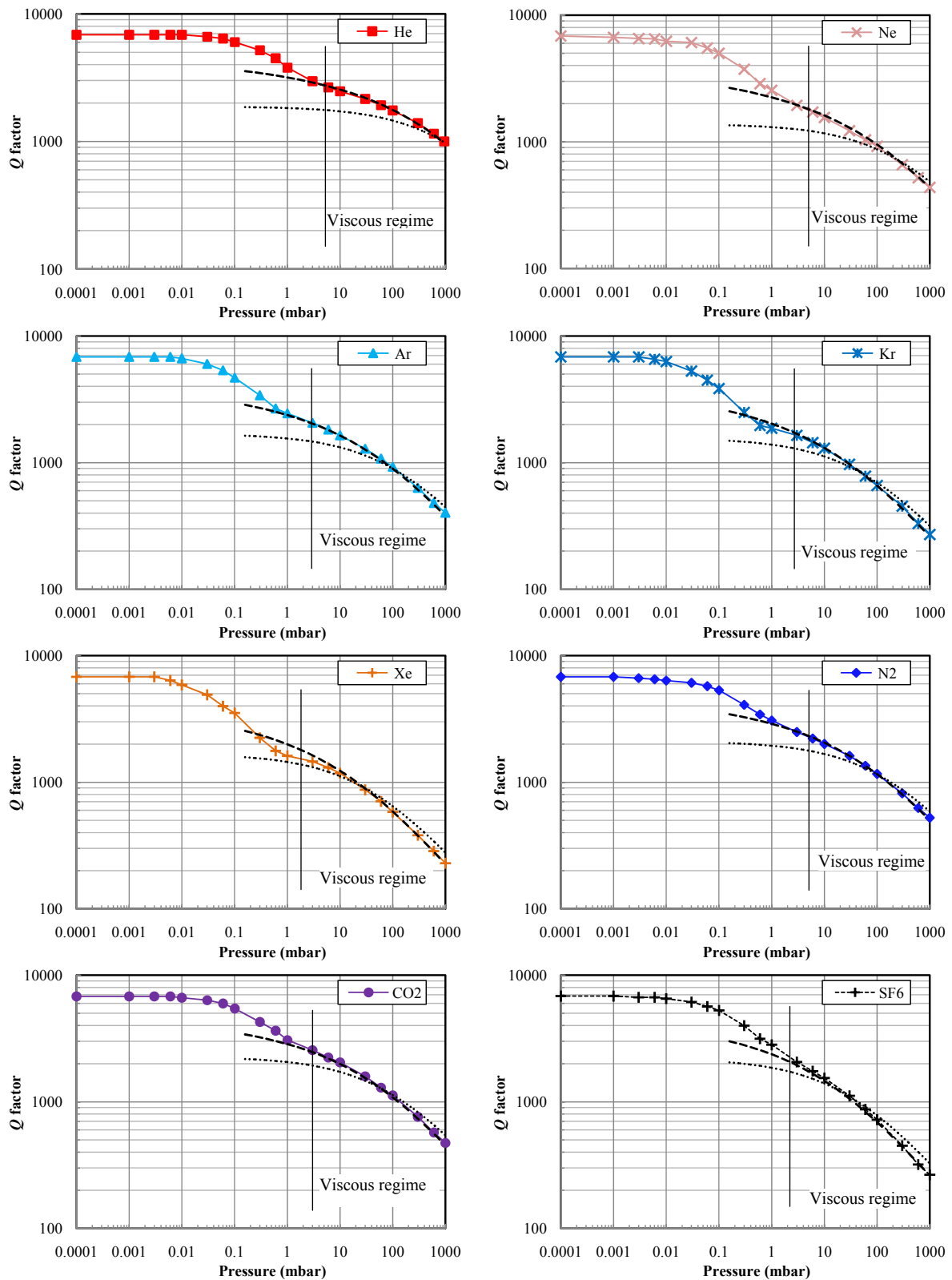


Figure 4.8: Measured and simulated Q factors versus pressure for the flexural mode of the $C6-I$ cantilever. The data points represent the measurement results, the dotted lines (.....) represent the sphere string model predictions (eq. (4.18)), while the dashed lines (---) are the cylinder model predictions (eq. (4.24)). The vertical lines represent the pressure where $Kn = 0.1$, at higher pressure or equally lower Kn , the gas can be considered as in the viscous regime.

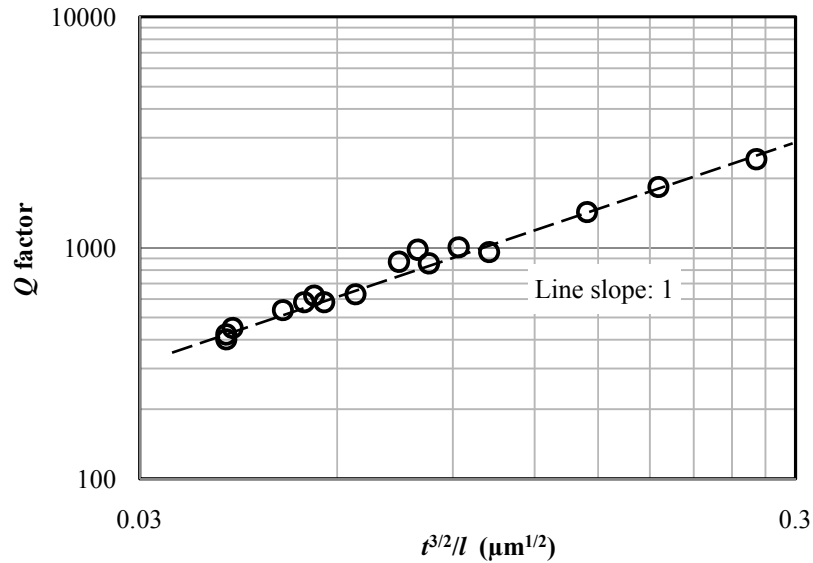


Figure 4.9: Q factor dependence on resonator geometries in N_2 at atmospheric pressure.

4.2.3 Analysis for micro resonators in the torsional mode

Our measurements show that cantilevers show higher quality factors in the torsional mode than in flexural ones (refer to Figs. 3.19 and 3.21). In this example, the cantilever with the higher-order torsional mode exhibits the best performance, i.e. the highest Q factor, the highest mass sensitivity, and the highest sensing resolution. So we now turn our attention to the torsional modes of oscillation, the analysis of which follows along analogous lines to that presented above for the flexural modes. Due to this similarity, we shall only summarize the key results of the analysis here.

Sphere string model

For the torsional vibrating case, it is appropriate to model the beam by a string of flat dishes [58] or two parallel strings of spheres [147, 148]. By calculating the moment of force on the torsional vibrating dishes or spheres, the gas damping force can be derived. Finally the quality factor associated with the gas damping $Q_{tors,sphe}$ is calculated as [147, 148]:

$$Q_{tors,sphe} = \frac{\rho_b t w \omega}{6\pi\eta + \frac{3}{4}\pi w \sqrt{2\rho\eta\omega}}. \quad (4.26)$$

Cylinder model

Similar to Section 4.2.1, an expression for the hydrodynamic function is required for calculating the resonance behavior of the system. An analytical expression for the hydrodynamic function of a microcantilever with circular cross-section in viscous liquids under torsional mode is given by [134]:

$$\Gamma_{tors} = \frac{2i}{Re} + \frac{iK_0(-i\sqrt{iRe})}{\sqrt{iRe}K_1(-i\sqrt{iRe})}, \quad (4.27)$$

In [149] an analytical form of the hydrodynamic function in terms of the Reynolds number Re is obtained by fitting the numerical results as follows:

$$\Gamma_{tors,real} = a_3 + a_4 Re^{-0.43}, \quad (4.28)$$

$$\Gamma_{tors,imag} = \frac{b_3}{\sqrt{Re}} + \frac{b_4}{Re}. \quad (4.29)$$

The parameters for an infinitely thin rectangular beam are $a_3 = 0.06$, $a_4 = 0.288$, $b_3 = 0.338$, $b_4 = 0.75$. The quality factor is calculated as:

$$Q_{tors,cyli} = \frac{\rho_b t w \omega}{6b_4 \pi \eta + 3b_3 \pi w \sqrt{\rho \eta \omega}}. \quad (4.30)$$

Equations in this Section are obtained using incompressible N-S equation for the first torsional mode. However, it is reasonable to extend their utility to a higher-torsional mode of vibration without introducing a serious error in the analysis. In reality, higher order torsional modes are rarely probed in practice.

4.2.4 Comparison between experimental and analytical results for the torsional mode

Fig. 4.10 shows the measured and analytically predicted Q factors of the two torsional mode resonances, as a function of ambient pressure. It can be seen that, on the premise that the surrounding pressure is in the viscous regime, the calculations show fairly good agreement with the measurement results.

Both experiments and calculations clearly indicate that torsional modes of a cantilever exhibit lower environmental damping in comparison with conventional flexural modes. This view point can be visualized by COMSOL simulations in Fig. 4.11, with the illustration of the gas flow around the cross section of the cantilever. When the cantilever moves under the flexural mode, the gas has to flow out of the whole width of the cantilever. However, for the torsional mode, the tuning-fork like anti-phase cantilever movement induces a large part of gas flow between the two sides. So the gas does not need to move around the whole cantilever width. This causes less gas flow volume tension or compression generated by the cantilever and less energy dissipation induced by the gas volume change. All of this contributes to a higher quality factor.

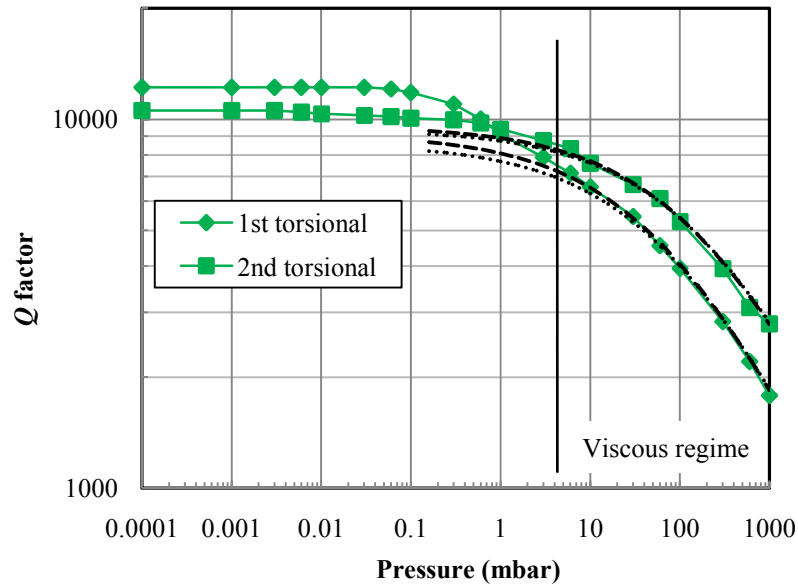


Figure 4.10: Measured and simulated Q factors versus pressure for the torsional modes of the cantilever. The data points represent the measurement results, the dotted lines (.....) represent the sphere string model predictions (eq. (4.26)), while the dashed lines (---) are the cylinder model predictions (eq. (4.30)). The vertical line represents the pressure where $Kn = 0.1$, at higher pressure or equally lower Kn , the gas can be considered as in the viscous regime.

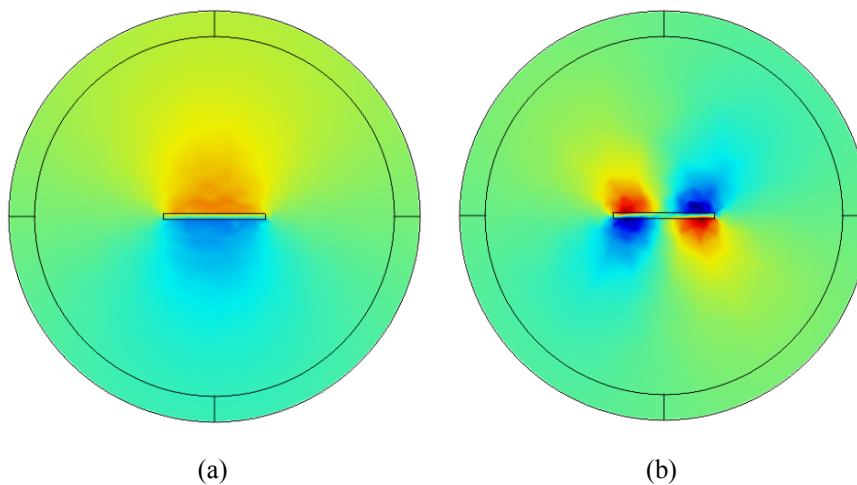


Figure 4.11: Visualized illustration of simulated pressure distribution around the cantilever cross-section in (a) the flexural mode, and (b) the torsional mode.

4.2.5 Discussion on the influence of the fluid compressibility

The models mentioned above assume that the gas in which the cantilever is vibrating, is incompressible. We could demonstrate a generally good agreement with experimental results. It has been also shown that operating the cantilever at higher resonant modes increases the Q factor of the device. However, it is found that the Q factor due to gas damping is finally decreasing when the resonance frequency is sufficiently high. Recent papers from Van Eysden and Sader [61, 62] detailed a model for a cantilever beam oscillating in a compressible fluid.

They predict that, as the mode number increases and passes a “coincidence point”, the Q factor will finally start to decrease. This is further confirmed by Weiss *et al.* [63] who compared the compressible and incompressible fluid simulation results using a numerical method. Jensen and Hegner [64] carried out measurements and found qualitative agreement between experimental results and calculations based on the compressible fluid model of Van Eysden and Sader. Here we note that higher order torsional modes are rarely probed in practice. We therefore restrict our discussion exclusively to the flexural modes.

The resonance frequency $f_{r,n}$ of the n th order flexural mode for a cantilever in vacuum is given by [150]

$$f_{r,n} = \frac{t}{4\pi} \frac{C_n^2}{l^2} \sqrt{\frac{E}{3\rho_b}}, \quad (4.31)$$

where C_n is the n th positive root of

$$1 + \cos C_n \cosh C_n = 0, \quad (4.32)$$

and is well approximated by $C_n \approx (n-1/2)\pi$ for $n \geq 2$.

For a slender elastic beam, the spatial wavelength of the beam for high mode numbers is:

$$\lambda_b = \frac{2\pi l}{C_n} \approx \frac{4l}{2n-1}. \quad (4.33)$$

The wavelength of acoustic oscillations generated by the beam in a fluid is:

$$\lambda_a = \left(\frac{C_1}{C_n} \right)^2 \frac{c_0}{f_1} \approx \frac{1.425}{(2n-1)^2} \frac{c_0}{f_1}. \quad (4.34)$$

Therefore, as the mode number increases, the acoustic wavelength λ_a eventually becomes comparable to the spatial wavelength of the beam λ_b , and compressibility can no longer be ignored. It is possible that energy can be dissipated by the generation of acoustic waves.

In order to resolve this issue, exact solutions for the 3D flow field were derived for the microcantilever in compressible viscous fluids [61, 62]. In this model, the “hydrodynamic function” Γ was obtained by solving a linear system of algebraic equations. Coefficients of the linear system were complex and expressed in terms of the Meijer G function [151]. A large number of integration steps is required to provide sufficient convergence of the solution. Due to the complication of this solution, here we seek another compact method to explain the compressible fluid damping. When acoustic radiation is the dominant loss, it can be modeled

using the acoustic wave equation:

$$\nabla^2 p + \frac{1}{c_0^2} \frac{\partial^2 p}{\partial t^2} = 0. \quad (4.35)$$

By approximating the rectangular cross-section with an elliptical cross-section, Blake [152] has obtained an approximation expression for the acoustic losses. The quality factor associated with acoustic radiation can be further simplified as [135]:

$$Q_{acous} = \frac{t \rho_b \omega}{2 \sigma_r \rho c_0}, \quad (4.36)$$

σ_r is a parameter known as the radiation efficiency, defined as the ratio of the average acoustic power radiated per unit area of the vibrating structure to the acoustic power radiated per unit area of a circular piston vibrating uniformly [153]. It increases from infinitesimal to 1 until the spatial wavelength of the beam λ_b exceeds the acoustic wavelength in the fluid λ_a .

To demonstrate how the resistance of a surrounding fluid and the damping due to the radiation of pressure waves affect the vibration behavior of a cantilever, quality factors of up to the 4th flexural modes of the beam are characterized and compared when vibrating in different gases. As the compressible effect can be observed only at high pressure, the Q factors at atmospheric pressure are selected and illustrated in Fig. 4.12.

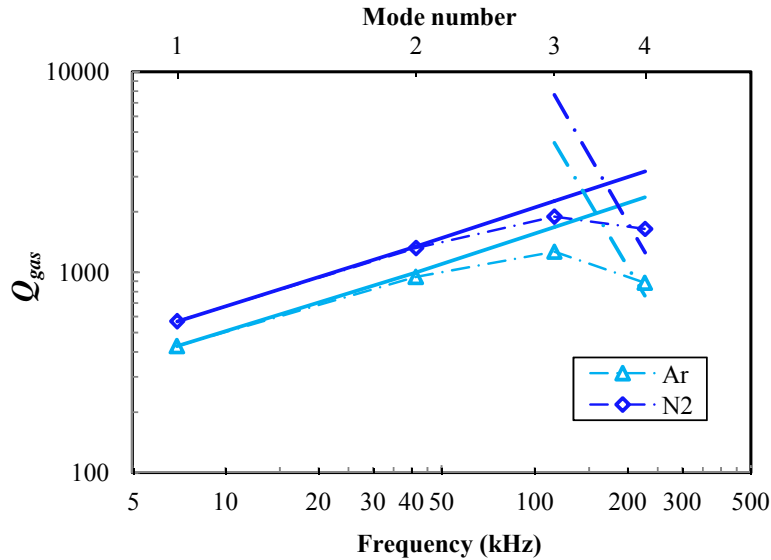


Figure 4.12: Quality factors due to gas damping of the resonance frequency and mode number. The data points are derived from the measurements after subtracting intrinsic damping, the solid lines are calculations based on the incompressible gas assumption (eq. (4.23)), while the dash-dotted lines are the acoustic wave model predictions (eq. (4.36)).

It is clear that the quality factor decreases after reaching the “coincident point”, which agrees

qualitatively with the predictions of the compressible fluid model. In conclusion it was observed that there is at least qualitative agreement with the compressible fluid model for practical microcantilevers. The compressible fluid model should be considered when planning experiments involving the use of higher resonant modes of microcantilevers in normal atmosphere.

4.3 Hydrodynamics of micro resonators vibrating close to a surface

The traditional squeeze film models deal with resonators vibrating very close to a surface or the plate dimensions are much larger than the film thickness (which is often called “narrow gap” assumption). However, in many practical devices, this narrow gap assumption does not always hold. In this Section we will focus on those that deal with moderate gap sizes. Three recently improved theories, namely (a) the extended squeeze film model, (b) the unsteady Navier-Stokes model and (c) a thermo-mechanical resonance model, as well as the COMSOL simulations are considered for describing the behavior of the resonators and they are compared with experiment results.

4.3.1 Mathematical models for micro resonators vibrating close to a surface

Extended squeeze film model

For the application of fluid lubrication, Osborne Reynolds first formulated the theory for a fluid film between two surfaces in relative motion to each other more than a century ago [66]. For normal motion of parallel plates with small displacement, the fluid motion is governed by the compressible Reynolds equation, which can be linearized as [67]:

$$p \left(\frac{\partial^2 p}{\partial x^2} + \frac{\partial^2 p}{\partial y^2} \right) - \frac{12\eta}{h_0^2} \frac{\partial p}{\partial t} = \frac{12\eta p}{h_0^3} \frac{\partial h}{\partial t} \quad (4.37)$$

Generally, the compressibility should be considered in modeling squeezed-film dampers. The importance of the compressibility increases when the oscillation frequency increases. An important measure for the squeezed film effect is the squeeze number:

$$\sigma = \frac{12\eta w^2 \omega}{p h_0^2}. \quad (4.38)$$

The squeeze number specifies the ratio between the spring force due to the gas compressibility, and the force due to the viscous flow. When σ is much smaller than 1, the gas in the film has enough time to “leak” out, thus, the gas is referred to as incompressible. For

the damper topologies in this study, the damper width w and the gap height h_0 are of the same order of magnitude, let us say $w/h_0 < 10$. For air at atmospheric pressures the resonance frequency should be higher than 700 kHz to ensure the squeeze number σ is bigger than 1.

When the squeeze number is very small, the compressible effects can be ignored and eq. (4.37) reduces to

$$\frac{\partial^2 p}{\partial x^2} + \frac{\partial^2 p}{\partial y^2} = \frac{12\eta}{h_0^3} \frac{\partial h}{\partial t}. \quad (4.39)$$

The solution to this Reynolds equation for incompressible gases, eq. (4.39), is usually given in complicated series. There are many forms of solution in the literature. The common conclusion is that the coefficient of the damping force can be written as

$$c_{squ} = \frac{\eta l w^3}{h_0^3} \beta(w/l), \quad (4.40)$$

where $\beta(w/l)$ is the geometrical correction factor. This factor for a square plate is 0.4217, and for a slender beam is 1, which is consistent with our case. The quality factor is then given by

$$Q_{squ} = \frac{\rho_b t \omega}{\eta w^2} h_0^3. \quad (4.41)$$

Griffin *et al.* [68] verified the analytical results by experiments at low frequency. They found that the agreement is very good when the gap distance is smaller than the plate dimensions by more than a factor of 10.

In order to include border effects into the analytical model, an effective plate length $l_{eff} = l + \Delta l$ and an effective plate width $w_{eff} = w + \Delta w$ are introduced. The values of the effective length and width are such that the coefficient of damping force for the enlarged plate with trivial boundary conditions has the same values as the coefficient of damping force of the real device size with the border effects, this concept is illustrated in Fig. 4.13.

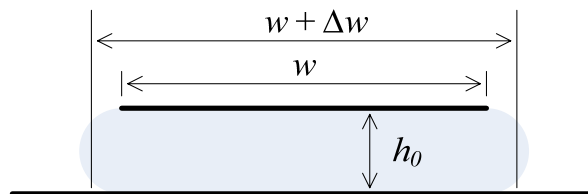


Figure 4.13: Schematic diagram of extended squeeze film model.

One method to predict the elongation caused by the border effect on parallel surfaces was

proposed by Veijola *et al.* [77, 78]. A series of two dimensional and three-dimensional FEM simulations were performed and, based on the results, approximations for the elongations were extracted. Veijola *et al.* obtained a very simple conclusion for a slender beam:

$$\Delta w = 1.3h_0. \quad (4.42)$$

The damping coefficient due to the fluid in the gap is

$$c_{squ,ex} = \frac{\eta l (w + 1.3h)^3}{h_0^3}. \quad (4.43)$$

The quality factor consequently is

$$Q_{squ,ex} = \frac{\rho_b w t \omega}{\eta (w + 1.3h_0)^3} h_0^3. \quad (4.44)$$

Effective fluid viscosity η_{eff} (cf. eq. (3.6)) can be used instead of dynamic viscosity η , to account for the non-continuum fluid behavior at very low pressures or for a very narrow gap.

Unsteady Navier-Stokes model

Another method to deal with moderate gaps can be based on some form of the Navier-Stokes equations. For a beam undergoing normal oscillations in a viscous fluid, the general form of the hydrodynamic force in the vibration direction is given in eq. (4.19). Results for $h_0/w \rightarrow \infty$ are identical to those obtained in Section 4.2.1. For the imaginary component $\Gamma_{squ,imag}$, the low Re , small h_0/w asymptote is obtained by using lubrication theory:

$$\Gamma_{squ,imag} = \frac{1}{\pi} \left(\frac{w}{h_0} \right)^3 \frac{1}{Re}. \quad (4.45)$$

Note that this result is consistent with that from the incompressible Reynolds equation. The hydrodynamic functions for micro beams vibrating close to a surface have been derived in [79, 80]. They depend on the ratio of the gap to the width of the micro beam and, unfortunately, in those references there is no unique expression for all gap-to-width ratios. In later work of Tung *et al.* [81], semi-analytical formulas for the calculation of the two-dimensional hydrodynamic function are obtained by using data fitting from the numerical solution. The two-dimensional hydrodynamic function is represented as $\Gamma_{squ}(Re, H)$, where H is the nondimensional gap height, defined as $H = 2h_0/w$. The general form of the semi-analytical formula for the hydrodynamic function is $\Gamma_{squ}(Re, H) = 10^{\Gamma_L}$ where

$$\begin{aligned} \Gamma_L(Re, H_L) = & a_1 + a_2 Re_L + a_3 Re_L^2 + a_4 Re_L^3 + a_5 Re_L^4 + a_6 Re_L H_L + a_7 H_L \\ & + a_8 H_L^2 + a_9 H_L^3 + a_{10} H_L^4 + a_{11} Re_L H_L^2 + a_{12} Re_L^2 H_L + a_{13} Re_L H_L^3, \\ & + a_{14} Re_L^3 H_L + a_{15} (Re_L H_L)^2 + a_{16} (Re_L H_L)^3 \end{aligned} \quad (4.46)$$

$H_L = \log_{10}(H)$, and $Re_L = \log_{10}(Re)$. The coefficients a_k , $k = 1, 2, \dots, 16$, have complex values. They are tabulated in Tung *et al.*'s paper. The fit is valid in the range of $10^{-2} < Re < 10^4$ and $10^{-1} < H < 10$. The Q factor due to the fluid damping is defined by

$$Q_{squ,NS} = \frac{4\rho_b t}{\pi\rho w \Gamma_{squ,imag}}. \quad (4.47)$$

The calculations are technically valid only when the continuum hypothesis holds. This is because the theory is based upon a subset of the Navier-Stokes equations, which are based on a continuum assumption. The useful range of this semianalytical expression can be extended beyond the continuum regime and into the slip and transition regimes by using an effective viscosity concept.

Thermo-mechanical resonance model

To deal with the large gap problem, Schwarz *et al.* [82] proposed a novel concept on analyzing and interpreting the measured quality factor curves. A qualitative and quantitative replication of the quality factor curves can be achieved by the combination of different damping mechanisms, e.g. intrinsic damping, molecular gas damping, viscous damping and the so called “dynamic” damping, squeeze film damping is only significant for very small gaps. The weighting of individual quality components has been achieved by multiplying a fitting parameter ξ .

Q_{int} : The intrinsic quality factor Q_{int} is determined exclusively by the resonator solid and is constant over the entire pressure range.

$$Q_{int} = \xi_{int}. \quad (4.48)$$

Q_{mol} : The quality factor due to molecular gas damping Q_{mol} prevails in the low pressure regime for Knudsen numbers $Kn \gg 1$. It is inversely proportional to the ambient pressure by:

$$Q_{mol} = \xi_{mol} / p. \quad (4.49)$$

Q_{vis} : The viscous quality factor Q_{vis} , due to Stokes friction, is related to the pressure and reflected in the double logarithmic representation by a straight line of slope -0.5. It is effective above about 10 mbar, corresponding to Knudsen numbers $Kn \ll 1$ therefore results in the description:

$$Q_{vis} = \xi_{vis} / \sqrt{p}. \quad (4.50)$$

Q_{dyn} : To interpret the damping mechanism in the transition region between molecular and viscous flow, a new model was developed. It transfers the calculation of thermoelastic damping in solids to the dynamic damping in gases, accounting for the thermal energy flow. The quality factor of dynamic damping Q_{dyn} is:

$$Q_{dyn} = \xi_{dyn} \frac{f_{0,dyn}^2 + f_r^2}{f_{0,dyn} f_r}, \quad (4.51)$$

with the resonance frequency f_r of the resonator and a fitting factor ξ_{dyn} . The thermal resonance frequency is:

$$f_{0,dyn} = \frac{\pi a_p}{2h_0^2}, \quad (4.52)$$

and

$$a_p = a \left(\frac{p_a}{p} \right)^{\varepsilon_{dyn}} = a \left(\frac{1000 \text{ mbar}}{p} \right)^{\varepsilon_{dyn}}. \quad (4.53)$$

The pressure-dependent parameter a_p is $19.22 \times 10^{-6} \text{ m}^2/\text{s}$ for N_2 gas when pressure p is 1000 mbar. More flexibility could be achieved by extending the root component ε_{dyn} from 0.41 to 0.64 for individual cases.

From eq. (4.51) it can be seen that Q_{dyn} has a minimum at a critical position, the position is determined by the coincidence of the mechanical resonance frequency of the resonator with the thermal frequency response of the gas. At this coincidence, a maximum of energy is extracted from the system, thus leading to the locally lowest quality factor.

4.3.2 Comparison between experimental, analytical and simulated results

Comparisons of the predictions from squeeze film, extended squeeze film and unsteady N-S models with the experimental data, as well as the COMSOL FSI simulations, were performed first. The resonator structure and its measurement results have been presented in Section 3.3. Fig. 4.14 shows the results for the 1st bending mode of the B2 bridge resonator oscillating in atmospheric N_2 environment at room temperature, and at various gap heights. In comparing with the experimental data, some care must be taken to remove the intrinsic damping of the resonator. The intrinsic damping in the experimental data was obtained by operating the resonator in HV, this damping was subsequently removed from the experimental data mathematically, leaving only the damping due to the fluid to be analyzed.

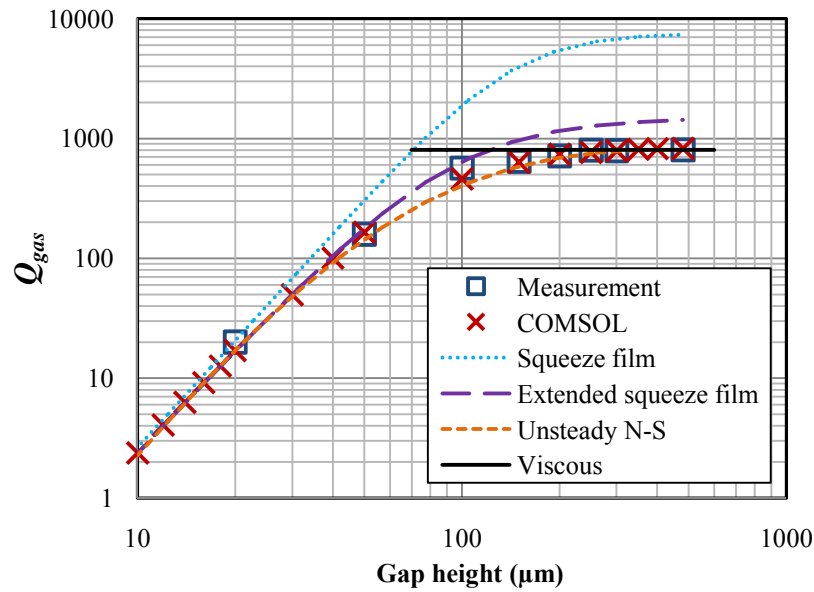


Figure 4.14: Plot showing the quality factors due to gas damping of the *B2* bridge resonator in the fundamental mode in atmospheric N_2 . The squares represent the measured Q factor due to gas damping, which are derived from the measurements after subtracting intrinsic damping, while the crosses are the predictions based on the COMSOL simulation. The dashed lines represent the analytical/semianalytical calculations, and the solid line shows the viscous model prediction, which is the limit for a structure without gap.

It is evident from this comparison that decreasing gap height h_0 results in a corresponding decrease in the quality factor. This decrease is quite dramatic for $h_0 < 50 \mu\text{m}$, as expected from squeeze film theory that the dissipation in the fluid varies as h_0^{-3} . When h_0 increases further, the classic squeeze film theory begins to underestimate the fluidic dissipation, while the calculations from the extended squeeze film model still exhibit a good fit to experiments as far as $h_0 = 100 \mu\text{m}$, since it accounts for the “leaked” gas effect outside the borderline. The quality factors derived from unsteady N-S model agree well with the COMSOL simulations, since the former is obtained by using data fitting from the numerical solution of N-S equations. Both the models are in close agreement with the experimental results.

Fig. 4.15 compares theoretical and experimental squeeze film quality factors of the *B2* bridge resonator with different gaps over a range of ambient pressures. The experimentally measured quality factor at each ambient pressure is plotted with a solid diamond-shaped point. Both Reynolds equation and Navier-Stokes equation are based on a continuum assumption ($Kn \leq 0.1$). In order to obtain effectiveness of the equations for squeeze film damping in a rarefied gas, the “coefficient of viscosity” η is replaced by an “effective” viscosity η_{eff} , which is dependent on the pressure via Knudsen number, cf. eq. (3.6). Such models that use the concept of an effective viscosity are expected to predict the gas damping even into the free molecular regime (moderate to high Knudsen numbers) for some specific cases. The concept

will be examined in the following.

The traditional squeeze film damping model underestimates the damping (overestimates Q factor) and the divergence increases rapidly as the gap height increases. In contrast, the extended squeeze film model predicts well the squeeze film gas damping up to gaps of 50 μm . Beyond this point some moderate deviation occurs. This model accurately predicts the gas damping well into the free molecular regime, indicating the “effective viscosity” concept is reasonable to account the rarefaction effect of the gas in a narrow gap.

The semi-analytical predictions from the unsteady N-S model are in better agreement with the experimental results as compared to the other two models. Three observations can be concluded from the comparisons: 1) for very narrow gap, e.g. 20 μm , the N-S equation predictions are as good as those from Reynolds equation at full pressure range; 2) for moderate to large gaps and at high pressure ranges, the calculations from the N-S equation fit well with the measurements; and 3) the disagreement tends to be maximum for bigger gaps and lower pressures, indicating the effective viscosity concept is not appropriate in that case. The viscous model is also compared in Fig. 4.15 g), in the viscous regime, the viscous model fits well with the measurements, but when the pressure decreases into the transition regime, this model loses its validity.

It is apparent that the presence of a wall can affect the behavior of the dissipative loading as $Re \rightarrow 0$ even at large separations. In this case, the concept of effective viscosity would become questionable, and the flow models based on continuum flow is no more valid. For $Kn \gg 1$, i.e. the gap distance is much smaller than the mean free path of the gas molecules, a free molecular model can be considered. But in the slip regime ($0.1 < Kn < 10$), to our best knowledge, a compact and universal solution does not yet exist. Schwarz's [82] proposal is developed to explain the gas damping behavior in this case and the proposal will be examined next.

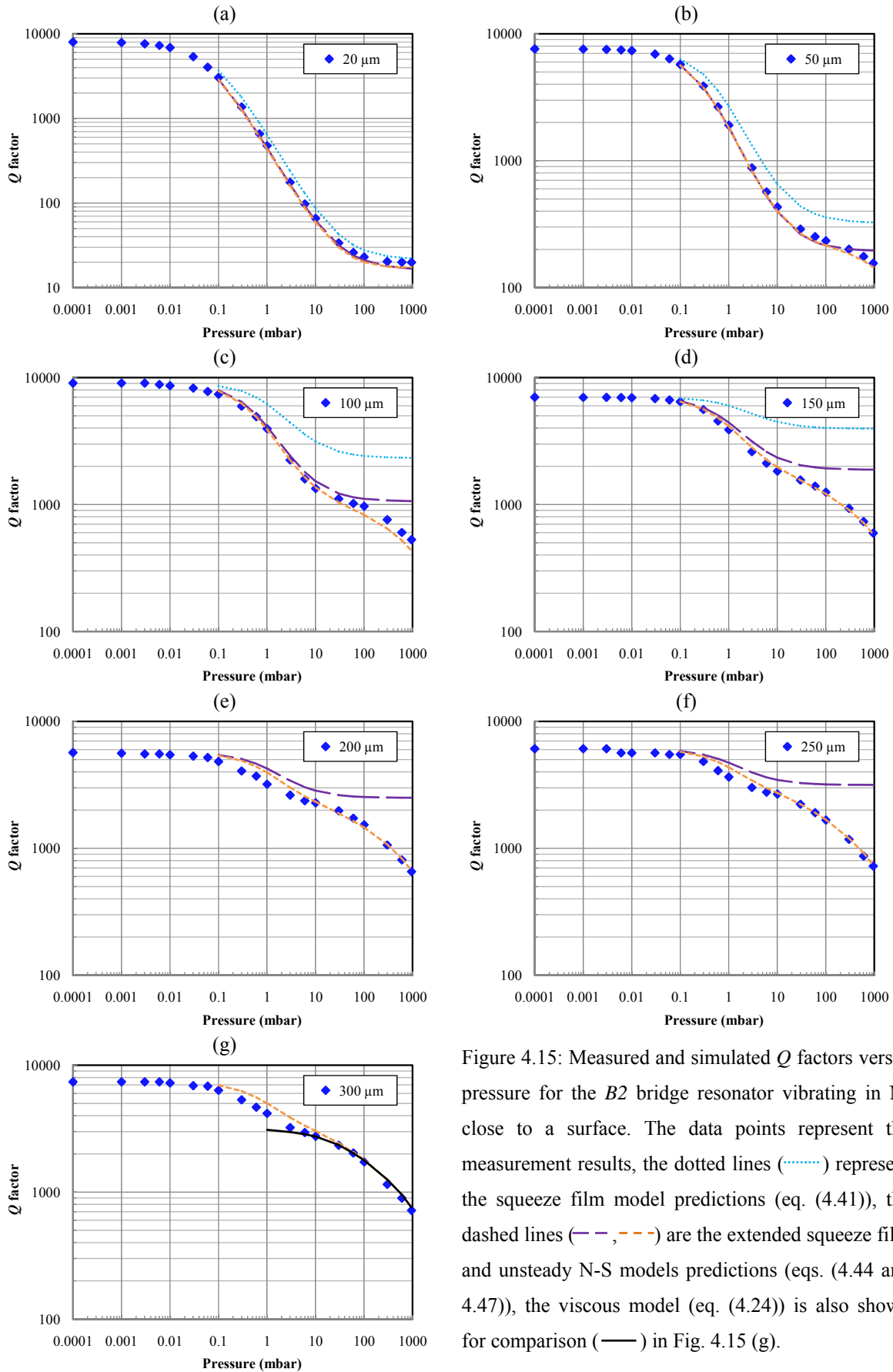


Figure 4.15: Measured and simulated Q factors versus pressure for the $B2$ bridge resonator vibrating in N_2 close to a surface. The data points represent the measurement results, the dotted lines (.....) represent the squeeze film model predictions (eq. (4.41)), the dashed lines (—, - - -) are the extended squeeze film and unsteady N-S models predictions (eqs. (4.44 and 4.47)), the viscous model (eq. (4.24)) is also shown for comparison (—) in Fig. 4.15 (g).

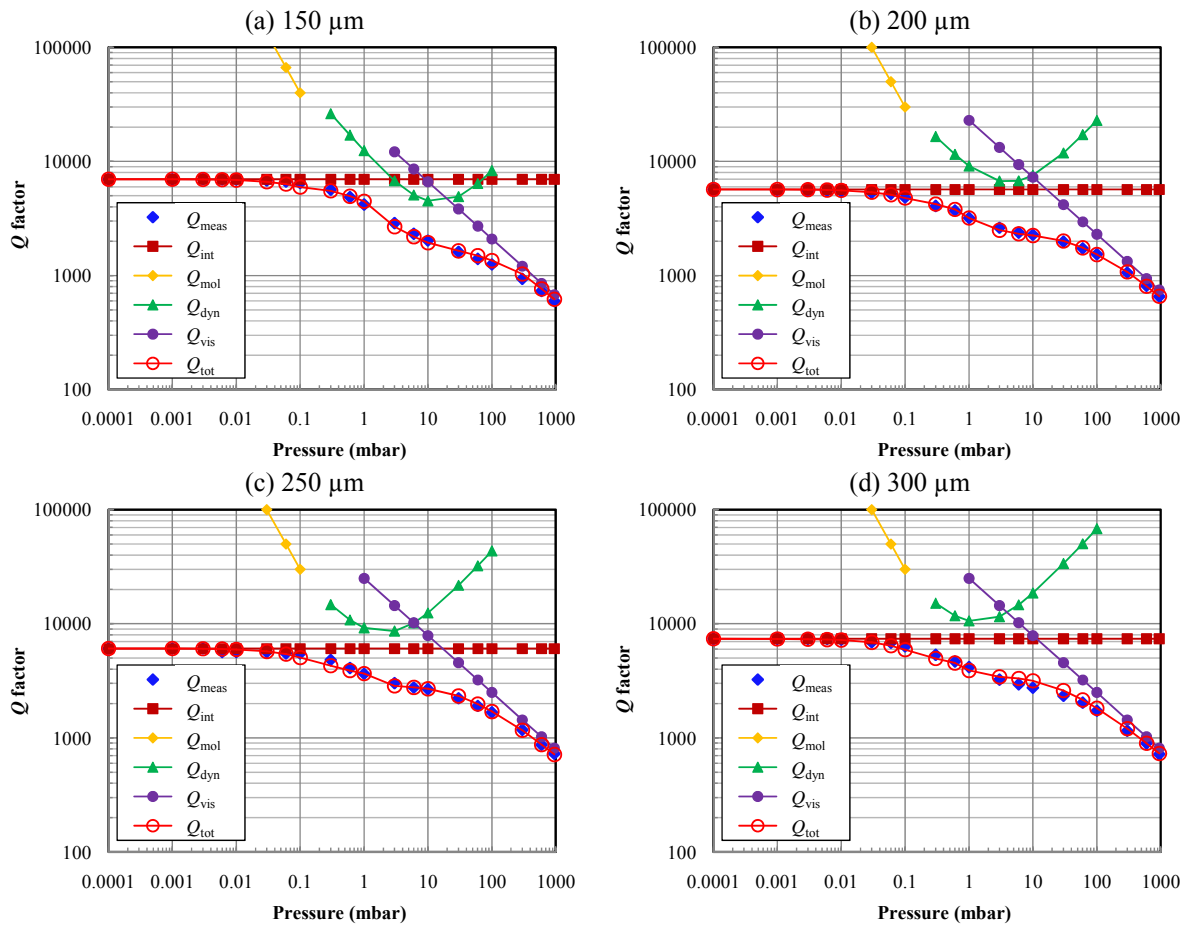


Figure 4.16: Qualitative approximation of the Q factors for the bridge resonator vibrating close to a surface with different gap sizes in N_2 environment.

h_0	ξ_{int}	ξ_{mol}	ξ_{vis}	ξ_{dyn}	ε_{dyn}
μm	-	mbar	$\sqrt{\text{mbar}}$	-	-
150	6999	4000	21000	2200	0.64
200	5690	3000	23000	3300	0.6
250	6082	3000	25000	4200	0.6
300	7387	3000	25000	5200	0.6

Table 4.1: Overview of the determined adjustment factors ξ from the replica of the quality curves for the different gap heights h_0 in Fig. 4.16.

The pressure dependent measured curves were fitted based on a quantitative superposition of quality factor components based on different physical damping effects. The weighting of individual quality factor components was achieved by multiplying the respective pressure dependence function with adjustment factors. Tab. 4.1 lists the adjustment factors ξ of individual quality factor components. These were determined with the objective of the best possible match of Q_{meas} and Q_{tot} . With these specifications, the measured quality factor curves

could be reproduced with very good agreement to the experimental values.

A systematic review of the quality curves of the resonator for the measured gap distances $h_0 = 150, 200, 250$ and $300 \mu\text{m}$ are presented in Fig. 4.16. The quality in the high vacuum regime is determined solely by the intrinsic quality factor Q_{int} . In this regime the gas damping can be negligible. As the pressure increases, the gas molecular density increases and the damping due to free molecular gas flow will reach a value that is in the same order as the intrinsic damping of the solid structure. For the regime $p \leq 1 \text{ mbar}$ ($Kn \geq 1$) it can be described solely by these two components. For small Knudsen numbers, corresponding to higher pressures, the gas damping model determined by free molecular flow loses its validity. Q_{dyn} is used to account for the gas damping in the transition regime $p \approx 1 \text{ mbar}$ to 10 mbar . Very importantly, the location of minimum Q_{dyn} obtained by the thermal resonance frequency $f_{0,dyn}$ (eq. (4.52)), is determined and verified. At higher pressure, e.g. $p > 100 \text{ mbar}$, the quality factor shows a $1/\sqrt{p_a}$ proportionality to the pressure, depicting in this regime Q_{vis} dominates. While at intermediate pressure region ($0.01 < Kn < 0.1$), the measured Q factor curves can be better fitted by the interaction of Q_{int} , Q_{vis} and Q_{dyn} .

It can be seen that Q_{dyn} is a function of the ambient pressures p and has a distinct minimum, the position is determined by the coincidence of the mechanical resonance frequency of the oscillator with the thermal frequency response of the gas. The impact area is located in the transition zone of the molecular to viscous flow above about 0.3 mbar up to 100 mbar , approximately.

4.3.3 Discussion

Overall, the traditional squeeze film model can be used to predict the gas damping for narrow gaps, e.g. the ratio of the resonator width to gap height w/h_0 is bigger than 10. By using the “effective viscosity” concept, the model can also be used to account for the rarefaction effect of the gas in a narrow gap. By taking boundary effects into account the extended squeeze film model is valid for $w/h_0 \geq 4$. When the gap height is even bigger, predictions of the semi-analytical formulas from the unsteady N-S model should be used. The results from this model are in close agreement with those based on fully three-dimensional FSI simulations and with the experimental measurements in the viscous regime. For the measurements in lower pressure at large separations, a newly developed thermo-mechanical resonance model is used to interpret the results. This model transfers the calculation of thermoelastic damping in solids to the dynamic damping in gases, accounting for the thermal energy flow.

Moreover, the quality factors generally increase with increasing gap height and resonant mode. As shown in Fig. 3.28 in the last Chapter, although the intrinsic quality factor in the 3rd mode is lower than the 1st mode, 2000 compare to almost 8000, the quality factors in atmospheric pressure increased from 20 to 146 and from 156 to 477 at 20 μm gap and 50 μm gap, respectively. This result can be explained as follows. When the resonator vibrates in a particular mode, a boundary layer is set up around the beam. The boundary layer thickness is known to be $\sqrt{2\eta/\rho\omega}$. When the gap between the resonator beam and the surface becomes comparable to the boundary layer thickness, the squeeze film effects start to emerge. Because higher modes have higher frequencies, they generate a thinner boundary layer around the beam. Consequently, a resonator oscillating in its higher mode can experience much less fluidic damping due to squeeze film effect.

5. Analysis of intrinsic damping in piezoelectric micro resonators

When a resonator is operated in high vacuum, external fluidic damping as discussed in previous Chapters becomes negligible. In this case, energy dissipation inside the materials of the resonator (so-called intrinsic damping) becomes dominant. Intrinsic damping is induced by numerous physical and/or chemical processes. Sources of dissipation generally include thermoelastic damping (TED), anchor losses, thin film coating losses and others. The different kinds of intrinsic damping mechanisms contribute to the overall damping of a resonator. It is not easy to exactly identify which one is more dominant than the others, and many of them still need further investigation.

In this Chapter we focus on three major damping effects on piezoelectric micro resonators, which are TED, anchor loss and coating loss. Since the different dissipation mechanisms generally appear mixed with each other, it is difficult to explore individual ones experimentally. Hence, in the first Section of this investigation, we employ both analytical and numerical methods to predict TED for different geometries and resonant modes of cantilevers. In the second Section the anchor loss is systematically studied; available analytical solutions are reviewed and compared with numerical simulations. The third Section focuses on the damping effect of the piezo-electrode stack deposited on the cantilevers. Finally, a series of experimental validations are conducted on different structures of piezoelectric cantilevers, showing that the analysis in this Chapter can yield a qualitative match with measurements.

5.1 Thermoelastic damping (TED)

TED has been identified as an important loss mechanism in numerous high Q micro resonators. A mechanical expansion in a solid lowers the temperature and a compression raises the temperature. The key process of TED is that energy is dissipated through the irreversible flow of heat from hot to cold regions of the solid. When the vibration frequency is much lower than the heat relaxation rate, the solid is always in thermal equilibrium and the vibrations are isothermal. On the other hand, when the vibration frequency is much higher than the heat relaxation rate, the system has no time to relax and the vibrations are adiabatic. Hence, when the vibration frequency is of the order of the relaxation rate, the energy loss due to TED becomes considerable.

In this work, both the analytical model from Zener [83, 84] and numerical simulations using

COMSOL are reviewed and compared. For piezoelectric cantilevers, there is a piezo-electrode stack coated on the silicon beam. Furthermore, cantilevers can be operated in higher resonant modes. From the view point of piezoelectric resonator applications, the concerns about the piezo-electrode stack and higher resonance mode effects are addressed in this part of research.

5.1.1 Analytical model for TED

In the original papers by Zener [83, 84], the phenomenon of TED was analyzed for a one dimensional case, specifically in a cantilever beam. Zener calculated the temperature field developed in the cantilever due to the periodic strain field for a one dimensional system. Using the temperature field, he calculated the bending moment caused by the temperature gradient in the cantilever. Finally, the quality factor of a flexural vibrating cantilever limited by TED loss can be expressed as:

$$Q_{TED} = \frac{\rho_b C_p}{\alpha_T^2 TE} \frac{f_r^2 + F_0^2}{f_r F_0}, \quad (5.1)$$

herein α_T and E are linear thermal expansion and elasticity modulus of the cantilever material, and F_0 is the thermal relaxation frequency, defined as $F_0 = \pi\kappa/2\rho_b C_p t^2$. Q_{TED} has a minimum at $f = F_0$, where the heat energy generated from the material internal friction dissipates completely, this agrees with the previous qualitative explanation.

5.1.2 Numerical simulation for TED

The analytical approximation can be used for the TED prediction. However there are still some concerns. Firstly, for resonators with complicated geometries, the analytical approximation may not give a good TED prediction; secondly, if the resonator is composed of different materials, i.e. the resonator is covered by metal electrode layers, the approximation does not includes such effects; thirdly, higher resonant modes, such as torsional mode and longitudinal mode, may also experience TED if there is a local volume change when deformed. Such effects can only be included by a numerical simulation for TED analysis. We used the software package COMSOL as platform to carry out the TED simulation by calculating the eigenfrequency of the system. One example for the TED simulation of a cantilever is shown in Fig. 5.1. The figure shows the cantilever deformation and the corresponding temperature distribution under the first resonant mode.

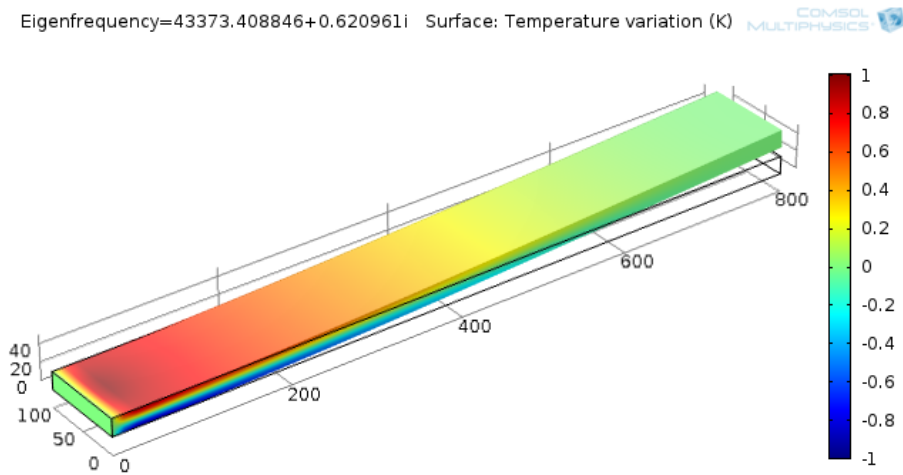


Figure 5.1: Fundamental mode shape and corresponding temperature distribution within a cantilever.

5.1.3 Comparison between analytical and simulated results

The resonators were made of single crystal silicon, which is an anisotropic material. Since the models shown above both are based on the assumption of isotropic materials, we can use the material properties of single crystal silicon along the $\langle 100 \rangle$ orientation for the model. Since the boundary planes of the fabricated beam resonators are all $[100]$, this material property approximation does not lead to a big error. The relevant properties of silicon as well as of other materials used in this work are listed in Tab. 5.1.

The simulation is carried out for different resonance frequencies corresponding to the different lengths of the cantilever. The beams are fixed to be $100 \mu\text{m}$ wide and $20 \mu\text{m}$ thick, while the length is varied from $50 \mu\text{m}$ to $2000 \mu\text{m}$. The fundamental mode frequency is inversely proportional to the beam length square in this experiment. The calculated quality factors from the finite element model were compared to those from the analytical expression of Zener (eq. (5.1)) for Si beams with identical geometry, omitting the deposited layers.

Property	Material	Symbol	Value
Density (kg/m ³)	Si [100]	ρ_{Si}	2330
	AlN	ρ_{AlN}	3300
	Au	ρ_{Au}	19300
Young's modulus (Pa)	Si [100]	E_{Si}	1.7×10^{11}
	AlN	E_{AlN}	3.4×10^{11}
	Au	E_{Au}	7.0×10^{10}
Poisson's ratio	Si [100]	ν_{Si}	0.28
	AlN	ν_{AlN}	0.3
	Au	ν_{Au}	0.44
Thermal expansion coefficient (K ⁻¹)	Si [100]	α_{Si}	2.6×10^{-6}
	AlN	α_{AlN}	2.6×10^{-6}
	Au	α_{Au}	1.4×10^{-5}
Heat capacity at constant pressure (J/(kg K))	Si [100]	C_{psi}	700
	AlN	C_{pAlN}	819.7
	Au	C_{pAu}	129
Thermal conductivity (W/(m K))	Si [100]	κ_{Si}	130
	AlN	κ_{AlN}	30.1
	Au	κ_{Au}	317
Environmental temperature (K)		T	300

Table 5.1: Properties of the materials used in the analytical calculation and COMSOL simulation. The values are obtained from the material database of COMSOL software.

Qualitatively, Fig. 5.2 shows that the finite element model is in reasonable agreement with the analytical expression; it displays the same high frequency and low frequency dependence, as well as Q factor magnitude. However, the analytical calculations are not in quantitative agreement with the simulations. It can be seen that there is an increasingly large discrepancy between them at smaller beam lengths. The fundamental assumption in Zener's calculation is that the heat transfer occurs only in the transverse direction, while the thermal gradient in the longitudinal direction is simply omitted. The various contributions to the discrepancy between the calculations may be thought as contributing to this assumption.

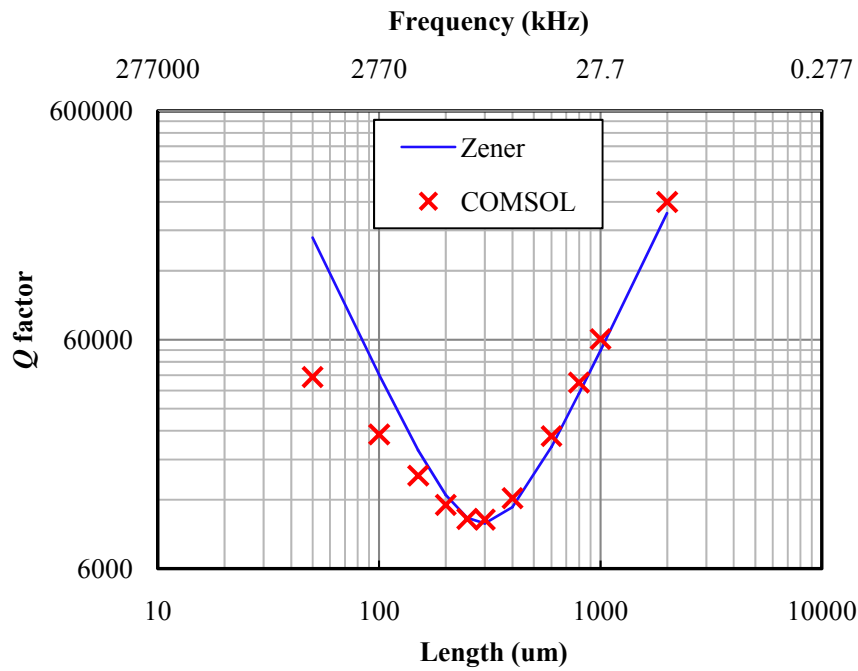


Figure 5.2: Comparison of Zener's analytical model (solid line) and COMSOL simulation ('x' marks) for TED. The width and thickness of the cantilever is held fixed at 100 μm and 20 μm , the length is varied from 50 μm to 2000 μm . Since the frequency is inversely proportional to length squared, the shorter length corresponds to higher frequency.

Furthermore, we check the effect of resonant mode and thin film coating on TED here. A piezoelectric cantilever, with dimensions 800 μm long, 100 μm wide and 20 μm thick, is used in this research. There is a piezo-electrode stack (1 μm thick AlN film and 300 nm thick Au film) coated on the clamped end of the cantilever with a cover percentage of 20%. This cantilever is simulated up to the 7th resonant mode and the simulation results are shown in Fig. 5.3. For comparison, the TED results from both Zener's equation and COMSOL simulation for a pure silicon cantilever with the same size are also presented. For this cantilever in flexural modes, the critical frequency F_0 is calculated to be 313 kHz, which is very close to the resonance frequency of the 2nd flexural mode, thus leading to a minimum of Q factor. TED is very weak for purely torsional resonators as the deformation is nearly isochoric. TED analysis for the lateral mode is similar to the flexural mode since the cantilever is also bending but in the in-plane direction.

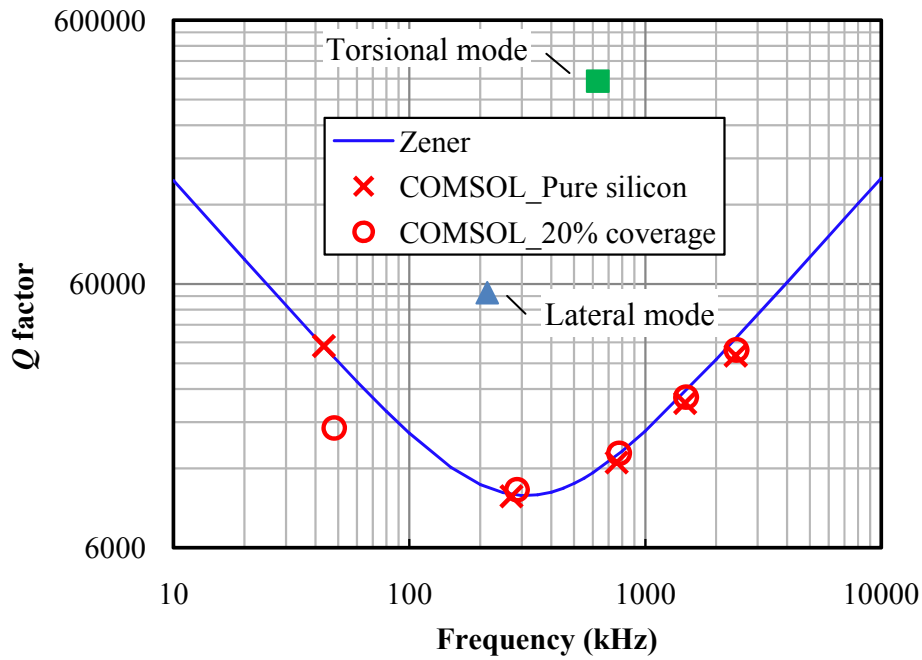


Figure 5.3: TED for higher modes of a micro cantilever with dimensions $800 \times 100 \times 20 \mu\text{m}$. The solid line is Zener's calculation, the 'x' marks represent COMSOL simulations for the flexural modes of the pure silicon beam. The simulation results for torsional and lateral modes are represented by solid square and triangle points. For comparison, the flexural mode TED of the beam covered by 20% piezo-electrode stack are also simulated and shown by the 'o' marks.

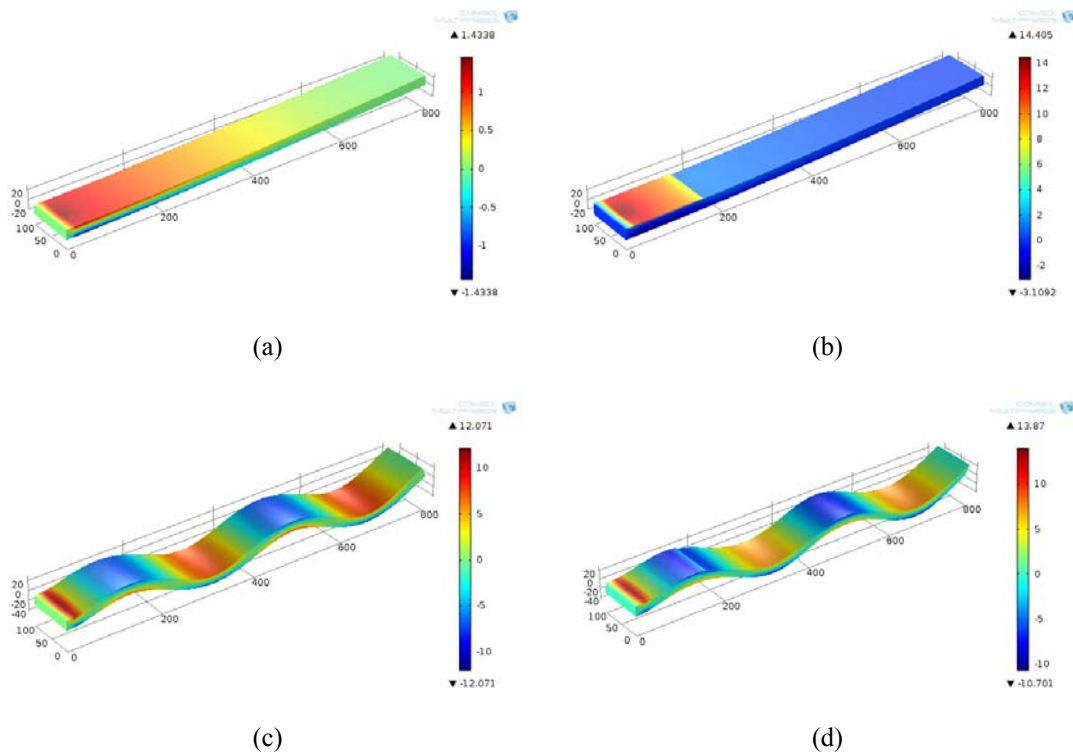


Figure 5.4: Temperature variation of the cantilever beam (a) without the piezo-electrode stack under the first flexural mode, (b) with the stack under the first flexural mode, (c) without the stack under the fifth flexural mode and (d) with the stack under the fifth flexural mode.

The influence of the piezo-electrode stack is also investigated. From Fig. 5.3 it can be seen that the presence of the stack covering 20% of the cantilever decreases the quality factor mainly in the first mode. Fig. 5.4 compares the temperature increment magnitude distributions corresponding to different bending modes of the resonator beam with and without stack, respectively. For the first mode, the stack modifies the temperature distribution on the surface of the beam, creating a temperature gradient mainly through the stack so that the quality factor decreases significantly. When the flexural mode number increases, the stack's influence on the temperature gradient decreases, since the resonator is only partially covered by the stack.

5.1.4 Conclusion

In this work we used the numerical simulation as a validation tool to check the validity for Zener's analytical model for TED. We compared the simulation results for cantilevers with different lengths or alternatively different resonance frequencies. It has been shown that the analytical model is not generally sufficient for studying real complex 3-D structures due to inherent restrictive assumptions. Furthermore, for piezoelectric resonators, the analysis shows that the piezo-electrode stack plays an important role in the quality factor.

5.2 Anchor losses

For MEMS devices vibrating in a HV environment, the second source of dissipation is due to the energy loss from the vibrating beams through their supporting structure. As the beam vibrates, it causes the supporting structure to deform slightly, thereby leading to the generation and propagation of elastic stress waves from the resonator to the surrounding material. Typically, the larger part of this energy flow is not reflected back into the cantilever [154]. Therefore, this mechanism is generally recognized as a source of dissipation, usually referred to as anchor loss, support loss or clamping loss.

The objective of this Section is to review and compare different analytical anchor loss models from the literature [93-98] and from numerical simulation, thus gain an improved understanding of the factors that influence anchor losses. General strategies to minimize anchor losses are also discussed in this Section.

5.2.1 Analytical models for anchor losses

To predict anchor loss analytically, the coupled resonator-support system must be considered in order to understand the interaction and energy transmission between them. The support is often assumed to be semi-infinite. Fig. 5.5 schematically shows three typical simplifications

of support structures.

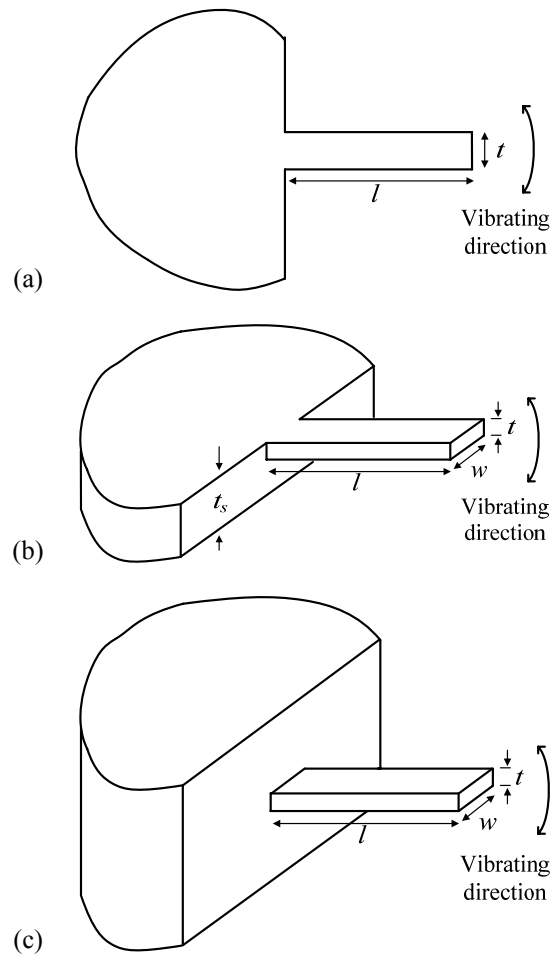


Figure 5.5: Schematic view of cantilever resonators connected to their support structures: (a) a cantilever attached to a semi-infinite support, the thickness is assumed to be infinite (2D assumption), (b) a cantilever attached to a support of finite thickness t_s , while lateral dimensions are assumed to be semi-infinite, and (c) a cantilever attached to a support that has semi-infinite space.

In 1968, Jimbo and Itao [93] derived an expression for the energy loss of a cantilever with an infinite thickness (a 2D assumption) and with the cantilever support considered as a semi-infinite large elastic body (refer to Fig. 5.5 (a)). Based on their fundamental work, several researchers derived the damping due to elastic energy radiation to the support as being proportional to the cube of the thickness to length ratio $(t/l)^3$. Hence, the quality factor Q_{anchor} of a resonator enduring only the anchor loss is estimated as:

$$Q_{anchor} = k \left(\frac{l}{t} \right)^3, \quad (5.2)$$

where k is a coefficient calculated as $k = 0.34$ [155], 2.081 [93] or 2.17 [94].

In practice, the support usually does not have the exact shape assumed in the 2D theoretical derivations. Judge *et al.* [97, 98] studied analytically the case of a 3D cantilever beam

attached either to a semi-infinite plate of finite thickness or to a semi-infinite space, by using beam theory and 3D elasticity theory. The closed-form expression for the quality factor in beam resonators attached to a semi-infinite plate of finite thickness t_s is (refer to Fig. 5.5 (b)):

$$Q_{anchor} = 1.05 \frac{l}{w} \frac{t_s^2}{t^2}. \quad (5.3)$$

While for resonators attached to a semi-infinite space, the quality factor is approximated as (refer to Fig. 5.5 (c)):

$$Q_{anchor} = 0.33 \frac{l}{w} \left(\frac{l}{t} \right)^4. \quad (5.4)$$

However, all these approaches contain simplifying assumptions which are generally difficult to quantify. The semi-infinite assumption is usually not realistic for practical MEMS devices. This is because the supporting structure often has dimensions of a similar order to the dimensions of the resonator itself. Furthermore, even under such assumptions, the analytical results also differ substantially from each other since the functional dependence of quality factors on geometrical features is completely different. E.g. in the simplest case of a cantilever beam of length l and square cross section of side t resting on a semi-infinite space, the quality factor is proportional to $(l/t)^3$ in 2D and to $(l/t)^5$ in 3D. It is reasonable to derive that the scaling may change for more realistic geometries of micromachined cantilevers. So detailed numerical analysis is required to estimate anchor losses.

5.2.2 Numerical simulation for anchor losses

The commercial FE package CoventorWare [156] is used here to simulate anchor losses for resonators. The solver in the software includes a so called “QuietBoundary” boundary condition (BC), which assumes the boundary to extend to infinity. This can be applied to predict how much elastic (vibrational) energy is dissipated via the anchor to the supporting structure.

One example silicon chip used in this research consists of a silicon frame and a beam attached to the frame at one end. The mesh model and dimensions are shown in Fig. 5.6; the cantilever thickness, which is not shown in the figure, is 20 μm . Since the resonator chip is glued on a PCB package, it is assumed that elastic waves propagate to infinity from the bottom of the chip. Thus a “QuietBoundary” BC is applied to the bottom face. In CoventorWare, the “QuietBoundary” BC is only supported for isotropic elastic material and can only be applied to meshes with linear elements. Linear Manhattan bricks are used to mesh the silicon chip model. In order to meet the requirement in the model for isotropic material, we use the

material properties of single crystal silicon along the $\langle 100 \rangle$ orientation for the model, the properties used in this work are listed in Tab. 5.1 shown earlier.

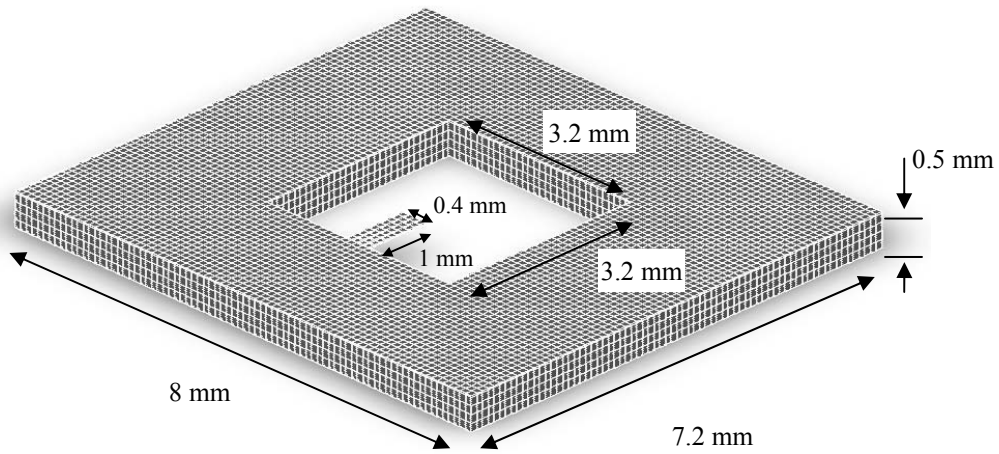


Figure 5.6: Geometry of the silicon chip and the meshed model.

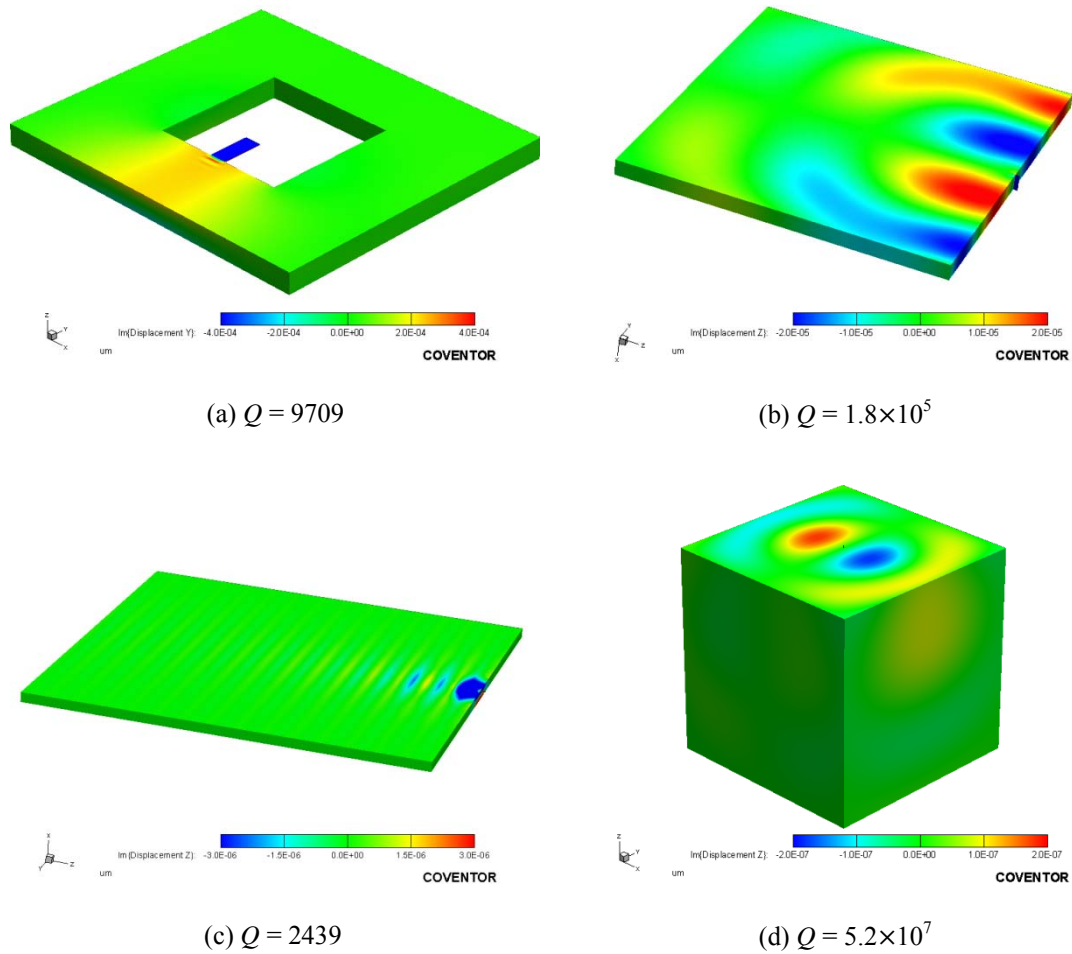


Figure 5.7: 3D illustration of energy dissipation for the cantilever vibrating in the first flexural mode through different substrates: (a) chip frame, (b) semi-infinite plate (corresponds to Fig.5.5 (a)), (c) semi-infinite plate with finite thickness (corresponds to Fig. 5.5 (b)) and (d) semi-infinite space (corresponds to Fig. 5.5 (c)).

Fig. 5.7 (a) shows the computed energy dissipation in the silicon chip for the cantilever vibrating in the first flexural mode. It can be seen that the bending motion of the beam generates and pumps elastic acoustic waves into the frame, where they carry away the energy of the resonance. The simulation result for the Q factor is 9709. Moreover, the analysis of Q factors of the cantilever beam resting on different semi-infinite support structures has also been performed, as shown in Figs. 5.7 (b)-(d), which correspond to the support structures schematically shown in Figs. 5.5 (a)-(c). One basic assumption in the analytical models is that the support structure is semi-infinite. To meet this assumption in the simulations, the substrate size is set as large as the acoustic wavelength in the substrate at the frequency of interest. Numerical studies suggest that when the substrate size is of the order of one wavelength, an error of 5-10% is obtained, while larger substrates do not yield significantly higher accuracy. In this figure, it can be seen that, even under this assumption, the calculated Q factors for the same cantilever with different support geometries are completely different by orders of magnitude, varying from 2439 to 5.2×10^7 .

5.2.3 Comparison between analytical and simulated results

Cantilever beams vibrating in the fundamental mode are studied to compare and validate the different analytical models. The beam width and thickness are fixed as $100 \mu\text{m}$ and $20 \mu\text{m}$, the Q factor is plotted as a function of the length of the beam in Fig. 5.8. To meet the semi-infinite substrate assumption in the analytical models, the substrate size is set as large as one acoustic wavelength for each case except for the realistic chip where the substrate size is kept constant at the values shown in Fig. 5.6.

It is shown that the simulations are in reasonable agreements with different analytical models under specific supporting substrate simplifications. It is important to note that, even under simplified support assumptions, the dependence of quality factors on geometrical features is completely different. Moreover, the semi-infinite support assumption is usually not realistic for practical MEMS devices. Cantilevers with chip support structure as shown in Fig. 5.6 are simulated and the results are also presented in Fig. 5.8. The support boundaries have an important effect on the motion of the resonator-support structure and thus on the energy dissipation. Hence, for more realistic geometries of micromachined cantilevers, numerical techniques for the prediction of anchor losses are required.

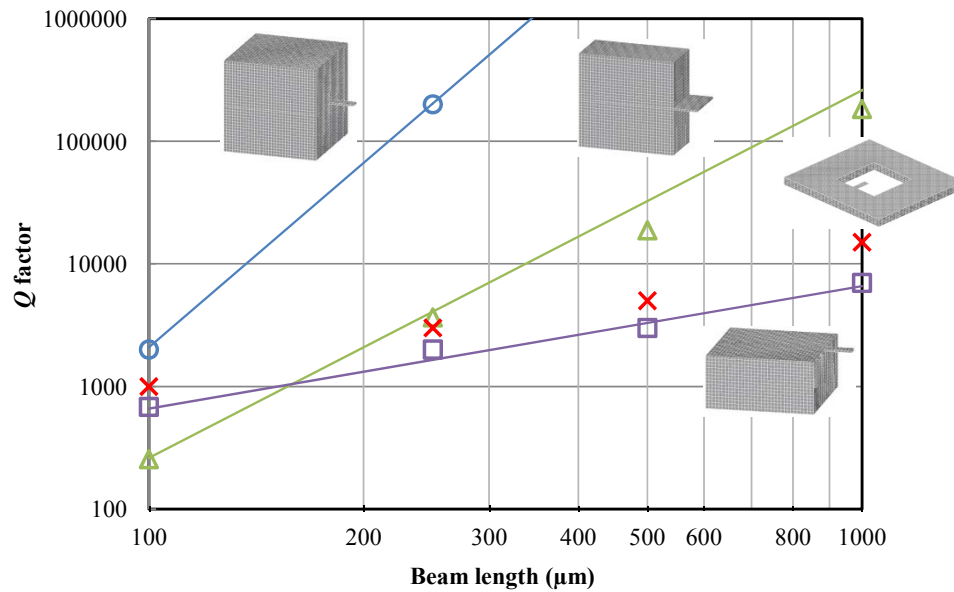


Figure 5.8: Comparison of Q factors resulting from anchor losses calculated using the three different analytical models (solid lines) and corresponding CoventorWare simulation (depicted by marks) under the same boundary assumptions. The width and thickness of the cantilevers are held fixed as $100\ \mu\text{m}$ and $20\ \mu\text{m}$, the lengths are varied from $100\ \mu\text{m}$ to $1000\ \mu\text{m}$. For anchor losses in the realistic chips (red 'x' marks), there is no available analytical model.

5.2.4 Discussion

We have compared the anchor loss of a cantilever attached to different support geometries and have found that the results may differ by orders of magnitude. Basically longer and/or thinner beams as well as larger supporting substrates exhibit lower anchor losses. Alternatively, more sophisticated designs can be employed by the assistance of a numerical simulation tool. Careful design of the resonator and its attachment to the support can reduce anchor losses by reducing motion of the attachment point, thereby reducing the coupling between the resonator and the surrounding material [157]. Such systems may involve a mounting mechanism, which isolates shear and moment reactions from the support [158, 159], or the introduction of blocking masses to reduce the vibration transmitted to the boundaries [160]. Besides, some preliminary experiments have shown that by placing anchors at nodal points, anchor losses can be minimized [161]. Thus, designing resonators to have a symmetric mode shape and placing anchor points at the nodes can reduce anchor losses.

5.3 Damping by thin film coating

Nevertheless, neither TED nor anchor losses can account alone for the measured dissipation of piezo-transduced resonators. There is experimental evidence that other effects should be included. For example, the calculated Q factors, which include TED and anchor losses, were

3088, 7062 and 28066 for C6-type cantilevers with different thicknesses of 57, 37 and 22 μm . However, the Q factors were measured as 3408, 3811 and 6897, respectively under HV conditions. The difference between measured and calculated Q factors increases when decreasing the cantilever thickness. This indicates that unforeseen energy dissipation exists in thin cantilevers. As another example, a capacitive plate resonator [73], with similar design as that shown in Section 4.1, has demonstrated a much higher Q factor for the first flexural mode ($Q \approx 40000$ compared to 6284), which can approach the fundamental limits of dissipation established by TED and anchor losses. Since there is no AlN or Au thin film sputtered on the beam surface of this capacitive counterpart, the most likely reason for the low Q factor of piezo-transduced resonators is the effect of these coating films.

Understanding how the coating film changes the overall damping characteristics is helpful for the Q factor predictions for a micro thin film coated resonator. In most previous literature [103, 104] where the coating effects were investigated, the resonators were full covered by coating films and the research interests were focused on the coating thickness effect on the resonators. In this work, a series of cantilevers which were covered by the coating in 20-100% coverage of the beam length were measured. In this way the damping effect of the thin film coating pattern can be explored in a more detailed way.

5.3.1 Experiments

In order to observe the effect of the coating patterns, two types of cantilevers were fabricated and characterized. The first type cantilever has a length of 2200 μm and a width of 400 μm , the second type is 1200 μm long and 200 μm wide. The thicknesses of all cantilevers are designed uniformly as 20 μm , the variation is controlled to below ± 3 μm . Cantilevers of both types have piezo-electrode stacks (1 μm thick AlN film and 300 nm thick Au film) sputtered on top of the beam and the coverage varies from 20% to 100%, starting from the cantilever suspension (as schematically shown in Fig. 5.9). The cantilevers are characterized in HV for the first flexural mode, for obtaining the intrinsic damping. The resonance frequency is shown in Fig. 5.10, the variation of the frequency is mainly due to the thickness difference of each beam and the coating film coverage variation.

By characterizing the cantilevers in HV environment, the relative effect of a piezo-electrode coating on the intrinsic properties of the cantilever can be explored. Fig. 5.11 (a) shows the measured Q factors of the two types of cantilevers as a function of coating cover percentage; the loss factors Q^{-1} are shown in Fig. 5.11 (b). From these figures we can see that thin film damping is nearly proportionally dependent on the coating coverage percentage. Furthermore,

this linear relationship does not change for both types of cantilevers, even though they have distinct resonance frequencies. Therefore, we can approximate that the coating damping is nearly independent of the resonance frequency within the inspected frequency range.

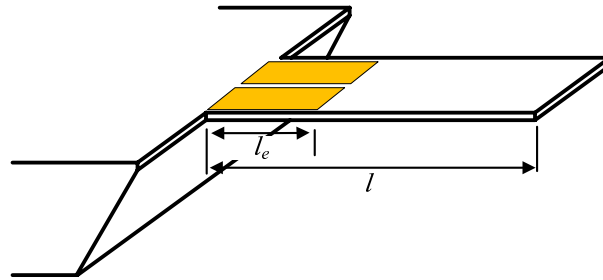


Figure 5.9: Schematic of the cantilever for coating film damping experiment. The piezo-electrode coating films (represented by the yellow parallelograms) are coated on top of the beam, having various lengths l_e with respect to the full cantilever length.

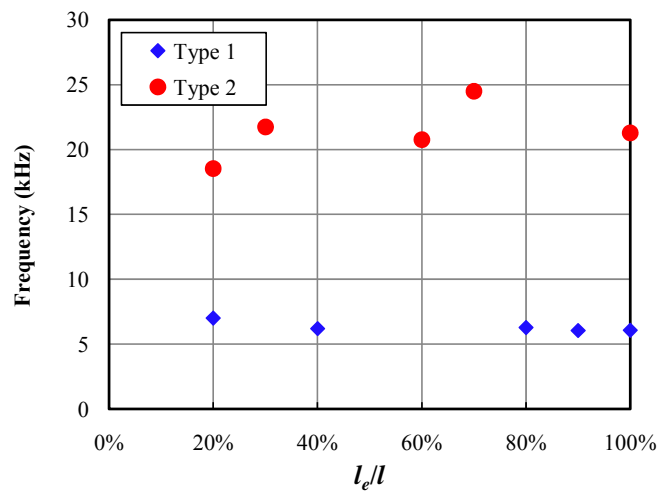


Figure 5.10: Measured resonance frequencies of the cantilevers. The first type of cantilevers has resonance frequencies around 6 kHz, the second type around 20 kHz.

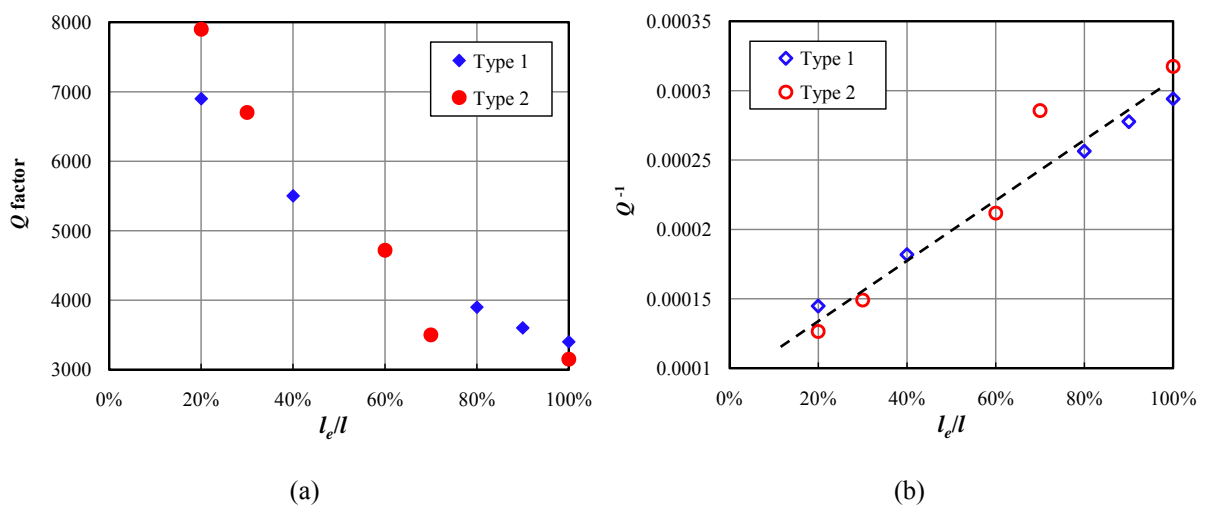


Figure 5.11: Measured (a) Q factors and (b) loss factors Q^{-1} of the cantilevers as a function of coating coverage.

By combining the investigations here and the conclusion from [103], wherein the damping due to thin film coating is found to be proportional to the coating thickness, an expression for the $Q_{coating}$ can be suggested as:

$$Q_{coating} = \frac{t}{t_e} \frac{l}{l_e} \xi_c, \quad (5.5)$$

where t_e is the thickness of the coating film, ξ_c is a constant related to bulk viscoelasticity of the coating layer. This $Q_{coating}$ is thus proportional to the coating thickness and cover percentage. Since it is very difficult to characterize the value of ξ_c , we will choose the best-fit values to minimize the error between the model and the experimental data in the following Section.

5.3.2 Discussion

In this Section, we macroscopically investigated how the coating layer affects the overall damping of the cantilevers. All measurements are from beams vibrating in the fundamental mode. For this investigation we have not included higher modes of vibration, as is often the case in many other studies. The coating film is found to dramatically decrease the Q factor of the cantilevers, and this film damping is nearly linearly dependent on the coating film coverage, irrespective of the resonance frequency.

There are AlN and Au films coated on the beam, in the present work it is difficult to answer how much does each coating film contribute to the overall damping of the cantilever. This issue, however, has been recently addressed in [162] where capacitive-piezoelectric sputtered thin film AlN resonators have been analysed. By separating electrodes from the piezo layer, a large increase in quality factor was measured over similar devices using conventional contacting electrodes. This seems to suggest that sputtered AlN is a high- Q material and that energy loss associated with Au electrodes should be primarily responsible for the low Q s for previous AlN resonators.

5.4 Experimental verification

For a resonator vibrating in vacuum, the dissipation Q^{-1} of the mechanical vibration energy can occur due to TED Q_{TED}^{-1} , anchor loss Q_{anchor}^{-1} , thin coating film loss $Q_{coating}^{-1}$, and others like electric loss in the piezoelectric material and stress loss in the structure material. In most publications it is assumed that the piezoelectric energy loss is small and can be neglected [163]. Therefore we also make a similar assumption. Computing stress loss is prohibitively complicated because a detailed knowledge of the distribution of various crystallographic

defects and their mobility within the substrate is required [164, 165]. However, by using commercially available single crystal silicon, the stress loss caused by the motion of crystallographic defects in silicon is negligible [166]. So we assume for a piezoelectric resonator operating in vacuum, the overall quality factor can be expressed as:

$$Q^{-1} = Q_{TED}^{-1} + Q_{anchor}^{-1} + Q_{coating}^{-1}. \quad (5.6)$$

Each of the components on the right side of eq. (5.6) is quantified using the method described above. In order to demonstrate the validity, their predictions are compared with the experimental data from different cantilevers. The piezo-electrode stack on the resonators used for this comparison covers 20% of the beam length, and the beam thickness was designed to vary from 20 μm to 60 μm . Due to its critical role in estimating the energy losses, the exact thickness of individual cantilevers is calculated by comparing the simulated resonance frequency with measured values.

Tab. 5.2 lists the measured quality factor (Q_{meas}) and analytical quality factors (Q_{analy}) of the fundamental mode of different sizes of cantilevers. The Q_{analy} is the overall quality factor calculated using eq. (5.6). Also listed in Tab. 5.2 are the Q_{TED} , Q_{anchor} and $Q_{coating}$ with ξ_c equals to 400. ξ_c is chosen as the best-fit value to minimize the error between the analytical quality factors and the experimental data. The analytical and measured quality factors are in reasonable agreement as they show quite similar trends. It is not expected that the data fit directly, since the exact modeling is prohibitively complicated and hence much simplified models are used, especially for the thin film coating loss analysis.

Nr.	l (μm)	w (μm)	t (μm)	f_r (kHz)	Q_{TED}	Q_{anchor}	$Q_{coating}$	Q_{analy}	Q_{meas}
<i>C2-I</i>	1540	200	18.8	12.28	30074	52213	9400	6298	5676
<i>C2-II</i>	1540	200	37	21.18	10700	11704	18500	4293	4012
<i>C2-III</i>	1540	200	58	30.99	8101	4612	27500	2655	3024
<i>C6-I</i>	2200	400	22	7.01	56935	55355	11000	7903	6897
<i>C6-II</i>	2200	400	37	10.66	17271	11947	18500	5111	3811
<i>C6-III</i>	2200	400	57.2	15.82	8345	4870	27500	2766	3408

Table 5.2: Comparison between measured Q factors and predicted Q factors of the first flexural mode of different sizes of piezoelectric cantilevers.

Results from both *C2* and *C6* cantilevers reveal that, Q_{TED} and Q_{anchor} are decreasing with increasing beam thickness, and $Q_{coating}$ losses its significant influence when the beam is as

thick as 55 μm . The total quality factors, Q_{meas} and Q_{analy} , show an inverse dependence on the beam thickness. The relationships are also shown in Fig. 5.12 for the cantilevers listed in Tab. 5.2. It can be seen from these two figures that the effect of coating loss $Q_{coating}^{-1}$ is large when the beam is very thin, while anchor loss Q_{anchor}^{-1} and TED Q_{TED}^{-1} become increasingly important when the beam thickness increases.

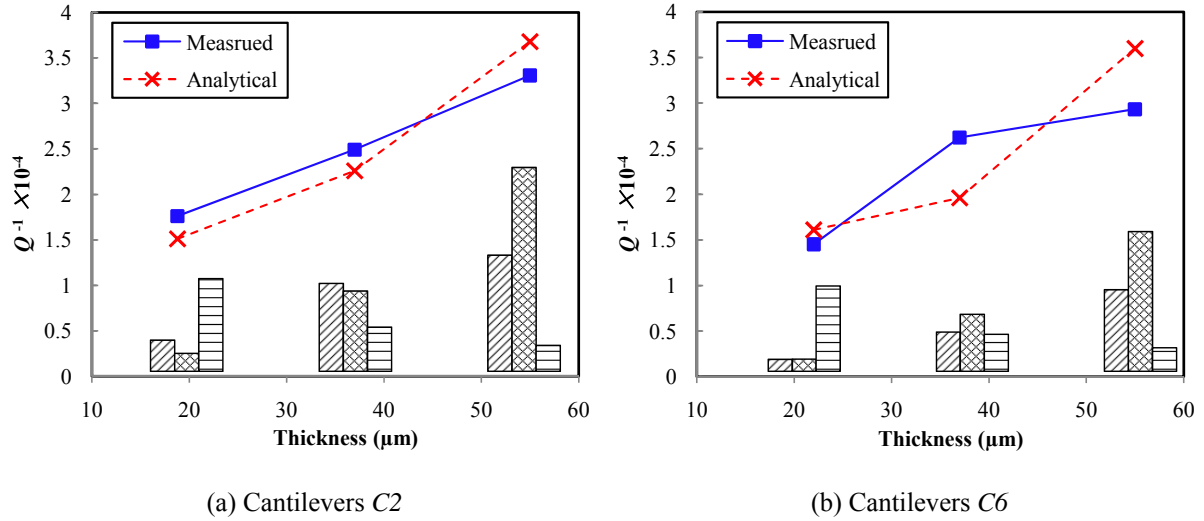


Figure 5.12: Measured total cantilever loss factors Q^{-1} , along with the predicted loss factors due to different damping mechanisms. The diagrams show the contributions from each damping mechanism, ▨ represents Q^{-1} due to TED, ⊠ represents Q^{-1} due to anchor loss, and ▤ represents Q^{-1} due to coating loss.

The comparison between the Q_{meas} and Q_{analy} of the first lateral mode of different sizes of cantilevers is shown in Tab. 5.3. It is found that $\xi_c = 160$ works well for the cantilevers. As expected, the value of ξ_c for lateral vibrating cantilever is smaller than that of a flexural vibrating resonator, since the coating film is much more deformed for the lateral mode.

Nr.	l (μm)	w (μm)	t (μm)	f_r (kHz)	Q_{TED}	Q_{anchor}	$Q_{coating}$	Q_{analy}	Q_{meas}
C1	1200	200	18.4	169.53	156240	4986	3680	2089	1886
C3	2200	200	17.7	53.68	73854	8218	3540	2394	2760
C6-I	2200	400	22	95.55	302632	2351	4400	1525	1332

Table 5.3: Comparison between measured Q factors and predicted Q factors of the first lateral mode of different sizes of piezoelectric cantilevers.

5.5 Conclusion

The goal of this Chapter is to survey the intrinsic energy dissipation characteristic of piezoelectric micro resonators. Three damping effects, TED, anchor losses and coating losses, were found to play an important role in the overall intrinsic damping of the resonators.

Parametric studies have been performed to gain a better understanding of the factors, e.g. resonator beam geometry, resonance mode, support structure and piezo-electrode thin film coating, that influence the energy dissipation for a micro resonator.

The presented analysis has been applied to real fabricated piezoelectric micro cantilevers. A monotonic reduction in Q with increasing thickness was observed for the cantilevers. Coating loss was found to be significant for very thin cantilevers, whereas TED and anchor loss was found to increase with increasing beam thicknesses. The experiments described in this Chapter provide a validation of the models for intrinsic damping in piezoelectric micro resonators, and the comparison of predictions from these models with measurements indicates that intrinsic damping can be reduced by a careful design of the cantilever geometry.

It is clear that further experiments should be carried out. For example, Q measurements over a broader set of cantilever thicknesses need to be performed to more firmly establish the thickness dependence. The minimum piezo-electrode stack coverage among the cantilevers in this work is 20%. This percentage can be reduced further, even to zero, if other excitation and detection methods could be involved, in order to further explore the coating film pattern effect on coating loss. Also more complex-shaped resonators are of great interest since recent research studies indicate the possibility of designing high Q resonators limited only by anchor loss or TED [167-169].

6. Conclusion and outlook

6.1 Conclusion

In this work, vibrating piezoelectric micro resonators of different geometries have been developed to study the energy dissipation mechanisms. The resonators were tested with eight different gases in a custom-built vacuum chamber, where the pressure can be controlled precisely from atmospheric pressure down to high vacuum. The aim was to systematically evaluate and compare the effects of ambient pressure, the nature of the surrounding gas, the resonator geometry, higher mode operation and the presence of a nearby surface on the resonance behavior. We have developed experimental, computational and analytical tools to analyze the dynamics of piezoelectric micro resonator in gases as well as in high vacuum. Specifically, the contribution of this thesis can be categorized in the following areas:

Device design, fabrication and packaging

Piezoelectric resonators were used in this research due to their advantages with respect to self-excitation and self-sensing, a low driving voltage and full integration. AlN was selected as the active piezoelectric material due to its excellent piezoelectric and mechanical properties. The AlN based piezoelectric resonators were fabricated using conventional microsystem technologies. In our design, the highly p-doped single crystal silicon formed the resonator and simultaneously served as bottom electrode for the piezoelectric layer. The elimination of a bottom metal electrode reduced the number of stacked layers and stress in the resonator, simplified the fabrication process and reduced the intrinsic energy loss in the structure.

Three sets of principal resonator configurations, namely cantilevers, bridges and plates, were designed and fabricated with different geometric dimensions. Two resonator packaging methods were used in this work, to investigate the dynamics of resonators vibrating in unbounded fluids or close to a surface. For the first case, the resonator chip was die-mounted on a PCB board, with a hole pre-drilled on the board at the area where the resonator beam would be located. For the second case, a top cover with different cavity heights was clamped on the top side of the resonators. This packaging technology allowed a flexibility for combining different resonator structures with varying squeeze film gaps.

All-electrical excitation and detection

An all-electrical excitation and detection method has been developed. The effect of the input-output electrical crosstalk in the resonator was found to be significant, the crosstalk made the mechanical resonance less pronounced and the characterization of the resonance behavior

more difficult. Two crosstalk compensation schemes were developed using a bridge resonator as example. The first scheme was based on an additional on-chip compensation electrode and could be more efficient for mass production, while the second applied a compensation voltage to the silicon bottom electrode and was more flexible with respect to individual precise adjustment. At the laboratory stage we were presently in, the latter method was used with individual calibration for each resonator.

Experimental details

The resonators were tested in a number of gases under pressures varying from 10^{-4} – 10^3 mbar. Five noble gases (He, Ne, Ar, Kr and Xe), as well as N_2 , CO_2 and SF_6 were used to observe the resonance variation. These eight gases covered a relatively broad spectrum of different properties and did not cause any safety problems. To investigate the energy losses in a practically unbounded fluid, up to seven higher vibration modes were recorded in addition to the fundamental flexural resonance mode. For the case of vibrations in a bounded volume of fluid, experiments with beam/surface separation of 20, 50, 100, 150, 200, 250 and 300 μm were carried out by using a 400 μm wide bridge resonator. This allowed a big range of separations, from much smaller than the resonator width up to the same order of magnitude.

Hydrodynamic loading on micro resonators

For resonators vibrating in a continuous fluid, the most extensive type of model clearly must be based on a solution of the full set of Navier-Stokes equations. The full set of equations was semi-analytically solved using the Boundary Element Method. The solution was interpreted by the “three wave theory” coupling viscous, thermal and acoustic waves. Furthermore, the commercial FEM package COMSOL Multiphysics has been used to solve and simulate the full model equations. The comparison of measured quality factors from a plate resonator and COMSOL simulation confirmed the accuracy of the full model and COMSOL predictions. This simulation model could be used to predict the hydrodynamic loading of resonators with any geometry in viscous fluids. However, this method does have some disadvantages, such as being computationally costly, relying on sophisticated numerical techniques, and being non-intuitive with respect to understand the results physically.

For a lot of applications, the resonator structures are beam-shaped. The beam-shaped resonators vibrating in unbounded fluids have been investigated, by measuring micro cantilevers in different gases and explaining the results using simplified sphere string and cylinder models based on the incompressible Navier-Stokes equation. The investigation was focused on vibrations of the flexural and torsional modes in the viscous regime; the analytical

predictions were in reasonable agreements with the measurement results. Besides, measurements with different gases showed that the compressibility of gases leads to additional damping when the resonator is vibrating in a higher mode, whereas in most cases the gases can be assumed to be incompressible. The compressible gas damping was modeled using the acoustic wave equation, and the calculated results showed a qualitative agreement with higher mode measurements.

The case of resonators vibrating close to a surface was also investigated. Experiments were performed using a bridge resonator with a big range of beam/surface separations. Different theoretical models were used to assist the analysis. The traditional squeeze film model could predict the gas damping when the ratio of the resonator width to gap height w/h_0 was bigger than 10, this model could account the gas rarefaction effect in the gap by using an “effective viscosity” concept. The extended squeeze film model was valid for $w/h_0 \geq 4$. The semi-analytical solution from the unsteady Navier-Stokes model could be used when the gap height was bigger. However, these models failed to predict gas damping effect in low pressure at large separations; the effect was interpreted by a newly developed thermo-mechanical resonance model, which transferred the calculation of thermoelastic damping in solids to the dynamic damping in gases in the transition pressure regime. The variation of quality factors at higher resonant mode was also measured, and the results could be qualitatively explained in terms of the boundary layer surrounding the micro resonator.

Intrinsic damping in vibrating piezoelectric micro resonators

When a resonator is operated in high vacuum, the energy dissipation inside the materials of the resonator dominates the quality factor. Three intrinsic damping effects, called TED, anchor losses and coating losses, were found to play important roles in piezoelectric micro resonators. Since the different damping mechanisms were mixed with each other, it was difficult to separate the contribution of individual mechanisms experimentally. TED and anchor losses were investigated by using a combination of both analytical and numerical methods, while the coating loss mechanism was explored by measuring a series of cantilevers with a piezo-electrode stack coverage ranging from 20% to 100% of the beam length. Finally, experimental validations were conducted on different structures of piezoelectric micro cantilevers, showing that the analysis yielded qualitative matches with measurements.

6.2 Outlook

Research is an ongoing effort, and due to time constraints some additional avenues of research could not be explored. However, disregarding these constraints we will outline possible directions for future work.

Electrical crosstalk in the resonators is mainly induced from the short circuit connection between drive and sense port silicon grounds. An electrical compensation method was used in the work; however the compensation quality reduces as the frequency increases. Another approach to reduce the crosstalk can be employed by using two separated metal ground electrodes. This could be more suitable for high frequency applications.

For micro resonators vibrating in an unbounded fluid, there is still a need to improve the existing theories of describing gas damping in the non-continuum regime. Carefully planned experiments should be performed, to help us better understand the evolution of the physics when going from full continuum flow to transition flow and then molecular flow.

For micro resonators vibrating close to a surface with moderate distance, the thermo-mechanical resonance model is a promising approach that describes the quality factor performance in the transition regime. However, it requires several fitting parameters such as the root component ε_{dyn} and the factor ξ_{dyn} . This is mainly due to a lack of knowledge of the pressure dependent thermal diffusivity of the gas. It is important to clarify this dependence in the future.

Further measurements on new resonators should be carried out to explore each intrinsic damping mechanism experimentally. For example, Q measurements over a broader set of resonator beam thicknesses need to be performed to more firmly establish the thickness dependence. The minimum piezo-electrode stack coverage among the cantilevers is 20%, this percentage can be reduced even to zero if other excitation and detection methods could be involved. Also, complex-shaped resonators are of great interest, since recent research studies [167-169] indicate the possibility of designing high Q resonators limited only by anchor loss or TED.

Throughout this thesis we have shown that there is a vast body of ongoing research in this field, a field that is continually changing. There are still many questions that need to be answered and many avenues of research that must be explored. The research reported in this dissertation represents an attempt to answer some of these questions.

References

- [1] P. S. Waggoner and H. G. Craighead: Micro- and nanomechanical sensors for environmental, chemical, and biological detection, *Lap Chip*, **7**, 1238-1255, 2007.
- [2] R. Ruby: Review and comparison of bulk acoustic wave FBAR, SMR technology, *Proc. IEEE Ultrasonic Symposium*, 1029-1040, 2007.
- [3] P. M. Martin, M. S. Good, J. W. Johnston, G. J. Posakony, L. J. Bond and S. L. Crawford: Piezoelectric films for 100-Mhz ultrasonic transducers, *Thin Solid Films*, **379**, 253-258, 2000.
- [4] A. M. Madni, L. E. Costlow and S. J. Knowles: Common design techniques for BEI GyroChip quartz rate sensors for both automotive and aerospace/defense markets, *Sensors J. IEEE*, **3**, 569-578, 2003.
- [5] S. P. Beeby, J. N. Ross and N. M. White: Design and fabrication of a micromachined silicon accelerometer with thick-film printed PZT sensor, *J. Micromech. Microeng.*, **10**, 322-328, 2000.
- [6] P. J. Stephanou, G. Piazza, C. D. White, M. B. J. Wijesundara and A. P. Pisano: Piezoelectric aluminum nitride MEMS annular dual contour mode filters, *Sens. Actuators A*, **134**, 152-160, 2007.
- [7] S. B. Horowitz, M. Sheplak, L. N. Cattafesta and T. Nishida: A MEMS acoustic energy harvester, *J. Micromech. Microeng.*, **16**, 174-181, 2006.
- [8] Ü. Sökmen, A. Stranz, A. Waag, A. Ababneh, H. Seidel, U. Schmid and E. Peiner: Evaluation of resonating Si cantilevers sputter-deposited with AlN piezoelectric thin films for mass sensing applications, *J. Micromech. Microeng.*, **20**, 064007, 2010.
- [9] C. Ayela and L. Nicu: Micromachined piezoelectric membranes with high nominal quality factors in Newtonian fluid media: a lamb's model validation at the microscale, *Sens. Actuators B*, **123**, 860-868, 2007.
- [10] D. James, S. M. Scott, Z. Ali and W. T. O'Hare: Chemical sensors for electronic nose systems, *Microchim Acta*, **149**, 1-17, 2005.
- [11] A. E. Hoyt, A. J. Ricco, J. W. Bartholomew and G. C. Osbourn: SAW sensors for the room-temperature measurement of CO₂ and relative humidity, *Anal. Chem.*, **70**, 2137-2145, 1998.
- [12] L. Fadel, F. Lochon, I. Dufour and O. Français: Chemical sensing: millimeter size resonant microcantilever performance, *J. Micromech. Microeng.*, **14**, S23, 2004.
- [13] S. J. Kim, T. Ono and M. Esashi: Study on the noise of silicon capacitive resonant

- mass sensors in ambient atmosphere, *J. Appl. Phys.*, **102**, 104304, 2007.
- [14] X. Xia, Z. Zhang and X. Li: A Latin-cross-shaped integrated resonant cantilever with second torsion-mode resonance for ultra-resoluble bio-mass sensing, *J. Micromech. Microeng.*, **18**, 035028, 2008.
- [15] J. Zhou, P. Li, S. Zhang, Y. Huang, P. Yang, M. Bao and G. Ruan: Self-excited piezoelectric microcantilever for gas detection, *Microelectron. Eng.*, **69**, 37-46, 2003.
- [16] A. Ababneh, U. Schmid, J. Hernando, J. L. Sánchez-Rojas and H. Seidel: The influence of sputter deposition parameters on piezoelectric and mechanical properties of AlN thin films, *Mater. Sci. Eng. B*, **172**, 253-258, 2010.
- [17] H. C. Qiu, P. Schwarz, D. Feili, X. Z. Wu and H. Seidel: Performance modeling and characterization of AlN resonator, *Proc. Microsystemtechnik Kongress*, 803-806, 2011.
- [18] H. C. Qiu, P. Schwarz, D. Feili, S. Merzsh, E. Peiner, X. Z. Wu and H. Seidel: Electrical performance analysis and characterization of two port piezoelectric resonators, *Microsyst. Technol.*, **19**, 1131-1136, 2013.
- [19] H. C. Qiu, P. Schwarz, H. Völlm, D. Feili, X. Z. Wu and H. Seidel: Electrical crosstalk in two-port piezoelectric resonators and compensation solutions, *J. Micromech. Microeng.*, **23**, 045007, 2013.
- [20] M. Elwenspoek, F. R. Blom, S. Bouwstra, T. S. J. Lammering, F. C. M. van de Pol, H. A. C. Tilmans, Th. J. A. Popma and J. H. J. Fluitman: Transduction mechanisms and their applications in micromechanical devices, *Proc. IEEE MEMS*, 126-132, 1989.
- [21] G. Stemme: Resonant silicon sensors, *J. Micromech. Microeng.*, **1**, 113-125, 1991.
- [22] A. M. Madni and L. A. Wan: Microelectromechanical systems (MEMS): An overview of current state-of-the-art, *Proc. IEEE Aerospace Conference*, 421-427, 1998.
- [23] L. A. Beardslee, A. M. Addous, S. Heinrich, F. Josse, I. Dufour and O. Brand: Thermal excitation and piezoresistive detection of cantilever in-plane resonance modes for sensing applications, *J. Microelectromech. Syst.*, **19**, 1015-1017, 2010.
- [24] T. Mattila, J. Kiihamaki, T. Lamminmaki, O. Jaakkola, P. Rantakari, A. Oja H. Seppä, H. Kattelus and I. Tittonen: A 12 MHz micromechanical bulk acoustic mode oscillator, *Sens. Actuators A*, **101**, 1-9, 2002.
- [25] S. Pourkanali, G. K. Ho and F. Ayazi: Vertical capacitive SiBARs, *Proc. IEEE*

- MEMS*, 211-214, 2005.
- [26] A. Jaakkola, P. Rosenberg, S. Asmala, A. Nurmela, T. Pensala, T. Riekkinen, J. Dekker, T. Mattila, A. Alastalo, O. Holmgren and K. Kokkonen: Piezoelectrically transduced single-crystal-silicon plate resonators, *Proc. IEEE Ultrasonic Symposium*, 717-720, 2008.
- [27] P. Rosenberg, A. Jaakkola, J. Dekker, A. Nurmela, T. Pensala, S. Asmala, T. Riekkinen, T. Mattila, and A. Alastalo: Piezoelectrically actuated micromechanical BAW resonators, *Proc. IEEE Ultrasonic Symposium*, 2181-2184, 2008.
- [28] G. Piazza, P. J. Stephanou and A. P. Pisano: Piezoelectric aluminum nitride vibrating contour-mode MEMS resonators, *J. Microelectromech. Syst.*, **15**, 1406-1418, 2006.
- [29] C. T. C. Nguyen: Microelectromechanical components for miniaturized low power communications, *Proc. IEEE Int. Microwave Symposium*, 48-77, 1999.
- [30] B. P. Otis and J. M. Rabaey: A 300- μ W 1.9-GHz CMOS oscillator utilizing micromachined resonators, *J. Solid-State Circuits*, **38**, 1271-1274, 2003.
- [31] R. E. Mihailovich and N. C. MacDonald: Dissipation measurements of vacuum operated single-crystal silicon microresonators, *Sens. Actuators A*, **50**, 199-207, 1995.
- [32] R. Lucklum, C. Behling, R. W. Cernosek and S. J. Martin: Determination of complex shear modulus with thickness shear mode resonators, *J. Phys. D*, **30**, 346-356, 1997.
- [33] A. N. Cleland and M. L. Roukes: Fabrication of high frequency nanometer scale mechanical resonators from bulk Si crystals, *Appl. Phys. Lett.*, **69**, 2653-2655, 1996.
- [34] S. Kim, K. D. Kihm and T. Thundat: Fluidic applications for atomic force microscopy (AFM) with microcantilever sensors, *Exp. Fluids*, **48**, 721-736, 2010.
- [35] B. N. Johnson and R. Mutharasan: Biosensing using dynamic-mode cantilever sensors: A review, *Biosensors and Bioelectronics*, **32**, 1-18, 2012.
- [36] P. L. Gatti: Applied structural and mechanical vibrations: Theory, methods and measuring instrumentation, CRC Press, New York, 1999.
- [37] B. N. Johnson and R. Mutharasan: Dependence of the quality factor of micromachined silicon beam resonators on pressure and geometry, *J. Vac. Sci. Technol. B*, **10**, 19-26, 1992.
- [38] G. K. Batchelor: Fluid dynamics, Cambridge University Press, Cambridge, 1974.

- [39] M. Bruneau, P. H. Herzog, J. Kergomard and J. D. Polack: General formulation of dispersion equation in bounded visco-thermal fluid, and application to simple geometries, *Wave Motion*, **11**, 441-451, 1989.
- [40] W. M. Beltman: Viscothermal wave propagation including acousto-elastic interaction, part I. Theory, *J. Sound Vib.*, **227**, 555-586, 1999.
- [41] W. M. Beltman: Viscothermal wave propagation including acousto-elastic interaction, part II. Applications, *J. Sound Vib.*, **227**, 587-609, 1999.
- [42] C. Karra and M. Ben Tahar: An intergral equation formulation for boundary element analysis of propagation in viscothermal fluids, *J. Acoust. Soc. Am.*, **102**, 1311-1318, 1997.
- [43] H. C. Qiu, P. Schwarz, D. Feili, X. Z. Wu and H. Seidel: Viscothermal acoustic waves in micro scale resonators, *Proc. Transducers*, 1719-1722, 2013.
- [44] J. H. Lee, S. T. Lee, C. M. Yao and W. Fang: Comments on the size effect on the microcantilever quality factor in free air space, *J. Micromech. Microeng.*, **17**, 139-146, 2007.
- [45] S. Basak and A. Raman: Hydrodynamic loading of microcantilevers vibrating in viscous fluids, *J. Appl. Phys.*, **99**, 114906, 2006.
- [46] COMSOL Multiphysics 4.3b manual.
- [47] K. Kokubun, M. Hirata, H. Murakami, Y. Toda and M. Ono: A bending and stretching mode crystal oscillator as a friction vacuum gauge, *Vacuum*, **34**, 731-735, 1984.
- [48] K. Kokubun, M. Hirata, M. Ono, H. Murakami and Y. Toda: Frequency dependence of a quartz oscillator on gas pressure, *J. Vac. Sci. Technol. A*, **34**, 2184-2187, 1985.
- [49] H. Hosaka, K. Itao and S. Kuroda: Evaluation of energy dissipation mechanisms in vibrational microactuators, *Proc. IEEE Workshop on MEMS'94*, 193-198, 1994.
- [50] H. Hosaka, K. Itao and S. Kuroda: Damping characteristics of beam shaped micro oscillators, *Sens. Actuators A*, **49**, 87-95, 1995.
- [51] L. D. Landau and E. M. Lifshitz: Fluid Mechanics, 2nd edition, Pergamon Press, Oxford, 2004.
- [52] S. Kirstein, M. Mertesdorf and M. Schönhoff: The influence of a viscous fluid on the vibration dynamics of scanning near-field optical microscopy fiber probes and atomic force microscopy cantilevers, *J. Appl. Phys.*, **84**, 1782-1790, 1998.
- [53] J. E. Sader: Frequency response of cantilever beams immersed in viscous fluids

- with applications to the atomic force microscope, *J. Appl. Phys.*, **84**, 64-76, 1998.
- [54] E. O. Tuck: Calculation of unsteady flows due to small motions of cylinders in viscous fluid, *J. Eng. Math.*, **3**, 29-44, 1969.
- [55] C. A. Van Eysden and J. E. Sader: Frequency response of cantilever beams immersed in viscous fluids with applications to the atomic force microscope: Arbitrary mode order, *J. Appl. Phys.*, **101**, 044908, 2007.
- [56] F. R. Blom, S. Bouwstra, M. Elwenspoek and J. H. J. Fluitman: Dependence of the Q factor of micro-machined silicon beam resonators on pressure and geometry, *J. Vac. Sci. Technol.*, **10**, 19-26, 1992.
- [57] K. Naeli and O. Brand: Dimensional considerations in achieving large quality factors for resonant silicon cantilevers in air, *J. Appl. Phys.*, **105**, 014908, 2009.
- [58] X. Xia and X. Li: Resonance-mode effect on microcantilever mass-sensing performance in air, *Rev. Sci. Instrum.*, **79**, 074301, 2008.
- [59] J. Lu, T. Ikehara, Y. Zhang, T. Mihara, T. Itoh and R. Maeda: High quality factor silicon cantilever driven by piezoelectric thin film actuator for resonant based mass detection, *Microsyst. Technol.*, **15**, 1163-1169, 2009.
- [60] S. Dohn, R. Sandberg, W. Svendsen and A. Boisen: Enhanced functionality of cantilever based mass sensors using higher modes, *Appl. Phys. Lett.*, **86**, 233501, 2005.
- [61] C. A. Van Eysden and J. E. Sader: Frequency response of cantilever beams immersed in compressible fluids with applications to the atomic force microscope, *J. Appl. Phys.*, **106**, 094904, 2009.
- [62] C. A. Van Eysden and J. E. Sader: Compressible viscous flows generated by oscillating flexible cylinders, *Phys. Fluids*, **21**, 013104, 2009.
- [63] B. Weiss, E. K. Reichel and B. Jakoby: Modeling of a clamped-clamped beam vibrating in a fluid for viscosity and density sensing regarding compressibility, *Sens. Actuators A*, **143**, 293-301, 2008.
- [64] J. Jensen and M. Hergner: Predictions of the compressible fluid model and its comparison to experimental measurements of Q factors and flexural resonance frequencies for microcantilevers, *J. Sensors*, **2012**, 258381, 2012.
- [65] E. Newell: Miniaturization of tuning forks, *Science*, **161**, 1320-1326, 1968.
- [66] W. E. Langlois: Isothermal squeeze films, *Quart. Appl. Math.*, **XX(2)**, 131-150, 1962.
- [67] J. J. Blech: On isothermal squeeze film, *ASME J. Lubric. Technol.*, **105**, 615-620,

- 1983.
- [68] W. S. Griffin, H. H. Richardson and S. Yamanami: A study of squeeze film damping, *ASME J. Basic Eng.*, **88**, 451-456, 1966.
- [69] M. Bao and H. Yang: Squeeze film air damping in MEMS, *Sens. Actuators A*, **136**, 3-27, 2007.
- [70] M. Andrews, I. Harres and G. Turner: A comparison of squeeze-film theory with measurements using a microstructure, *Sens. Actuators A*, **36**, 79-87, 1993.
- [71] T. Veijola: Compact models for squeezed-film dampers with inertial and rarefied gas effects, *J. Micromech. Microeng.*, **14**, 1109-1118, 2004.
- [72] P. Schwarz, D. Feili and H. Seidel: Squeeze Film Effect Based Micro Sensor for Vacuum Pressure Measurement, *Proc. Smart Systems Integration*, 87-90; 2010.
- [73] P. Schwarz, D. Feili, R. Engel, N. Pagel and H. Seidel: Vacuum pressure and gas detection with a silicon based micromechanical squeeze film sensor, *Proc. Eurosensors XXIV*, 750-753, 2010.
- [74] T. Naik, E. K. Longmire and S. C. Mantell: Dynamic response of a cantilever in liquid near a solid wall, *Sens. Actuators A*, **102**, 240-254, 2003.
- [75] C. Harrison, E. Tavernier, O. Vancauwenberghe, E. Donzier, K. Hsu, A. R. H. Goowin, F. Marty and B. Meicier: On the response of a resonating plate in a liquid near a solid wall, *Sens. Actuators A*, **134**, 414-426, 2007.
- [76] A. Fornari, M. Sullivan, H. Chen, C. Harrison, K. Hsu, F. Marty and B. Mercier: Experimental observation of inertia-dominated squeeze film damping in liquid, *J. Fluids Eng.*, **132**, 121201, 2010.
- [77] T. Veijola, A. Pursula and P. Raback: Extending the validity of existing squeeze-film damper models with elongations of surface dimensions, *Proc. Nanotech 2004*, 235-238, 2004.
- [78] T. Veijola, A. Pursula and P. Raback: Extending the validity of squeeze-film damper models with elongations of surface dimensions, *J. Micromech. Microeng.*, **15**, 1624-1636, 2005.
- [79] C. P. Green and J. E. Sader: Frequency response of cantilever beams immersed in viscous fluids near a solid surface with applications to the atomic force microscope, *J. Appl. Phys.*, **98**, 114916, 2005.
- [80] C. P. Green and J. E. Sader: Small amplitude oscillations of a thin beam immersed in a viscous fluid near a solid surface, *Phys. Fluids*, **17**, 073102, 2005.
- [81] R. C. Tung, A. Jana and A. Raman: Hydrodynamic loading of microcantilevers

- oscillating near rigid walls, *J. Appl. Phys.*, **104**, 114905, 2008.
- [82] P. Schwarz: Untersuchung der gasart- und spaltabhängigen Dämpfungseigenschaften mikromechanischer Resonatoren von der Molekular- bis zur Kontinuumsströmung (in German), Ph.D. thesis, Saarland University, 2014.
- [83] C. Zener: Internal friction in solids: I. Theory of internal friction in reeds, *Phys. Rev.*, **52**, 230-235, 1937.
- [84] C. Zener: Internal friction in solids: II. General theory of thermoelastic internal friction, *Phys. Rev.*, **53**, 90-99, 1937.
- [85] R. Lifshitz and M. L. Roukes: Thermoelastic damping in micro- and nanomechanical systems, *Phys. Rev. B*, **61**, 5600-5609, 2000.
- [86] R. N. Candler, A. Duwel, M. Varghese, S. A. Chandorkar, M. A. Hopcroft, P. Woo-Tae, K. Bongsang, G. Yama, A. Partridge, M. Lutz and T. W. Kenny: Impact of geometry on thermoelastic dissipation in micromechanical resonant beams, *J. Microelectromech. Syst.*, **15**, 927-934, 2006.
- [87] R. Abdolvand, H. Johari, G. K. Ho, A. Erbil and F. Ayazi: Quality factor in trench-refilled polysilicon beam resonators, *J. Microelectromech. Syst.*, **15**, 471-478, 2006.
- [88] S. J. Wong, C. H. J. Fox and S. McWilliam: Thermoelastic damping of the in-plane vibration of thin silicon rings, *J. Sound Vib.*, **293**, 266-285, 2006.
- [89] S. K. De and N. R. Aluru: Theory of thermoelastic damping in electrostatically actuated microstructures, *Phys. Rev. B*, **74**, 144305, 2006.
- [90] B. Antkowiak, J. P. Gorman, M. Varghese, D. J. D. Carter, A. Duwel: Design of a high Q low impedance GHz-range piezoelectric resonator, *Proc. Transducers*, 841-846, 2003.
- [91] J. Gorman: Finite element model of thermoelastic damping in MEMS, Master of science thesis, Massachusetts Institute of Technology, 2002.
- [92] A. Duwel, R. N. Candler, T. W. Kenny and M. Varghese: Engineering MEMS resonators with low thermoelastic damping, *J. Microelectromech. Syst.*, **15**, 1437-1445, 2006.
- [93] Y. Jimbo and K. Ito: Energy loss of a cantilever vibrator. *J. Horolog. Inst. Jpn.*, **47**, 1-15, 1968 (In Japanese).
- [94] Z. Hao, A. Erbil and F. Ayazi: An analytical model for support loss in micromachined beam resonators with in-plane flexural vibrations, *Sens. Actuators A*, **109**, 156-164, 2003.

- [95] Y. H. Park and K. C. Park: High-fidelity modeling of MEMS resonators – Part I: Anchor loss mechanisms through substrate, *J. Microelectromech. Syst.*, **13**(2), 238-247, 2004.
- [96] Y. H. Park and K. C. Park: High-fidelity modeling of MEMS resonators – Part II: Coupled beam-substrate dynamics and validation, *J. Microelectromech. Syst.*, **13**(2), 248-257, 2004.
- [97] D. M. Photiadis and J. A. Judge: Attachment losses of high Q oscillators, *Appl. Phys. Lett.*, **85**, 482-484, 2004.
- [98] J. A. Judge, D. M. Photiadis, J. F. Vignola, B. H. Houston and J. Jarzynski: Attachment loss of micromechanical and nanomechanical resonators in the limits of thick and thin support structures, *J. Appl. Phys.*, **101**, 013521, 2007.
- [99] D. S. Bindel and S. Govindjee: Elastic PMLs for resonators anchor loss simulation. *Int. J. Numer. Meth. Eng.*, **64**(6), 789-818, 2005.
- [100] D. S. Bindel: HiQLab, available from at <http://www.cims.nyu.edu/~dbindel/> (accessed date January 2014).
- [101] J. Lysmer and R. L. Kuhlemeyer: Finite dynamic model for infinite media, *J. Eng. Mechanics Division*, 859-877, 1969.
- [102] G. Meyer and N. M. Amer: Novel optical approach to atomic force microscopy, *Appl. Phys. Lett.*, **53**, 1045-1047, 1988.
- [103] R. Sandberg, K. Møhlhave, A. Boisen and W. Svendsen: Effect of gold coating on the Q factor of a resonant cantilever, *J. Micromech. Microeng.*, **15**, 2249-2253, 2005.
- [104] L. Sekaric, D. W. Carr, S. Evoy, J. W. Parpia and H. G. Craighead: Nanomechanical resonant structures in silicon nitride: fabrication, operation and dissipation issues, *Sens. Actuators A*, **101**, 215-219, 2002.
- [105] J. Hernando, J. L. Sánchez-Rojas, S. González-Castilla, E. Iborra, A. Ababneh and U. Schmid: Simulation and laser vibrometry characterization of piezoelectric AlN thin films, *J. Appl. Phys.*, **104**, 053502, 2008.
- [106] P. Muralt: Ferroelectric thin films for micro-sensors and actuators: a review, *J. Micromech. Microeng.*, **10**, 136-146, 2000.
- [107] M. J. Vellekoop, C. C. O. Visser, P. M. Sarro and A. Venema: Compatibility of zinc oxide with silicon IC processing, *Sens. Actuators A*, **23**, 1027-1030, 1990.
- [108] R. S. Naik, R. Reif, J. J. Lutsky and C. G. Sodini: Low-temperature deposition of highly textured aluminum nitride by direct current magnetron sputtering for

- applications in thin-film resonators, *J. Electrochem. Soc.*, **146**, 691-696, 1999.
- [109] A. Ababneh, K. Kreher and U. Schmid: Etching behaviour of sputter-deposited aluminium nitride thin films in H₃PO₄ and KOH solutions, *Microsyst. Technol.*, **14**, 567-573, 2008.
- [110] G. Pizza and A. P. Pisano: Two-port stacked piezoelectric aluminum nitride contour-mode resonant MEMS, *Sens. Actuators A*, **136**, 638-645, 2007.
- [111] C. J. van Mullem, H. A. C. Tilmans, A. J. Mouthaan and J. H. J. Fluitman: Electrical cross-talk in two-port resonator - the resonant silicon beam force sensor, *Sens. Actuators A*, **31**, 168-173, 1992.
- [112] C. Zuo, N. Sinha, C. R. Perez, R. Mahameed, M. B. Pisani and G. Piazza: Hybrid ultra-compact 4th order band-pass filters based on piezoelectric AlN contour-mode MEMS resonators, *Solid-state Sensors and Microsystems Workshop*, 324-327, 2008.
- [113] M.S. Weinberg, R.N. Candler, S.A Chandorkar, J.S. Varsanik, T.W. Kenny and A.E. Duwel: Energy loss in MEMS resonators and the impact on inertial and RF devices, *Proc. Transducers*, 688-695, 2009.
- [114] V. Cimalla, F. Niebelschütz, K. Tonish, Ch. Foerster, K. Breckner, I. Cimalla, T. Friedrich, J. Pezoldt, R. Stephan, M. Hein and O. Ambacher: Nanoelectromechanical devices for sensing applications, *Sens. Actuators B*, **126**, 24-34, 2007.
- [115] J. Mertens, E. Finot, T. Thundat, A. Fabre, M. H. Nadal, V. Eyraud and E. Bourillot: Effects of temperature and pressure on microcantilever resonance response, *Ultramicroscopy*, **97**, 119-126, 2003.
- [116] R. G. Christian: The theory of oscillating-vane vacuum gauges, *Vacuum*, **16**, 175-178, 1966.
- [117] S. Bianco, M. Cocuzza, S. Ferrero, E. Giuri, G. Piacenza, C. F. Pirro, A. Ricci, L. Scaltrito, D. Bich, A. Merialdo, P. Schina and R. Correale: Silicon resonant microcantilevers for absolute pressure measurement, *J. Vac. Sci. Technol. B*, **24**, 1803-1809, 2006.
- [118] G. A. Bird: *Molecular gas dynamics and the direct simulation of gas flows*, Clarendon Press, Oxford, 1994.
- [119] R. W. Barber and D. R. Emerson: Challenges in modeling gas-phase flow in microchannels: from slip to transition, *Heat Transfer Engineering*, **27**, 3-12, 2006.
- [120] R. K. Agarwal, K. Y. Yun and R. Balakrishnan: Beyond Navier-Stokes: Burnett

- equations for flows in the continuum-transition regime, *Phys. Fluids*, **13**, 3061-3085, 2001.
- [121] S. Chapman and T. G. Cowling: The mathematical theory of non-uniform gases, 3rd ed., Cambridge University Press, Cambridge, 1970.
- [122] V. Yakhot and C. Colosqui: Stokes' second flow problem in a high-frequency limit: application to nanomechanical resonators, *J. Fluid Mech.*, **586**, 249-258, 2007.
- [123] D. M. Karabacak, V. Yakhot and K. L. Ekinici: High-frequency nanofluidics: an experimental study using nanomechanical resonators, *Phys. Rev. Lett.*, **98**, 254505, 2007.
- [124] K. L. Ekinici, D. M. Karabacak and V. Yakhot: Universality in oscillating flows, *Phys. Rev. Lett.*, **101**, 264501, 2008.
- [125] K. L. Ekinici, V. Yakhot, S. Rajauria, C. Colosqui and D. M. Karabacak: High-frequency nanofluidics: a universal formulation of the fluid dynamics of MEMS and NEMS, *Lab Chip*, **10**, 3013-3025, 2010.
- [126] C. Lissandrello, V. Yakhot and K. L. Ekinici: Crossover from hydrodynamics to the kinetic regime in confined nanoflows, *Phys. Rev. Lett.*, **108**, 084501, 2012.
- [127] O. Svitelskiy, V. Sauer, N. Liu, K. M. Cheng, E. Finley, M. R. Freeman and W. K. Hiebert: Pressurized fluid damping of nanoelectromechanical systems, *Phys. Rev. Lett.*, **103**, 244501, 2009.
- [128] O. Svitelskiy, V. Sauer, D. Vick, K. M. Cheng and N. Liu: Nanoelectromechanical devices in a fluidic environment, *Phys. Rev. E*, **85**, 056313, 2012.
- [129] R. B. Bhiladvala and Z. J. Wang: Effect of fluids on the Q factor and resonance frequency of oscillating micrometer and nanometer scale beams, *Phys. Rev. E*, **69**, 036307, 2004.
- [130] F. Lochon, I. Dufour and D. Rebière: An alternative solution to improve sensitivity of resonant microcantilever chemical sensors: comparison between using high-order modes and reducing dimensions, *Sens. Actuators B*, **108**, 979-985, 2005.
- [131] B. N. Johnson, H. Sharma and R. Mutharasan: Torsional and lateral resonant modes of cantilevers as biosensors: alternatives to bending modes, *Anal. Chem.*, **85**, 1760-1766, 2013.
- [132] H. Xie, J. Vitard, S. Haliyo and S. Règnier: Enhanced sensitivity of mass detection using the first torsional mode of microcantilevers, *Meas. Sci. Technol.*, **19**, 055207, 2008.

- [133] A. Ababneh, A. N. Al-Omari, A. M. K. Dagamseh, H. C. Qiu, D. Feili, V. Ruiz-Díez, T. Manzaneque, J. Hernando, J. L. Sanchez-Rojas, A. Bittner, U. Schmid and H. Seidel: Electrical characterization of micromachined AlN resonators at various back pressures, *Microsyst. Technol.*, **20**, 663-670, 2014.
- [134] C. P. Green and J. E. Sader: Torsional frequency response of cantilever beams immersed in viscous fluids with applications to the atomic force microscope, *J. Appl. Phys.*, **92**, 6262-6274, 2002.
- [135] J. A. Judge, J. F. Vignola and J. Jarzynski: Dissipation from microscale and nanoscale beam resonators into a surrounding fluid, *Appl. Phys. Lett.*, **92**, 124102, 2008.
- [136] F. Lochon, I. Dufour and D. Rebière: A microcantilever chemical sensors optimization by taking into account losses, *Sens. Actuators B*, **118**, 292-296, 2006.
- [137] D. Anselmetti, R. Luthi, E. Meyer, T. Richmond, M. Dreier, J. E. Frommer and H. J. Guntherodt: Attractive mode imaging of biological materials with dynamic force microscopy, *Nanotechnology*, **5**, 87-94, 1994.
- [138] Q. Zhong and D. Inniss: Fractured polymer/silica fiber surface studied by tapping mode atomic force microscopy, *Surf. Sci. Lett.*, **290**, 688-692, 1993.
- [139] H. G. Hansma, R. L. Sinsheimer, J. Gropper, T. C. Bruice, V. Elings, G. Gurley, M. Bezanilla, I. A. Mastrangelo, P. V. C. Hough and P. K. Hansma: Recent advances in atomic force microscopy of DNA, *Scanning*, **15**, 296-299, 1993.
- [140] P. K. Hansma, J. P. Cleveland, M. Radmacher, D. A. Walters, P. E. Hillner, M. Bezanilla, M. Fritz, D. Vie, H. G. Hansma, C. B. Prater, J. Massie, L. Fukunaga, J. Gurley and V. Elings: Tapping mode atomic force microscopy in liquids, *Appl. Phys. Lett.*, **64**, 1738-1740, 1994.
- [141] Y. Huang and C. C. Williams: Capacitance voltage measurement and modeling on a nanometer scale by scanning C-V microscopy, *J. Vac. Sci. Technol. B*, **12**, 369-372, 1994.
- [142] Y. Huang, C. C. Williams and J. Slinkman: Quantitative two-dimensional dopant profile measurement and inverse modeling by scanning capacitance microscopy, *Appl. Phys. Lett.*, **66**, 344-346, 1995.
- [143] A. Pavlov, Y. Pavlova and R. Laiho: Proposal of scanning probe microscope with MEMS cantilever for study of conductive and non-conductive materials, *Rev. Adv. Mater. Sci.*, **5**, 324-328, 2003.
- [144] A. Burgdorfer: The influence of the molecular mean free path on the performance

- of hydrodynamic gas lubricated bearings, *J. Basic Eng.*, **81**, 94-99, 1959.
- [145] F. P. Mechel: Revision of the Kirchhoff-Rayleigh theory of sound propagation in visco-thermal air, *Acta Acust. united Ac.*, **93**, 507-534, 2007.
- [146] A. Maali, C. Hurth, R. Boisgard, C. Jai, T. Cohen-Bouhacina and J. P. Aimé: Hydrodynamics of oscillating atomic force microscopy cantilevers in viscous fluid, *J. Appl. Phys.*, **97**, 074907, 2005.
- [147] H. C. Qiu, D. Feili, X. Z. Wu and H. Seidel: Dynamic analysis of the torsional resonant mode of piezoelectric microcantilevers, *Mikrosystemtechnik Kongress*, 788-791, 2013.
- [148] H. C. Qiu, D. Feili, X. Z. Wu and H. Seidel: Resonance-mode effect on piezoelectric microcantilever performance in air, with a focus on the torsional modes, *Chin. Phys. B*, **23**, 027701, 2014.
- [149] T. Cai, F. Josse, I. Dufour, S. Heinrich, N. Nigro and O. Band: Resonant characteristics of rectangular microcantilevers vibrating torsionally in viscous liquid media, *IEEE International Frequency Control Symposium*, 807-812, 2012.
- [150] Timoshenko: Vibration problems in engineering, Van Nostrand Company Inc., New York, 1937.
- [151] Y. L. Luke: The special functions and their approximations, Academic Press, New York, 1979.
- [152] W. K. Blake: The radiation from free-free beams in air and in water, *J. Sound Vib.*, **33**, 427-450, 1974.
- [153] F. Fahy: Sound and structural vibration: Radiation, transmission, and response, Academic Press, New York, 1985.
- [154] A. Frangi, M. Cremonesi, A. Jaakkola and T. Pensala: Analysis of anchor and interface losses in piezoelectric MEMS resonators, *Sens. Actuators A*, **190**, 127-135, 2013.
- [155] J. Yang, T. Ono and M. Esashi: Energy dissipation in submicrometer thick single-crystal silicon cantilevers, *J. Microelectromech. Syst.*, **11**, 775-783, 2002.
- [156] CoventorWare 2012 Documentation: MEMS Design and Analysis in ANALYZER Tutorials
- [157] R. M. Langdon: Resonator sensors—a review, *J. Phys. E: Sci. Instrum.*, **18**, 103-115, 1985.
- [158] T. Yan, B. E. Jones, R. T. Rakowski, M. J. Tudor, S. P. Beeby and N. M. White: Design and fabrication of thick-film PZT-metallic triple beam resonators, *Sens.*

- Actuators A*, **115**, 401-407, 2004.
- [159] B. P. Harrington and R. Abdolvand: In-plane acoustic reflectors for reducing effective anchor loss in lateral-extensional MEMS resonators, *J. Micromech. Microeng.*, **21**, 085021, 2011.
- [160] M. Haueis, J. Dual and R. Buser: A mechanical isolation of a bending resonator, *Sens. Actuators A*, **128**, 257-264, 2006.
- [161] A. T. Ferguson, L. Li, V. T. Nagaraj, B. Balachandran, B. Piekarski and D. L. DeVoe: Modeling and design of composited free-free beam piezoelectric resonators, *Sens. Actuators A*, **118**, 63-69, 2005.
- [162] L. W. Huang and C. T. C. Nguyen: Capacitive piezoelectric AlN resonators with $Q > 12000$, *Proc. MEMS 2011*, 173-176, 2011.
- [163] T. Ikeda: Fundamentals of piezoelectricity, Oxford University Press, Oxford, 1990.
- [164] A. S. Nowick and B. S. Berry: Anelastic relaxation in crystalline solids, Academic Press, New York, 1972.
- [165] M. S. Blanter, I. S. Golovin, H. Neuhauser and H. R. Sinning: Internal friction in metallic materials, Springer-Verlag, New York, 2007.
- [166] G. Sosale, S. Prabhakar and L. G. Fréchet: A microcantilever platform for measuring internal friction in thin films using thermoelastic damping for calibration, *J. Microelectromech. Syst.*, **20**, 764-773, 2011.
- [167] A. Duwel, R. N. Candler, T. W. Kenny and M. Varghese: Engineering MEMS resonators with low thermoelastic damping, *J. Microelectromech. Syst.*, **15**, 1437-1445, 2006.
- [168] Z. Hao, S. Pourkamali and F. Ayazi: VHF single-crystal silicon elliptic bulk-mode capacitive disk resonators – Part I: Design and modeling, *J. Microelectromech. Syst.*, **15**, 1043-1053, 2004.
- [169] M. A. Abdelmoneum, M. U. Demirci and C. T. C. Nguyen: Stemless wine-glass-mode disk micromechanical resonators, *Proc. IEEE MEMS*, 698-701, 2003.

Publications

Journal publications

- [1] H. C. Qiu, P. Schwarz, H. Völlm, D. Feili, X. Z. Wu and H. Seidel: Electrical crosstalk in two-port piezoelectric resonators and compensation solutions, *Journal of Micromechanics and Microengineering*, **23**, 045007, 2013.
- [2] H. C. Qiu, P. Schwarz, D. Feili, S. Merzsch, E. Peiner, X. Z. Wu and H. Seidel: Electrical performance analysis and characterization of two port piezoelectric resonators, *Microsystem Technologies*, **19**, 1131-1136, 2013.
- [3] A. Ababneh, A. N. Al-Omari, A. M. K. Dagamseh, H. C. Qiu, D. Feili, V. Ruiz-Díez, T. Manzaneque, J. Hernando, J. L. Sanchez-Rojas, A. Bittner, U. Schmid and H. Seidel: Electrical characterization of micromachined AlN resonators at various back pressures, *Microsystem Technologies*, **20**, 663-670, 2014.
- [4] H. C. Qiu, D. Feili, X. Z. Wu and H. Seidel: Resonance-mode effect on piezoelectric microcantilever performance in air, with a focus on the torsional modes, *Chinese Physics B*, **23**, 027701, 2014.
- [5] H. C. Qiu, D. Feili, X. Z. Wu and H. Seidel: Resonant-mode effect on fluidic damping of piezoelectric microcantilevers vibrating in an infinite viscous fluid, *Sensors and Actuators A* (under review) 2014.
- [6] H. C. Qiu, P. Schwarz, D. Feili, X. Z. Wu and H. Seidel: Hydrodynamics of micro beam resonator vibrating close to a surface with a moderate distance, *Journal of Micromechanics and Microengineering* (under review) 2014.
- [7] H. C. Qiu, A. Ababneh, D. Feili, X. Z. Wu and H. Seidel: Analysis of intrinsic damping in vibrating piezoelectric microcantilevers, *Journal of Sound and Vibration* (under review) 2014.

Conference publications

- [1] H. C. Qiu, P. Schwarz, D. Feili, X. Z. Wu and H. Seidel: Performance modeling and characterization of AlN resonator, *Proceedings of Mikrosystemtechnik Kongress*, 803-806, 2011.
- [2] A. Ababneh, A. N. Al-Omari, H. C. Qiu, T. Manzaneque, J. Hernando, J. L. Sanchez-Rojas, A. Bittner, U. Schmid and H. Seidel: Pressure dependence of the quality factor of piezoelectrically driven AlN/Si-microcantilevers, *Proceedings of*

- SPIE Smart Sensors, Actuators, and MEMS VI*, 876334, 2013.
- [3] H. C. Qiu, P. Schwarz, D. Feili, X. Z. Wu and H. Seidel: Viscothermal acoustic waves in micro scale resonators, *Proceedings of Transducers 2013 & Eurosensors XXVII*, 1719-1722, 2013.
- [4] H. C. Qiu, D. Feili, X. Z. Wu and H. Seidel: Dynamic analysis of the torsional resonant mode of piezoelectric microcantilevers, *Proceedings of Mikrosystemtechnik Kongress*, 788-791, 2013.
- [5] H. C. Qiu, D. Feili, X. Z. Wu and H. Seidel: Hydrodynamic analysis of piezoelectric microcantilevers vibrating in viscous compressible gases, *Proceedings of Transducers 2015 (abstract submitted)* 2015.

List of figures

Figure 1.1: Resonance curves for a resonator at pressures of 0.01 mbar (narrow resonance) and 1000 mbar (broad resonance).	6
Figure 1.2: Cantilever beam in fundamental (a) flexural, (b) torsional and (c) lateral vibration modes. The color coding represents the deflection in the relevant direction.	7
Figure 1.3: First four flexural mode shapes of a cantilever.	7
Figure 1.4: Illustration of a sphere oscillating in a Newtonian fluid at angular frequency ω . Inside the boundary layer, the flow is nearly tangential to the solid body surface.	10
Figure 1.5: Energy dissipation mechanisms of micro resonators.....	10
Figure 2.1: (a) Photograph of the sputtering machine (von Ardenne) and (b) a schematic description of the AlN reactive sputtering process.....	18
Figure 2.2: Flow chart of the resonator fabrication process.....	19
Figure 2.3: Micrograph of the drive port of the piezoelectric resonator, including the compensation electrode discussed in Section 2.3.....	19
Figure 2.4: The overall transfer function diagram of a two-port piezoelectric resonator.	20
Figure 2.5: Illustration of the effect of increasing the figure of merit λ on the electrical output of a two port piezoelectric resonator, the lightest color lines show the output without any crosstalk ($\lambda = 0$).	20
Figure 2.6: Simplified capacitance model of the piezoelectric resonator.	21
Figure 2.7: Equivalent circuit model for the two port piezoelectric resonator.	21
Figure 2.8: Measured and analytically derived response of the AlN based piezoelectric resonator at normal atmosphere.....	22
Figure 2.9: Measured and analytically calculated polar diagram of the resonator's response, the left circle shows the ideal resonance polar diagram without any crosstalk.	23
Figure 2.10: Schematic diagram of the feedthrough capacitance cancellation technique, using a compensation capacitor.....	25
Figure 2.11: Simplified capacitance model for the piezoelectric resonator with an on-chip compensation electrode. There are two compensation electrodes in the drive port and sense port separately, only the one in the drive port is used.	25
Figure 2.12: Electric wiring diagram for cancelling the feedthrough capacitance, using the on-chip compensation electrode in the drive port.	25
Figure 2.13: Schematic diagram of the feedthrough capacitance cancellation technique by applying an inverted voltage $-kU_i$ to the bottom electrode.	26
Figure 2.14: Electric wiring diagram for cancelling the feedthrough capacitance by applying an inverted voltage with adjustable gain k to the SCS bottom electrode.	26
Figure 2.15: Photograph of the compensation-readout circuit.	27
Figure 2.16: Results of on-chip compensation and electrical compensation of the piezoelectric resonator. The original uncompensated signal is shown for comparison.....	28
Figure 2.17: Measured amplitude and phase curves as well as polar plots of original resonator output at normal atmosphere and 1 mbar.	29

Figure 2.18: Measured amplitude and phase curves as well as polar plots of the output after signal conditioning at normal atmosphere and 1 mbar.....	29
Figure 3.1: (a) The camera picture and (b) the schematic diagram of the measurement setup used to characterize the micro resonators in the vacuum chamber.	33
Figure 3.2: The basis resonator structures: (a) cantilever, (b) bridge and (c) plate.	34
Figure 3.3: (a) The photo of a packaged chip for gas flow evaluation and (b) the schematic cross section view of the setup.	35
Figure 3.4: (a) The photo of a packaged chip for squeeze film evaluation and (b) the schematic cross section view of the setup.	35
Figure 3.5: (a) 3D illustration of the surface and (b) the surface profile of a bridge resonator.	36
Figure 3.6: Surface profile of the top covers.....	36
Figure 3.7: Measured resonance (circles) with fitting curves (solid line) according to eq. (3.2) yielding the fit parameters $f_r = 46.325$ kHz and $Q = 1691.8$	37
Figure 3.8: Resonant measurements of the cantilever under the pressures from HV to 1000 mbar in N_2 environment for the first flexural mode. The insert shows the resonance mode and cantilever dimensions (in μm).	38
Figure 3.9: Resonance frequency shift for the first flexural mode as a function of ambient pressure in N_2 atmosphere.	39
Figure 3.10: Variation of Q factor with ambient pressure in N_2 environment for the first flexural mode. The solid diamond points are the measured Q factors, while the hollow points are the calculated Q factors purely due to gas damping, by separating mathematically the intrinsic damping.....	40
Figure 3.11: Resonance frequency shifts with ambient pressure and different gases for the resonator in its first mode.	42
Figure 3.12: Normalized frequency shifts as a function of the density ρ of the gases under different pressures. The insert figure shows the results for atmospheric pressure only....	42
Figure 3.13: Variation of Q factors with ambient pressure for different gases with the resonator in its first flexural mode.....	43
Figure 3.14: Variation of the Q factor due to gas damping in the high pressure regime (approx. viscous regime) for different gases with the resonator in its first flexural mode.	44
Figure 3.15: Evolution of the Q factors as a function of the product of the density ρ and the dynamic viscosity η of the gases under different pressures. The insert figure shows the results at atmospheric pressure only.....	44
Figure 3.16: The Q factors of cantilevers with different widths and lengths. The Q factors of fully piezo-electrode stack covered cantilevers in HV were included for comparison.	45
Figure 3.17: The Q factors of cantilevers with different thicknesses.....	46
Figure 3.18: Amplitude spectrum and mode shapes of the cantilever at normal atmospheric N_2	47
Figure 3.19: The Q factors of different modes as a function of ambient pressure.....	48
Figure 3.20: The Q factors of the flexural modes at different pressures in N_2 environment. ..	49

- Figure 3.21: The Q factors as a function of resonance frequency of different cantilevers at different modes, (a) in HV and (b) at atmospheric pressure in N_2 environment. The dashed lines are guides to the eye only..... 50
- Figure 3.22: The Q factors of the cantilever of different flexural modes in different gases at atmospheric pressure. 51
- Figure 3.23: Amplitude spectra of bridge resonator in fundamental mode in N_2 at atmospheric pressure. The curves for 250 and 300 μm and no gap are overlapped in this figure. Insert shows the quality factor and resonance frequency, the dashed lines represent the limit as without gap. 53
- Figure 3.24: Variation of Q factors with ambient pressure for N_2 with different gap heights. 53
- Figure 3.25: Variation of Q factors with ambient pressure for different gases with a 20 μm gap. 54
- Figure 3.26: Variation of Q factors with ambient pressure for different gases with a 50 μm gap. 55
- Figure 3.27: Replot of the Q factors shown in Figs. 3.25 and 3.26 as a function of effective viscosity..... 55
- Figure 3.28: Variation of Q factors over pressure for the 1st and 3rd flexural modes and for two different gap heights in N_2 atmosphere. 56
- Figure 4.1: Two regions in the acoustic domain: the bulk and the boundary layer, and three waves due to vibration..... 62
- Figure 4.2: Characteristic length scales for vibrations in air: acoustic wavelength (solid), viscous wavelength (dashed), thermal wavelength (dotted) and boundary layer thickness (dash-dotted)..... 62
- Figure 4.3: The geometry of the PI resonator (in μm). The insert shows the photo of the resonator mounted on a PCB board with attached bonding wires..... 63
- Figure 4.4: Geometrical model of the current fluid structure interaction problem as generated in COMSOL Multiphysics software package..... 64
- Figure 4.5: Pressure in the fluid domain surrounding the resonator: (a) bounded with a substrate and (b) unbounded constellation. 64
- Figure 4.6: Measured and simulated Q factor of the resonator as a function of ambient pressure..... 65
- Figure 4.7: Simplified model for the beam resonator: (a) sphere string model and (b) cylinder model. 67
- Figure 4.8: Measured and simulated Q factors versus pressure for the flexural mode of the $C6-I$ cantilever. The data points represent the measurement results, the dotted lines represent the sphere string model predictions (eq. (4.18)), while the dashed lines are the cylinder model predictions (eq. (4.24)). The vertical lines represent the pressure where $Kn = 0.1$, at higher pressure or equally lower Kn , the gas can be considered as in the viscous regime. 71
- Figure 4.9: Q factor dependence on resonator geometries in N_2 at atmospheric pressure..... 72
- Figure 4.10: Measured and simulated Q factors versus pressure for the torsional modes of the cantilever. The data points represent the measurement results, the dotted lines represent the sphere string model predictions (eq. (4.26)), while the dashed lines are the cylinder model predictions (eq. (4.30)). The vertical line represents the pressure where $Kn = 0.1$, at

- higher pressure or equally lower Kn , the gas can be considered as in the viscous regime.
 74
- Figure 4.11: Visualized illustration of simulated pressure distribution around the cantilever cross-section in (a) the flexural mode, and (b) the torsional mode. 74
- Figure 4.12: Quality factors due to gas damping of the resonance frequency and mode number. The data points are derived from the measurements after subtracting intrinsic damping, the solid lines are calculations based on the incompressible gas assumption (eq. (4.23)), while the dash-dotted lines are the acoustic wave model predictions (eq. (4.36)). 76
- Figure 4.13: A schematic of extended squeeze film model. 78
- Figure 4.14: Plot showing the quality factors due to gas damping of the $B2$ bridge resonator in the fundamental mode in atmospheric N_2 . The squares represent the measured Q factor due to gas damping, which are derived from the measurements after subtracting intrinsic damping, while the crosses are the predictions based on the COMSOL simulation. The dashed lines represent the analytical/semianalytical calculations, and the solid line shows the viscous model prediction, which is the limit for a structure without gap. 82
- Figure 4.15: Measured and simulated Q factors versus pressure for the $B2$ bridge resonator vibrating in N_2 close to a surface. The data points represent the measurement results, the dotted lines represent the squeeze film model predictions (eq. (4.41)), the dashed lines are the extended squeeze film and unsteady N-S models predictions (eqs. (4.44 and 4.47)), the viscous model (eq. (4.24)) is also shown for comparison in Fig. 4.15 (g). 84
- Figure 4.16: Qualitative approximation of the Q factors for the bridge resonator vibrating close to a surface with different gap sizes in N_2 environment. 85
- Figure 5.1: Fundamental mode shape and corresponding temperature distribution within a cantilever. 91
- Figure 5.2: Comparison of Zener's analytical model (solid line) and COMSOL simulation ('x' marks) for TED. The width and thickness of the cantilever is held fixed at $100\ \mu\text{m}$ and $20\ \mu\text{m}$, the length is varied from $50\ \mu\text{m}$ to $2000\ \mu\text{m}$. Since the frequency is inversely proportional to length squared, the shorter length corresponds to higher frequency. 93
- Figure 5.3: TED for higher modes of a micro cantilever with dimensions $800 \times 100 \times 20\ \mu\text{m}$. The solid line is Zener's calculation, the 'x' marks represent COMSOL simulations for the flexural modes of the pure silicon beam. The simulation results for torsional and lateral modes are represented by solid square and triangle points. For comparison, the flexural mode TED of the beam covered by 20% piezo-electrode stack are also simulated and shown by the 'o' marks. 94
- Figure 5.4: Temperature variation of the cantilever beam (a) without the piezo-electrode stack under the first flexural mode, (b) with the stack under the first flexural mode, (c) without the stack under the fifth flexural mode and (d) with the stack under the fifth flexural mode. 94
- Figure 5.5: Schematic view of cantilever resonators connected to their support structures: (a) a cantilever attached to a semi-infinite support, the thickness is assumed to be infinite (2D assumption), (b) a cantilever attached to a support of finite thickness t_s , while lateral dimensions are assumed to be semi-infinite, and (c) a cantilever attached to a support that has semi-infinite space. 96
- Figure 5.6: Geometry of the silicon chip and the meshed model. 98
- Figure 5.7: 3D illustration of energy dissipation for the cantilever vibrating in the first flexural mode through different substrates: (a) chip frame, (b) semi-infinite plate (corresponds to

- Fig.5.5 (a)), (c) semi-infinite plate with finite thickness (corresponds to Fig. 5.5 (b)) and (d) semi-infinite space (corresponds to Fig. 5.5 (c)). 98
- Figure 5.8: Comparison of Q factors resulting from anchor losses calculated using the three different analytical models (solid lines) and corresponding CoventorWare simulation (depicted by marks) under the same boundary assumptions. The width and thickness of the cantilevers are held fixed as $100\ \mu\text{m}$ and $20\ \mu\text{m}$, the lengths are varied from $100\ \mu\text{m}$ to $1000\ \mu\text{m}$. For anchor losses in the realistic chips (red 'x' marks), there is no available analytical model..... 100
- Figure 5.9: Schematic of the cantilever for coating film damping experiment. The piezo-electrode coating films (represented by the yellow parallelograms) are coated on top of the beam, having various lengths l_e with respect to the full cantilever length. 102
- Figure 5.10: Measured resonance frequencies of the cantilevers. The first type of cantilevers has resonance frequencies around $6\ \text{kHz}$, the second type around $20\ \text{kHz}$ 102
- Figure 5.11: Measured (a) Q factors and (b) loss factors Q^{-1} of the cantilevers as a function of coating coverage. 102
- Figure 5.12: Measured total cantilever loss factors Q^{-1} , along with the predicted loss factors due to different damping mechanisms. The diagrams show the contributions from each damping mechanism. 105

List of tables

Table 2.1: Capacitances of the fabricated resonator.	22
Table 3.1: Properties of different gases (at 20 °C and 1000 mbar).....	32
Table 3.2: Resonator geometries.....	34
Table 3.3: Comparison of experimentally observed resonance frequencies f_e (kHz) and COMSOL simulated frequencies f_s (kHz).	47
Table 4.1: Overview of the determined adjustment factors ξ from the replica of the quality curves for the different gap heights h_0 in Fig. 4.16.	85
Table 5.1: Properties of the materials used in the analytical calculation and COMSOL simulation. The values are obtained from the material database of COMSOL software..	92
Table 5.2: Comparison between measured Q factors and predicted Q factors of the first flexural mode of different sizes of piezoelectric cantilevers.	104
Table 5.3: Comparison between measured Q factors and predicted Q factors of the first lateral mode of different sizes of piezoelectric cantilevers.	105

Nomenclature

Greek symbols

Symbol	Description	Unit
α	thermal expansion coefficient	K^{-1}
α_a	coefficient for acoustic pressure	-
α_h	coefficient for entropic pressure	-
α_{AlN}	AlN thermal expansion coefficient	K^{-1}
α_{Au}	Au thermal expansion coefficient	K^{-1}
α_{Si}	Si [100] thermal expansion coefficient	K^{-1}
β	geometrical correction factor	-
γ	specific heat ratio	-
Γ	hydrodynamic function	-
Γ_L	$\text{Log}_{10}(\Gamma)$	-
Γ_{flex}	hydrodynamic function for flexural mode	-
$\Gamma_{flex, real}$	real part of hydrodynamic function for flexural mode	-
$\Gamma_{flex, imag}$	imaginary part of hydrodynamic function for flexural mode	-
Γ_{squ}	hydrodynamic function for squeeze film	-
$\Gamma_{squ, imag}$	imaginary part of hydrodynamic function for squeeze film	-
Γ_{tors}	hydrodynamic function for torsional mode	-
$\Gamma_{tors, real}$	real part of hydrodynamic function for torsional mode	-
$\Gamma_{tors, imag}$	imaginary part of hydrodynamic function for torsional mode	-
ε_{dyn}	root component	-
η	dynamic viscosity	Pa s
η_{eff}	effective viscosity	Pa s
κ	thermal conductivity	W/(m K)
κ_{AlN}	AlN thermal conductivity	W/(m K)
κ_{Au}	Au thermal conductivity	W/(m K)
κ_{Si}	Si [100] thermal conductivity	W/(m K)
λ	ratio of crosstalk to mechanical resonance signal	-

Symbol	Description	Unit
<i>(continued)</i>		
λ	mean free path	m
λ_a	acoustic wavelength	m
λ_b	spatial wavelength of slender beam	m
λ_h	entropic wavelength	m
λ_v	viscous wavelength	m
ν_{AIN}	AlN Poission's ratio	-
ν_{Au}	Au Poission's ratio	-
ν_{si}	Si [100] Poission's ratio	-
ξ	fitting parameter	-
ξ_c	constant related to bulk viscoelasticity of coating layer	-
ξ_{int}	fitting parameter for Q_{int}	-
ξ_{mol}	fitting parameter for Q_{mol}	-
ξ_{vis}	fitting parameter for Q_{vis}	-
ξ_{dyn}	fitting parameter for Q_{dyn}	-
ρ	gas density	kg/m ³
ρ_{AIN}	AlN density	kg/m ³
ρ_{Au}	Au density	kg/m ³
ρ_b	beam density	kg/m ³
ρ_{si}	Si [100] density	kg/m ³
σ	squeeze number	-
σ_r	radiation efficiency	-
ϕ_a	coefficient for acoustic pressure gradient	-
ϕ_h	coefficient for entropic pressure gradient	-
ω	angular frequency	rad/s
ω_r	resonance angular frequency	rad/s

Roman symbols

Symbol	Description	Unit
a_{1-4}, b_{1-4}	hydrodynamic function parameters	-
a_k	coefficients for hydrodynamic function	-
a_p	pressure dependent parameter	m^2/s
c_0	sound speed	m/s
c_0	damping coefficient of a resonator	$\text{N s}/\text{m}$
c_a	fluidic damping coefficient of a resonator	$\text{N s}/\text{m}$
$c_{flex,cyli}$	damping coefficient for a cylinder in flexural mode	$\text{N s}/\text{m}$
c_{sphe}	damping coefficient for a sphere	$\text{N s}/\text{m}$
c_{squ}	squeeze film damping coefficient	$\text{N s}/\text{m}$
$c_{squ, ex}$	extended squeeze film damping coefficient	$\text{N s}/\text{m}$
C_{comp}	compensation capacitor	F
C_d, C_{d1}, C_{d2}	drive port shunt capacitance	F
C_{ft}	feedthrough capacitance	F
C_m	capacitance in motional branch	F
C_n	n th positive root	-
C_s, C_{s1}, C_{s2}	drive port shunt capacitance	F
C_p	heat capacity at constant pressure	$\text{J}/(\text{kg K})$
C_{pAlN}	AlN heat capacity at constant pressure	$\text{J}/(\text{kg K})$
C_{pAu}	Au heat capacity at constant pressure	$\text{J}/(\text{kg K})$
C_{psi}	Si [100] heat capacity at constant pressure	$\text{J}/(\text{kg K})$
C_v	heat capacity at constant volume	$\text{J}/(\text{kg K})$
d_0	molecular diameter	m
d_{31}, d_{33}	piezoelectric constant	pm/V
E	elasticity modulus	Pa
E_{AlN}	AlN elasticity modulus	Pa
E_{Au}	Au elasticity modulus	Pa
E_{si}	Si [100] elasticity modulus	Pa

Symbol	Description	Unit
<i>(continued)</i>		
f	external force acting on a resonator	N
$f_{0, dyn}$	thermal resonance frequency	Hz
f_{drive}	external driven force on a resonator	N
f_e	experimentally observed resonance frequency	Hz
f_{hydro}	fluidic drag force on a resonator	N
f_r	resonance frequency	Hz
$f_{r, n}$	resonance frequency of n th flexural mode	Hz
$f_{r, HV}$	resonance frequency in high vacuum	Hz
f_s	simulated resonance frequency	Hz
Δf	resonance frequency shift	Hz
F_0	thermal relaxation frequency	Hz
\mathbf{F}_d	fluid drag force	N
h_0	gap height	m
H	nondimensional gap height	-
H_L	$\text{Log}_{10}(H)$	-
i	imaginary unit	-
i_{comp}	current from compensation capacitance	A
i_r, i_r'	current from motional branch	A
i_{ft}, i_{ft}'	current from feedthrough capacitance	A
i_o	output current	A
k	gain of inverted voltage amplifier	-
k	coefficient for anchor loss	-
k_0	spring constant for a resonator	N/m
k_a	fluidic spring constant for a resonator	N/m
k_a	acoustic wave number	-
k_h	entropic wave number	-
k_{spher}	spring constant for a sphere	N/m

Symbol	Description	Unit
<i>(continued)</i>		
k_v	viscous wave number	-
K_0, K_1	modified Bessel functions of the third kind	-
K_b	Boltzmann constant (1.38×10^{-23})	-
Kn	Knudsen number	-
l	resonator length	m
l_e	coating film length	m
l_{eff}	effective plate length	m
Δl	additional plate length	m
L	characteristic dimension of a object	m
L_m	inductance in motional branch	H
m	resonator mass	kg
M	molar mass	kg/mol
p	ambient pressure ($1 \text{ N/m}^2 = 1 \text{ Pa} = 10^{-5} \text{ mbar}$)	Pa
p_a	acoustic pressure ($1 \text{ N/m}^2 = 1 \text{ Pa} = 10^{-5} \text{ mbar}$)	Pa
p_h	entropic pressure ($1 \text{ N/m}^2 = 1 \text{ Pa} = 10^{-5} \text{ mbar}$)	Pa
Q	quality factor	-
Q_{acous}	quality factor due to acoustic damping	-
Q_{analy}	analytical quality factor	-
Q_{anchor}	quality factor due to anchor loss	-
$Q_{coating}$	quality factor due to thin film coating loss	-
Q_{dyn}	quality factor of dynamic damping	-
$Q_{flex,sphe}$	quality factor for flexural mode from sphere string model	-
$Q_{flex,cyli}$	quality factor for flexural mode from cylinder model	-
Q_{gas}	quality factor due to gas damping	-
Q_{int}	intrinsic quality factor	-
Q_{meas}	measured quality factor	-
Q_{mol}	quality factor due to molecular gas damping	-

Symbol	Description	Unit
<i>(continued)</i>		
Q_{squ}	quality factor from squeeze film model	-
$Q_{squ, ex}$	quality factor from extended squeeze film model	-
$Q_{squ, NS}$	quality factor from unsteady Navier-Stokes model	-
Q_{tot}	total quality factor	-
$Q_{tors, sphe}$	quality factor for torsional mode from sphere string model	-
$Q_{tors, cyli}$	quality factor for torsional mode from cylinder model	-
Q_{TED}	quality factor due to TED	-
Q_{vis}	quality factor due to viscous damping	-
R	sphere radius	m
Re	Reynolds number	-
Re_L	$\text{Log}_{10}(Re)$	-
R_m	resistance in motional branch	Ω
s	$i\omega$	rad/s
t	time	s
t	resonator thickness	m
t_e	coating film thickness	m
t_s	substrate thickness	m
T	ambient temperature	K
ΔT	temperature fluctuation	K
\mathbf{u}	velocity vector	m/s
\mathbf{u}_v	viscous velocity vector	m/s
\mathbf{u}_l	laminar velocity vector	m/s
u_0	object velocity	m/s
U_i	input of a two port piezoelectric resonator	V
U_o	output of resonator	V
U_M	mechanical resonance behavior of resonator	V
U_E	electrical crosstalk in resonator	V

Symbol	Description	Unit
<i>(continued)</i>		
U_{off}	offset voltage	V
w	resonator width	m
w_{eff}	effective plate width	m
Δw	additional plate width	m
\widehat{W}	Fourier transformation of cantilever deformation	m
x, y, z	cartesian coordinates	m

Acknowledgements

I would like to express my sincere thanks to my supervisor Prof. Dr. Helmut Seidel, for his guidance, patience and encouragement throughout the duration of my study at the Chair of Micromechanics, Microfluidics/Microactuators (LMM). He has made these past four and a half years an enjoyable and valuable learning experience for me and he will permanently impact my future life, both academically and personally.

I am also very grateful to Prof. Dr. José Luis Sánchez-Rojas for his willingness to examine this work.

Many thanks to my colleagues in LMM: Dr. Dara Feili, Dr. Patrick Schwarz, Dr. Abdallah Ababneh, Mazier Afshar, Jianguo Zhao, Henning Völlm, Günter Marchand, Natalie Pagel, Heike Kreher, Dr. Christian Kirsh, Somaie Saremi and Christian Kiefer. I would like to especially thank Dr. Abdallah Ababneh and Dr. Patrick Schwarz for their advice and instructions in the preparation of my experiments, as well as Jianguo Zhao, with whom I enjoy many endless discussions much beyond our projects. The help from Ms. Ute Flieger is indeed appreciated. Also I would like to thank my student Yuchun Xing for the support during his master thesis project.

I would also like to thank: Detlev Cassel and Tobias Oberbillig of FH Zweibrücken and Stephan Merzsch of TU Braunschweig, for their valuable assistance during my device fabrication.

I want to mention my fantastic friend: Jiafeng Zhang. I thank my former Badminton partners Zhong Ren and Yong Pang for playing together and discharging me of so many obligations.

A special acknowledgement goes to the China Scholarship Council who covered my living during the study in the past four years. I would also like to thank my teachers in National University of Defense Technology in China. I am grateful to Prof. Xuezhong Wu for offering me the great opportunity to pursue my PhD abroad and for his constant support and encouragement during my time in Germany. I would also like to express my gratitude to Assoc. Prof. Hongjuan Cui and Assoc. Prof. Dingbang Xiao for their help and support on many matters for the past years.

Finally I would like to thank my parents and my younger sister for their love and great confidence in me through all these years.

Eidesstattliche Versicherung

Hiermit versichere ich an Eides statt, dass ich die vorliegende Arbeit selbstständig und ohne Benutzung anderer als der angegebenen Hilfsmittel angefertigt habe. Die aus anderen Quellen oder indirekt übernommenen Daten und Konzepte sind unter Angabe der Quelle gekennzeichnet. Die Arbeit wurde bisher weder im In- noch im Ausland in gleicher oder ähnlicher Form in einem Verfahren zur Erlangung eines akademischen Grades vorgelegt.

Ort, Datum

Unterschrift